

NUMERICAL MODELING OF INNOVATIVE FILM COOLING HOLE SCHEMES

by

Siavash Khajehhasani

B. Sc., Mechanical Engineering, Shahid Bahonar University of Kerman, 2007

M. Sc., Mechanical Engineering, Iran University of Science and Technology, 2010

A dissertation

presented to Ryerson University

in partial fulfillment of the
requirements for the degree of

DOCTOR OF PHILOSOPHY

in the Program of
Aerospace Engineering

Toronto, Ontario, Canada, 2014

©Siavash Khajehhasani 2014

All rights reserved

This Page Intentionally Left Blank

Author's Declaration

I hereby declare that I am the sole author of this dissertation. This is a true copy of the dissertation, including any required final revisions, as accepted by my examiners.

I authorize Ryerson University to lend this dissertation to other institutions or individuals for the purpose of scholarly research.

I further authorize Ryerson University to reproduce this dissertation by photocopying or by other means, in total or in part, at the request of other institutions or individuals for the purpose of scholarly research.

I understand that my dissertation may be made electronically available to the public.

Siavash Khajehhasani

This Page Intentionally Left Blank

Abstract

NUMERICAL MODELING OF INNOVATIVE FILM COOLING HOLE SCHEMES

Doctor of Philosophy, Aerospace Engineering, Ryerson University, June 2014
Siavash Khajehhasani

A numerical investigation of the film cooling performance on novel film hole schemes is presented using Reynolds-Averaged Navier-Stokes analysis. The investigation considers low and high blowing ratios for both flat plate film cooling and at the leading edge of a turbine blade.

A novel film hole geometry using a circular exit shaped hole is proposed, and the influence of an existing sister holes' technique is investigated. The results indicate that high film cooling effectiveness is achieved at higher blowing ratios, results of which are even greater when in the presence of discrete sister holes where film cooling effectiveness results reach a plateau. Furthermore, a decrease in the strength of the counter-rotating vortex pairs is evident, which results in more attached coolant to the plate's surface and a reduction in aerodynamic losses.

Modifications are made to the spanwise and streamwise locations of the sister holes around the conventional cylindrical hole geometry. It is found that the spanwise variations have a significant influence on the film cooling effectiveness results, while only minor effects are observed for the streamwise variations. Positioning the sister holes in locations farther from the centerline increases the lateral spreading of the coolant air over the plate's surface. This result is further verified through the flow structure analysis.

Combinations of sister holes are joined with the primary injection hole to produce innovative variant sister shaped single-holes. The jet lift-off is significantly decreased for the downstream and up/downstream configurations of the proposed scheme for the flat plate film cooling. These schemes have shown notable film cooling improvements whereby more lateral distribution of coolant is obtained and less penetration of coolant into the mainstream flow is observed.

The performance of the sister shaped single-holes are evaluated at the leading edge of a turbine blade. At the higher blowing ratios, a noticeable improvement in film cooling performance including the effectiveness and the lateral spread of the cooling air jet has been observed for the upstream and up/downstream schemes, in particular on the suction side. It is determined that the mixing of the coolant with the high mainstream flow at the leading edge of the blade is considerably decreased for the upstream and up/downstream configurations and more adhered coolant to the blade's surface is achieved.

This Page Intentionally Left Blank

Acknowledgements

1000 days ago, a new chapter started in my life; the pursuit of my PhD in film cooling under the supervision of Professor Bassam Jubran was one of my dreams that came true. During my research, he was always telling me: “Siavash! You are in the driver’s seat”. Yes! I was a driver with the best mentor, guidance, support and encouragement. He trained me to become a successful researcher and thought me great lessons that I will carry on throughout my life. Herein, I would like to express my sincerest thanks to him. It was a great honor being his student.

I would like to thank the Natural Science and Engineering Research Council of Canada for their funding towards this research. Special thanks are also due to the High Performance Computing Virtual Laboratory for their extensive computing resources.

I would like to send my utmost thanks to my friend Sobhan Etemadi; a friend who has defined the literal meaning of “pure friendship” for me. His undeniable English knowledge was always helpful for me. My special thanks also goes to Arthur Kar Leung Lin for his financial advice throughout my PhD and also his time in familiarizing me with the beauties of the Chinese culture. My best moments at Ryerson have been spent with them.

This is the moment to thank my family and I am going to make it as short as possible; because when it comes to my heart, the best way to express my appreciation is through playing music. It is enough to say that this thesis has been written for and dedicated to my mother and father as well as my loving wife, whose presence and support allowed me to accomplish success and attain my dream goals.

This Page Intentionally Left Blank

For
My
Loving Mother and Father,
&
Beloved Wife

This Page Intentionally Left Blank

Table of Contents

ABSTRACT	V
ACKNOWLEDGEMENTS	VII
TABLE OF CONTENTS	XI
LIST OF FIGURES	XIII
LIST OF TABLES	XVI
NOMENCLATURE	XVII
1. INTRODUCTION	1
1.1. RESEARCH MOTIVATION	1
1.2. THESIS OBJECTIVES.....	2
1.3. THESIS OUTLINE	3
2. LITERATURE REVIEW	4
2.1. CYLINDRICAL FILM COOLING HOLES	4
2.2. FILM COOLING THROUGH A SLOT	5
2.3. FLOW STRUCTURE CONTROL SCHEMES.....	7
2.3.1. Shaped Holes	10
2.3.2. Anti-Vortex Holes.....	15
2.4. NUMERICAL APPROACHES	17
3. GOVERNING EQUATIONS AND TURBULENCE MODELING	20
3.1. GOVERNING EQUATIONS	20
3.2. STANDARD $k - \epsilon$ MODEL	22
3.3. RNG $k - \epsilon$ MODEL.....	23
3.4. REALIZABLE $k - \epsilon$ MODEL.....	25
3.5. REYNOLDS-STRESS MODEL.....	27
4. CIRCULAR EXIT SHAPED HOLE WITH DISCRETE SISTER HOLES’ INFLUENCE	30
4.1. PROBLEM STATEMENT	30
4.2. COMPUTATIONAL OVERVIEW AND DOMAIN.....	33
4.3. RESULTS.....	35
4.3.1. Turbulence Modeling.....	36
4.3.2. Film Cooling Effectiveness.....	38
4.3.3. Flow Structure.....	41
4.3.4. Effect of the Exit Hole Shape	46
4.4. CONCLUSIONS	47
5. MODIFICATION OF DISCRETE SISTER HOLES’ LOCATION	49

5.1.	PROBLEM STATEMENT	49
5.2.	COMPUTATIONAL OVERVIEW AND DOMAIN.....	52
5.2.1.	COMPUTATIONAL GRID	53
5.2.2.	Effect of Mainstream Channel Height	54
5.3.	RESULTS.....	56
5.3.1.	Validation.....	56
5.3.2.	Film Cooling Effectiveness.....	57
5.3.3.	Flow Structure.....	66
5.4.	CONCLUSIONS	73
6.	SISTER SHAPED SINGLE–HOLE SCHEMES.....	75
6.1.	PROBLEM STATEMENT	75
6.2.	COMPUTATIONAL OVERVIEW AND DOMAIN.....	79
6.3.	RESULTS.....	80
6.3.1.	Film Cooling Effectiveness.....	81
6.3.2.	Flow Structure.....	86
6.3.3.	Effect of the Exit Hole Shape	91
6.4.	CONCLUSIONS	94
7.	EVALUATION OF THE SISTER SHAPED SINGLE–HOLE SCHEMES AT THE LEADING EDGE.....	96
7.1.	PROBLEM STATEMENT	96
7.2.	COMPUTATIONAL OVERVIEW AND DOMAIN.....	102
7.2.1.	Computational Grid.....	103
7.3.	RESULTS.....	105
7.3.1.	Validation.....	106
7.3.2.	Film Cooling Effectiveness.....	107
7.3.3.	Temperature Contours.....	112
7.3.4.	Velocity Plot Distributions.....	116
7.4.	CONCLUSIONS	120
8.	CONCLUSIONS & RECOMMENDATIONS FOR FUTURE WORK.....	121
8.1.	CONCLUSIONS	121
8.2.	RECOMMENDATIONS FOR FUTURE WORK	123
	APPENDIX A: PEER REVIEWED PUBLICATIONS	125
	APPENDIX B: PROFILE COORDINATES FOR AGTB BLADE.....	127
	REFERENCES.....	128

List of Figures

FIGURE 1.1: LIFETIME PROGRESSION OF TURBINE ENTRY TEMPERATURE (ADOPTED FROM [1]).....	2
FIGURE 2.1: FOUR TYPES OF VORTICAL STRUCTURES ASSOCIATED WITH JET IN CROSSFLOW NEAR-FIELD [23].....	8
FIGURE 2.2: FOUR TYPES OF SHAPED FILM COOLING HOLES [9]	10
FIGURE 2.3: SCHEMATIC OF (A) LOUVER, (B) DUMBELL, (C) FAN-SHAPED AND (D) CRESCENT SHAPED HOLES [46].....	13
FIGURE 2.4: DESIGN CONCEPT OF (A) HEART-SHAPED HOLE [47] - (B) DJFC AND NEKOMIMI [48].....	14
FIGURE 2.5: CONFIGURATION OF (A) TRIPLE JETS [53], (B) ANTI-VORTEX HOLES [56] AND (C) SISTER HOLES [62]	17
FIGURE 4.1: GEOMETRY OF EESH WITH UP/DOWNSTREAM DISCRETE SISTER HOLES	31
FIGURE 4.2: TOP VIEW OF CESH GEOMETRY WITH UP/DOWNSTREAM DISCRETE SISTER HOLES	32
FIGURE 4.3: SCHEMATIC VIEW OF COMPUTATIONAL DOMAIN AND BOUNDARY CONDITIONS.....	34
FIGURE 4.4: SIDE VIEW OF THE COMPUTATIONAL GRIDS (EESH WITH UP/DOWNSTREAM SISTER HOLES).	35
FIGURE 4.5: PERFORMANCE OF DIFFERENT NEAR-WALL APPROACHES IN TERMS OF CENTERLINE FILM COOLING EFFECTIVENESS	36
FIGURE 4.6: PERFORMANCE OF DIFFERENT RANS-BASED TURBULENCE MODELS IN TERMS OF CENTERLINE FILM COOLING EFFECTIVENESS	37
FIGURE 4.7: CENTERLINE FILM COOLING EFFECTIVENESS	39
FIGURE 4.8: LATERALLY AVERAGED FILM COOLING EFFECTIVENESS	40
FIGURE 4.9: TEMPERATURE CONTOURS AND VELOCITY VECTORS FOR BLOWING RATIO OF $M = 0.5$ AT $x/D = 1$	42
FIGURE 4.10: TEMPERATURE CONTOURS AND VELOCITY VECTORS FOR BLOWING RATIO OF $M = 0.5$ AT $x/D = 5$	43
FIGURE 4.11: TEMPERATURE CONTOURS AND VELOCITY VECTORS FOR BLOWING RATIO OF $M = 1$ AT $x/D = 1$	44
FIGURE 4.12: TEMPERATURE CONTOURS AND VELOCITY VECTORS FOR BLOWING RATIO OF $M = 1$ AT $x/D = 5$	45
FIGURE 4.13: VELOCITY MAGNITUDE CONTOURS [M/S] IN THE JET EXIT PLANE FOR $M = 0.5$ AND 1.5 (NOT DRAWN TO SCALE)	47
FIGURE 5.1: GEOMETRY OF THE CYLINDRICAL HOLE WITH BASE CASE OF THE UP/DOWNSTREAM DISCRETE SISTER HOLES	51
FIGURE 5.2: SCHEMATIC VIEW OF COMPUTATIONAL DOMAIN AND BOUNDARY CONDITIONS.....	53

FIGURE 5.3: THE GRID SENSITIVITY TEST ($M = 1$, $DR = 2$).....	54
FIGURE 5.4: EFFECT OF MAINSTREAM CHANNEL HEIGHT ON CENTERLINE FILM COOLING EFFECTIVENESS ($M = 1$, $DR = 2$)	55
FIGURE 5.5: FILM COOLING EFFECTIVENESS ($M = 1$, $DR = 2$)	56
FIGURE 5.6: CENTERLINE FILM COOLING EFFECTIVENESS – STREAMWISE VARIATION OF THE DISCRETE SISTER HOLES’ LOCATION	59
FIGURE 5.7: CENTERLINE FILM COOLING EFFECTIVENESS – SPANWISE VARIATION OF THE DISCRETE SISTER HOLES’ LOCATION.....	60
FIGURE 5.8: LATERALLY AVERAGED FILM COOLING EFFECTIVENESS – STREAMWISE VARIATION OF THE DISCRETE SISTER HOLES’ LOCATION	62
FIGURE 5.9: LATERALLY AVERAGED FILM COOLING EFFECTIVENESS – SPANWISE VARIATION OF THE DISCRETE SISTER HOLES’ LOCATION	63
FIGURE 5.10: LOCAL FILM COOLING EFFECTIVENESS FOR DIFFERENT BLOWING RATIOS	65
FIGURE 5.11: TEMPERATURE CONTOURS AND VELOCITY VECTORS AT $x/D = 1$ AND 5 FOR $M = 0.25$	67
FIGURE 5.12: TEMPERATURE CONTOURS AND VELOCITY VECTORS AT $x/D = 1$ AND 5 FOR $M = 0.5$	68
FIGURE 5.13: TEMPERATURE CONTOURS AND VELOCITY VECTORS AT $x/D = 1$ AND 5 FOR $M = 1$	70
FIGURE 5.14: TEMPERATURE CONTOURS AND VELOCITY VECTORS AT $x/D = 1$ AND 5 FOR $M = 1.5$	72
FIGURE 6.1: GEOMETRY AND COMPUTATIONAL DOMAIN OF THE CYLINDRICAL HOLE.....	76
FIGURE 6.2: CLOSE-UP OF THE SIDE AND TOP VIEWS OF (A) CYLINDRICAL HOLE AND (B) 15° FORWARD DIFFUSED SHAPED HOLE (NOT DRAWN TO SCALE).....	76
FIGURE 6.3: DESIGN CONCEPT OF DOWNSTREAM SISTER SHAPED SINGLE-HOLE (DOWNSTREAM SSSH)..	77
FIGURE 6.4: DESIGN CONCEPT OF UPSTREAM SISTER SHAPED SINGLE-HOLE (UPSTREAM SSSH)	78
FIGURE 6.5: UP/DOWNSTREAM SISTER SHAPED SINGLE-HOLE (UP/DOWNSTREAM SSSH)	79
FIGURE 6.6: COMPUTATIONAL DOMAIN AND BOUNDARY CONDITIONS	79
FIGURE 6.7: CENTERLINE FILM COOLING EFFECTIVENESS	82
FIGURE 6.8: LATERALLY AVERAGED FILM COOLING EFFECTIVENESS	83
FIGURE 6.9: LOCAL FILM COOLING EFFECTIVENESS FOR DIFFERENT BLOWING RATIOS	85
FIGURE 6.10: TEMPERATURE CONTOURS AND VELOCITY VECTORS AT $x/D = 1$ AND 5 FOR $M = 0.5$	88
FIGURE 6.11: TEMPERATURE CONTOURS AND VELOCITY VECTORS AT $x/D = 1$ AND 5 FOR $M = 1.5$	90
FIGURE 6.12: VELOCITY MAGNITUDE CONTOURS [M/S] IN THE JET EXIT PLANE FOR $M = 0.5$ AND 1.5 (NOT DRAWN TO SCALE)	93
FIGURE 7.1: GEOMETRY OF AGTB-B1 BLADE [82]	96
FIGURE 7.2: SCHEMATIC OF AGTB-B1 CASCADE [86].....	98

FIGURE 7.3: CLOSE-UP OF THE SIDE AND TOP VIEW OF (A) CYLINDRICAL HOLE AND (B) 15° FORWARD DIFFUSED SHAPED HOLE (NOT DRAWN TO SCALE).....	99
FIGURE 7.4: DOWNSTREAM SISTER SHAPED SINGLE-HOLE SCHEME (DOWNSTREAM SSSH)	100
FIGURE 7.5: UPSTREAM SISTER SHAPED SINGLE-HOLE SCHEME (UPSTREAM SSSH).....	101
FIGURE 7.6: UP/DOWNSTREAM SISTER SHAPED SINGLE-HOLE SCHEME (UP/DOWNSTREAM SSSH)	101
FIGURE 7.7: COMPUTATIONAL DOMAIN AND BOUNDARY CONDITIONS	103
FIGURE 7.8: THE GRID SENSITIVITY TEST ($M = 1.1$).....	104
FIGURE 7.9: COMPUTATIONAL GRID	105
FIGURE 7.10: STATIC PRESSURE DISTRIBUTION ON BLADE'S SURFACE AT MID-SPAN PLANE.....	107
FIGURE 7.11: CENTERLINE FILM COOLING EFFECTIVENESS	109
FIGURE 7.12: LATERALLY AVERAGED FILM COOLING EFFECTIVENESS	111
FIGURE 7.13: TEMPERATURE CONTOURS ON MID-SPAN PLANE FOR $M = 0.7$	113
FIGURE 7.14: TEMPERATURE CONTOURS ON MID-SPAN PLANE FOR $M = 1.1$	114
FIGURE 7.15: TEMPERATURE CONTOURS ON MID-SPAN PLANE FOR $M = 1.5$	115
FIGURE 7.16: VELOCITY PLOT DISTRIBUTIONS ON MID-SPAN PLANE FOR $M = 0.7$	117
FIGURE 7.17: VELOCITY PLOT DISTRIBUTIONS ON MID-SPAN PLANE FOR $M = 1.1$	118
FIGURE 7.18: VELOCITY PLOT DISTRIBUTIONS ON MID-SPAN PLANE FOR $M = 1.5$	119

List of Tables

TABLE 4.1: PLENUM INLET VELOCITY	33
TABLE 5.1: PLENUM INLET VELOCITY	51
TABLE 6.1: PLENUM INLET VELOCITY	80
TABLE 7.1: CASCADE GEOMETRY AND PARAMETERS.....	97
TABLE 7.2: BOUNDARY CONDITIONS	102
TABLE B.1: PROFILE COORDINATES IN BITANGENT-SYSTEM FOR AGTB BLADE.....	127

Nomenclature

Alphabetical

A	Area
a	Semi-minor axis of an ellipse
a'	Semi-minor axis of the ellipse at the cross-sectional area of the CESH
b	Semi-major axis of an ellipse
b'	Semi-major axis of the ellipse at the cross-sectional area of the CESH
C	Closure coefficient
D	Diameter
DR	Density ratio
E	Total energy
H	Height
I	Momentum flux ratio
k	Kinetic energy of turbulence
k'	Thermal conductivity
L	Length
L_{ch}	Chord length
LE	Hole leading edge at the blade
M	Blowing ratio
Ma	Mach number
P	Pressure
P/D	Pitch-to-diameter ratio
Pr	Prandtl number
PS	Pressure side
Re	Reynolds number
S	Strain-rate tensor
SS	Suction side
T	Temperature
u	Velocity
k	Turbulent kinetic energy
t	Time
t'	Cascade pitch
TE	Hole trailing edge at the blade
Tu	Turbulent intensity
y^+	Normalized distance from wall
x, y, z	Cartesian coordinate
x', y', z'	Secondary coordinate system

Greek

Ω	Rate-of-rotation tensor
β	Flow angle
γ	Streamwise ejection angle

δ	Kronecker delta
ε	Turbulent dissipation rate
η	Adiabatic film cooling effectiveness
μ	Dynamic viscosity
ρ	Density
σ_k	Prandtl number for kinetic energy of turbulence
σ_ε	Prandtl number for turbulent dissipation rate
ν	Kinematic viscosity
ω_k	Angular velocity

Subscripts

1	Inlet flow
2	Outlet flow
aw	Adiabatic wall
c	Coolant
ch	Chord
cs	Cross-section
eff	Effective
is	Isentropic condition
PS	Pressure side
s	Staggering
SS	Suction side
t	Turbulent
v	Vane
∞	Freestream (mainstream)

Acronyms

$ACRVP$	Anti-Counter Rotating Vortex Pairs
$AGTB$	Modellschaufel der Arbeitsgemeinschaft Hochtemperaturgasturbine (AG Turbo) Schaufeltyp B (Shovel Model of the Working Group temperature Gas Turbine (Turbo AG) Bucket type B)
$CESH$	Circular Exit Shaped Hole
$CRVP$	Counter-Rotating Vortex Pairs
DES	Detached Eddy Simulation
$DJFC$	Double-Jet Film Cooling
DNS	Direct Numerical Simulation
$EESH$	Elliptical Exit Shaped Hole
LES	Large Eddy Simulation
$RANS$	Reynolds-Averaged Navier-Stokes

<i>RSM</i>	Reynolds-Stress Model
<i>SIMPLEC</i>	Semi-Implicit Method for Pressure-Linked Equations-Consistent
<i>SSSH</i>	Sister Shaped Single-Hole
<i>SST</i>	Shear Stress Transport
<i>ST</i>	Specific thrust
<i>TET</i>	Turbine Entry Temperature
<i>TSFC</i>	Thrust Specific Fuel Consumption

This Page Intentionally Left Blank

1. INTRODUCTION

Modern gas turbine engines are designed to operate at high temperatures in order to elevate the overall efficiency and output power; these temperatures exceed the melting point of the turbine blades' material. Despite advancements in blades' metallurgy including the thermal barrier coating, an effective cooling technique can contribute to obtaining a reasonable lifetime for the turbine blades. The turbine blade can be cooled internally by moving the coolant through passages or by impinging cold jets inside the blade (internal cooling). Moreover, external cooling involves injecting the coolant air flow from discrete holes or slots through the blade's surface, wherein the cooling air flow is extracted from the engine's compressor. As such, a thin blanket of the cooling air flow covers the turbine blades and protects them against the hot gases from the combustion chamber. This method is called film cooling. Over six decades, film cooling has been known as an effective cooling technique to protect the blades from such extreme temperatures.

1.1. RESEARCH MOTIVATION

The performance of a gas turbine engine can be defined by two important parameters which are the thrust specific fuel consumption (TSFC) and the specific thrust (ST). The TSFC is defined as the fuel consumption per unit thrust and the ST is the thrust per unit mass flow rate of air [1]. There has been a continuing tendency to increase the TET in gas turbine industry, either to increase the ST or to reduce the TSFC, in order to increase the engine's performance [2]. An overview on advancements of turbine cooling technology which resulted in obtaining a notable increase in turbine entry temperature (TET) is shown in Figure 1.1 [1]. There has also been a continuous demand to improve film cooling through practices involving the design of innovative hole schemes to increase engine performance. Therefore, by using advanced film cooling schemes, the turbine blades can be more efficiently cooled allowing for higher turbine entry temperatures.

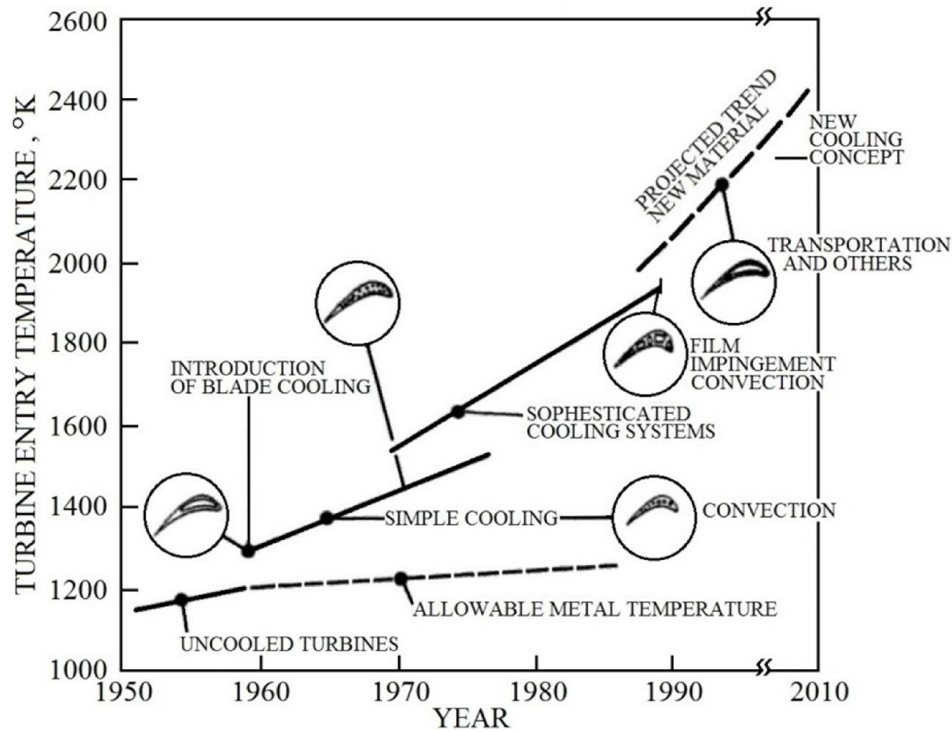


Figure 1.1: Lifetime progression of turbine entry temperature (adopted from [1])

1.2. THESIS OBJECTIVES

Four primary objectives are undertaken for the present study. Each objective has been advanced and further analyzed from the preceding objective. To initialize the research, a novel film hole geometry is developed based on the conventional cylindrical hole; wherein the geometry comprises a circular hole through the blade structure that produces an ellipse at the blade's surface. The inspiration of the initial objective comes from the notion of inverting this conventional cylindrical hole whereby an elliptical hole geometry is extruded from the blade's structure and a circular exit shaped hole (CESH) is produced at the surface. This novel geometry will be numerically analyzed to determine the film cooling effectiveness and flow structure. Moreover, the CESH will be combined with existing sister holes as previously proposed by Ely and Jubran [3], to further validate its performance. The second objective is to modify the spanwise and streamwise locations of the sister holes to evaluate the film cooling performance while considering various locations of the sister holes on a flat plate around the conventional cylindrical hole geometry. To further add to advancements in shaped hole film cooling geometries, the third objective will be to utilise the principles of sister holes and extend them to

sister shaped single-hole configurations, wherein various combinations of sister holes are joined with the primary injection hole to produce a variant shaped hole and analyzed on a flat plate. The fourth and final objective makes use of the results of the previous objective which will then be applied to the leading edge of a turbine blade to evaluate the film cooling performance.

1.3. THESIS OUTLINE

This thesis is comprised of eight chapters; starting with Chapter 1 as the introduction. Chapter 2 provides an overview of film cooling studies on various hole configurations along with the most relevant findings. The governing equations and various Reynolds-Averaged Navier-Stokes (RANS) turbulence models including the standard, RNG and realizable $k-\epsilon$ models and the Reynolds-stress model are presented in Chapter 3. The novel CESH (circular exist shaped hole) film hole configuration under the influence of sister holes is presented in Chapter 4 along with a numerical analysis and investigation on adiabatic film cooling effectiveness and flow structure. In Chapter 5, a numerical parametric study is carried out on modifications of the discrete sister holes' locations. Chapter 6 investigates a numerical analysis on film cooling performance from innovative sister shaped single-holes (SSSH) schemes. The SSSH schemes are evaluated at the leading edge of a cascade turbine blade with two rows of cooling holes in Chapter 7. Finally, the Chapter 8 of this thesis presents the conclusions and recommendations for future work.

2. LITERATURE REVIEW

Over the history of film cooling, numerous studies have been carried out to improve its performance. Various aspects of film cooling have been investigated. Among them the geometrical parameters are considered as the most influential factors in film cooling performance. For more than three decades, a migration has been made from conventional film cooling through cylindrical holes to novel film cooling schemes. Advanced film cooling configurations became a reality due to the advancement in manufacturing techniques. It is important to mention here that the major part of this migration is still under development and is in its transitional stage. An overview of film cooling studies on various hole configurations will be presented in the following sections, along with the most relevant findings.

2.1. CYLINDRICAL FILM COOLING HOLES

The discrete cylindrical hole (round hole) geometries are considered as the conventional and most commonly used film cooling schemes. Researchers have conducted numerous studies both numerically and experimentally on film cooling. Geometric parameters, such as length-to-diameter ratio (L/D), film cooling hole diameter, injection angle and pitch-to-diameter ratio (P/D) have a significant effect on flow structure, and consequently on film cooling effectiveness [4]. The pitch-to-diameter ratio is defined as the ratio of the lateral spacing between two holes in a row of injection holes to diameter of the injection hole.

Lutum and Johnson [5] carried out an experimental study on the influence of the length-to-diameter ratio for a row of cylindrical holes with the inclination angle of 35° . They performed the experiments for various length-to-diameter ratios of 1.75, 3.5, 5, 7 and 18 for a range of blowing ratios, $M = DR(V_c/V_\infty)$, from 0.52 to 1.56, where $DR = \rho_c/\rho_\infty$. In general, they found that the film cooling effectiveness decreases when increasing the length-to-diameter ratio from 1.75 to 5, wherein the lowest film cooling effectiveness was found for $L/D = 1.75$.

The effect of large angle injection for the flat plate film cooling flow on the adiabatic effectiveness, thermal and velocity fields is investigated by Kohli and Bogard [6]. The obtained

results for the hole with 55° inclination angle were compared to the inclination angle of 35° for blowing ratios of 0.5 and 1. They found that increasing the injection angle to 55° can result in a slight decrease in the film cooling effectiveness results for the low blowing ratio of 0.5, while a significant reduction in the effectiveness was observed for the high blowing ratio of 1. Moreover, they reported a notable diffusion of the cooling jet for the 55° injection angle as compared to the 35° in the near-hole region.

Baldauf et al. [7] studied adiabatic film cooling on a flat plate from a row of cylindrical holes. They found that the hole spacing factor plays an important role in the film cooling effectiveness results. The lateral spacing of $P/D = 2, 3$ and 5 is investigated. Results indicated that the film cooling effectiveness decreased while increasing the pitch-to-diameter ratio. This is attributed to the reduction in lateral interaction of the jets. They also proposed a correlation for the prediction of the laterally averaged film cooling effectiveness.

The effect of film cooling flow parameters such as density ratio, velocity ratio, momentum flux ratio and blowing ratio on the adiabatic film cooling effectiveness is experimentally investigated by Sinha et al. [8]. The measurements on a flat plate are carried out downstream of a row of cylindrical holes with an inclination angle of 35° and a length-to-diameter ratio of 1.75. The laterally averaged film cooling effectiveness is found to be dependent on density and momentum flux ratios. Increasing the momentum flux ratio and decreasing the density ratio resulted in a decrease in the coolant spread over the blade surface.

2.2. FILM COOLING THROUGH A SLOT

Desirable film cooling can be achieved through a continuous slot hole on the turbine blade. These slots can provide a two-dimensional uniform flow over the blade. Many efforts have been made to put this film cooling configuration into practice. However, some restrictions such as aerodynamics, thermal and mechanical stress, and most importantly, the manufacturing issue, made the slots' geometry almost infeasible [9].

The converging slot hole idea, the console, has been introduced by Sargison et al. [10-12]. They experimentally compared the cooling performance of a single row of consoles with cylindrical, fan-shaped and slot holes. Improvement in cooling performance and aerodynamic efficiency was achieved when using the console hole configuration. Although, the coolant air flow tends to adhere more to the surface through the use of the console, the performance of this

method is highly dependent on the number of consoles in each array. Another experimental test on a converging slot hole has been performed by Liu et al. [13]. Their results, compared with the cylindrical holes, indicated that the influence of the passage vortex on the jets from the consoles is weaker than that of the cylindrical holes. As expected the cooling coverage area of the console was much larger than that of the cylindrical hole for both single and multiple rows of the holes. However, for the lower diffusion angle of the console, the detachment of the coolant caused lower film cooling effectiveness in the vicinity of the holes. A detailed flow and thermal analysis on the converging slot hole geometry has been carried out by Azzi and Jubran [14]. They concluded that the spanwise spreading of the thermal field can be correctly predicted through the application of the anisotropic eddy-viscosity/diffusivity model. In comparison with the cylindrical and shaped hole configurations, they also confirmed that the console geometry provides a promising cooling performance.

Apart from the continuous slots, Bruce-Black et al. [15] performed an experimental study on several practical slot-like film cooling configurations on the suction side (SS) of a scaled-up turbine vane. The coolant flow was injected through the slot holes with an inclination of 30° to the mainstream flow, which were fed with cylindrical impinging holes. By increasing the width of the slots at a blowing ratio equal to or greater than 1.8, an increase in the adiabatic film cooling effectiveness was observed. Furthermore, a greater influence is noticed on the spatially averaged adiabatic effectiveness when the depths of the slots are changed instead of their widths.

Liu et al. [16] performed a numerical and experimental study on a new slot film cooling hole, called a waist-shaped slot hole. The momentum flux ratio, $I = DR(V_c/V_\infty)^2$, of around 2 was found as the optimum momentum ratio in the upstream region for the waist-shaped slot hole based on the laterally averaged film cooling effectiveness results. Wherein, the density ratio (DR) is the ratio of the density of cooling air flow (ρ_c) to the density of mainstream air flow (ρ_∞). Comparison of the obtained results with two kinds of console holes showed a better flow resistance characteristic for the waist-shaped slot hole than that of the console with a small exit-entry area ratio.

Moreover, a combination of a cylindrical hole and slot at the exit plane of the jet, called a trenched shaped hole, has been used to enhance film cooling performance. Further modifications such as applying a lateral or forward diffusion to the cylindrical hole before reaching the slot were also proposed and investigated by Baheri et al. [17]. Numerical analysis on various

configurations at a blowing ratio of 1.1 revealed that the trenched shaped hole mainly decreases the jet lift-off effect right after the injection. The jet lift-off effect is schematically shown in Figure 2.1. The coolant also tends to adhere more to the blade's surface. In addition, less improvement is achieved through the trenching on the pressure side (PS) of the blade as compared with the suction side [17]. In general, they reported that the trenched shaped holes provide a considerable improvement in lateral film cooling effectiveness on both pressure and suction sides than other examined geometries. Detailed experimental study on trench hole configurations can be found in the work of Way and Bogard [18] and Lu et al. [19].

A dual trench configuration has recently been developed by Abdala et al. [20], and is formed by a wider trench and a secondary narrower trench that is extruded from the wider one. The dual trench hole increased the lateral spreading of the coolant and reduced the momentum of the exit flow; hence, film flow covers more area on the blade's surface. Interestingly, the adiabatic effectiveness increased as the blowing ratio increased. Also, higher film cooling effectiveness values are achieved for the dual trench case in comparison with the regular trench, laidback fan-shaped, fan-shaped and cylindrical hole for different blowing ratios [20].

2.3. FLOW STRUCTURE CONTROL SCHEMES

The interaction between an injected jet and a crossflow results in a complex flow structure, including various types of vortices downstream of the injection hole. Among them, counter rotating vortex pairs' (CRVP) structure (also known as kidney vortices) has the most detrimental effect on film cooling performance in the streamwise injection flow [21]. The jet lift-off effect due to CRVP is considered and believed to be one of the major contributors in reducing film cooling performance [22]. The mechanism of the CRVP increases the aerodynamic mixing of the jet with the crossflow and causes a delay in the reattachment of the cooling jet to the blade's surface due to the jet lift-off effects.

Fric and Roshko [23] studied the various vortices that form in the jet in the crossflow, including jet shear-layer vortices at the perimeter of the bending jet, the developing counter-rotating vortex pairs, horseshoe vortices on the wall and the wake vortices extending from the wall to the jet. A schematic of these vortices is depicted in Figure 2.1.

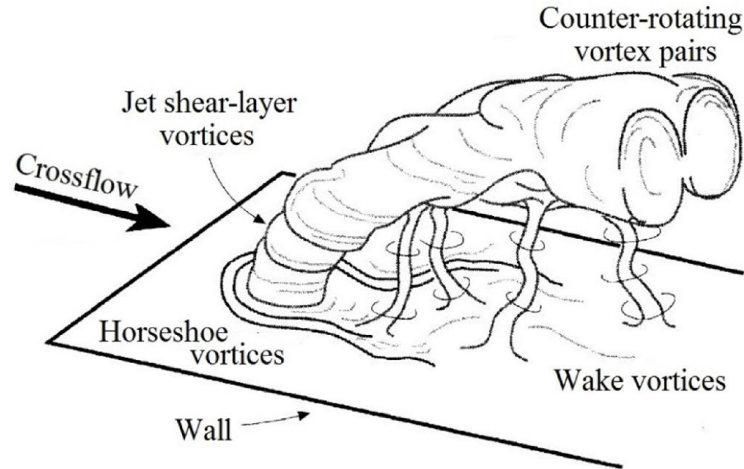


Figure 2.1: Four types of vortical structures associated with jet in crossflow near-field [23]

Several attempts have been made in the literature to increase the film cooling performance through flow structure control schemes. Advancements in shaped hole film cooling has led researchers to design holes with a focus on reducing the effect of CRVP.

In order to examine the effect of the hole exit geometry of crossflow jets, Haven and Kurosaka [24] ran water tunnel experiments for four different hole shapes including circular (round), elliptical, square and rectangular shapes, with an injection angle of 90° and the same cross-sectional area. They noted that the hole geometry and especially the exit shape of the hole have a strong effect on the near flow field characteristics of the counter-rotating vortex pairs. It was also mentioned that the exit jet from the circular hole improves the jet adhesion to the wall surface and reduces the jet lift-off effect.

Another experimental study on elliptical jet in crossflow which was later conducted by New et al. [25] showed that the effects of an elliptical jet exit orientation are only significant in the near-field jet region. They also reported that for the low aspect ratio (the ratio of spanwise to streamwise length of the jet exit shape) case, two counter-rotating vortices are initially formed at the sides of the jet, while only one CRVP is formed throughout the jet. Note that the low aspect ratio case can be achieved, when the semi-major axis of the ellipse is aligned with the crossflow.

A numerical analysis of a hybrid scheme with different outlet configurations namely trapezoidal, elliptical, rectangular and square is carried out by Ghorab [26]. It is concluded that the highest overall area-averaged effectiveness with less secondary flow rate and pressure losses were achieved for the hybrid trapezoidal and square schemes at high blowing ratios.

An experimental effort on film cooling hole geometry with various cross-sectional area was made by Takahashi et al. [27]. The test was run for a circle, three rectangles and two oval holes at several blowing ratios. Note that in order to perform the experiment with a simple method, the film cooling jet was heated instead of the mainstream flow. Higher film cooling effectiveness was achieved for the rectangular holes compared with the circular hole. This was caused by greater spreading of the film cooling jet over the target surface. Nonetheless, the oval shaped hole outperformed all the other configurations, and was reported as an easy geometry to open through the real gas turbine blade [27].

An experimental study on compound angled film cooling holes, which was conducted by Aga et al. [28], showed a considerable decrease in the strength of the CRVP structure. The flow structure was reported based on a row of cylindrical holes at an inclined angle of 20° to the flat plate surface and a compound angle of 45° . Interestingly, they reported no jet lift-off at the high blowing ratio of 3 for their geometry. Also, through compound angled hole injection more coolant spreading was observed, compared with the streamwise coolant injection.

A considerable decrease in the strength of the CRVP when using the compound angled holes has been observed in the experimental work of Aga et al. [28]. For the high blowing ratio of 3, no jet lift-off is reported. Moreover, the coolant is spread more in the spanwise direction for the compound angled holes as compared with the streamwise injection. A numerical simulation on the compound angle and detailed flow physics is carried out by McGovern and Leylek [29] and Gräf and Kleiser [30].

A vortex generator system is proposed by Rigby and Heidmann [31], placing a delta shaped object downstream of the injection hole. They determined that the vortex generator was very effective at generating ACRVP (anti-counter rotating vortex pairs); as a result, the coolant pushed towards the wall surface and spread out along the wall. Similar results have also been reported by An et al. [32] for using a vortex generator by placing a short crescent-shaped hole downstream of a cylindrical cooling hole.

Several studies on the physics of the flow in an elliptical duct have been carried out by researchers. Among them, Cain and Duffy [33] performed an experimental study on turbulent flow in an elliptical duct. They found that the fully turbulent flow occurs approximately $30D$ downstream of the duct entrance, where D was defined as the hydraulic diameter of the elliptical duct. Velusamy et al. [34] reported that the pressure drop over an elliptical duct is less than what

occurs in a circular duct. Voronova and Nikitin [35] implemented a DNS study on the turbulent flow in an elliptical pipe at a Reynolds numbers of 4,000. They found that in order to produce the basic turbulent characteristics for an elliptical pipe with the semi-axis ratio (b'/a') of 2, the length of $6b'$ is enough, where b' and a' are semi-major and semi-minor axes of the elliptical section, respectively [35].

2.3.1. Shaped Holes

Other than the slot scheme, cylindrical and other shapes of film cooling holes, the idea of the shaped hole geometry has been proposed as one of the most practical advancements in film cooling technology [9]. Bunker [9] performed a comprehensive review on the literature concerning the performance of shaped holes, and examined the origin of such film holes. One of the earlier research efforts in shaped-hole film cooling has been carried out by Goldstein et al. [36]. The experiments were carried out on shaped and cylindrical film cooling holes. The passage of the shaped hole started with a circular cross-sectional pipe that became wider by an angle of 10° to each side as it approached the blade's surface. The increased film cooling effectiveness with the shaped holes can be explained by the decrease in the mean velocity of the secondary flow at the jet exit. As a result, the coolant hugged the blade's surface due to the Coanda effect at the jet exit, and higher film cooling effectiveness was achieved.

Bunker [9] classified the shaped holes into four hole categories, as shown in Figure 2.2.

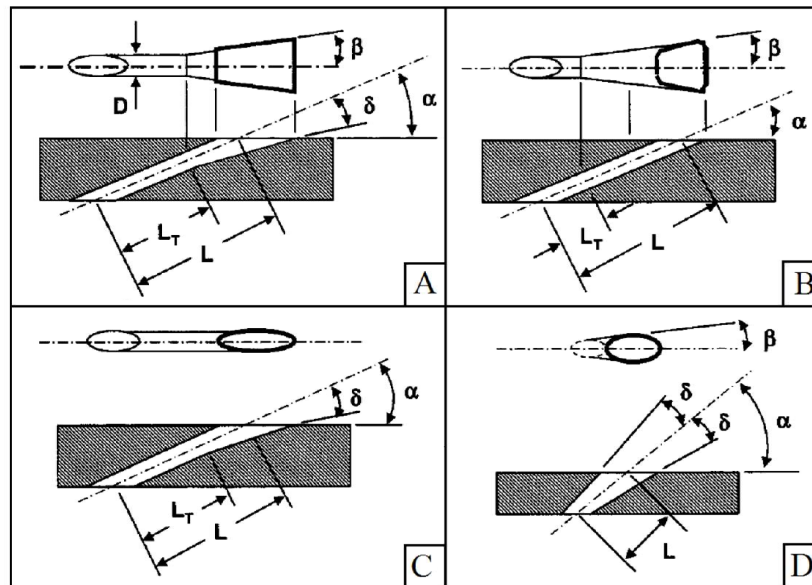


Figure 2.2: Four types of shaped film cooling holes [9]

Different expansions in shaped holes including the lateral expansion or expansion into the surface can provide a fan-shaped or laidback hole, respectively. Based on that, the first category (type A) contains both expansions; the second and third categories (types B and C) include only lateral and laidback expansions, respectively; and the last category (type D) of the shaped holes contains an equal expansion from the inlet around the hole centerline, which produces a conical shaped hole.

Saumweber and Schulz [37, 38] compared the cooling performance of a fan-shaped hole with a 14° expansion angle to a simple cylindrical hole. They summarized that the crossflow Mach number plays an important role at the inlet of the cooling hole. Furthermore, the performance gained from the fan-shaped hole was overestimated as compared to the cylindrical hole for low turbulence levels and low Mach numbers, where the effect of large mainstream turbulence intensity was always detrimental to the fan-shaped hole case [38]. Saumweber and Schultz [39] also investigated the effect of some geometric variations on film cooling performance from fan-shaped cooling holes. The most important geometrical parameters of diffuser holes were found to be the expansion angle of the diffuser, the inclination angle of the hole and the length of the cylindrical part of the hole entrance. A numerical simulation of the optimization of a fan-shaped hole using SST turbulence model is performed by Lee and Kim [40]. They chose the injection angle, lateral expansion angle and length-to-diameter ratio as the design variables; wherein maximizing the spatially averaged film cooling effectiveness was their objective. Finally, they concluded that a fan-shaped hole with an injection angle of 40.34° , a lateral expansion of 21.83° and a length to-diameter-ratio of 7.45 is the optimal shape for the blowing ratio of 0.5. Montomoli et al. [41] proposed an advanced fan-shaped hole which is called the double backward facing step. Through experimental and numerical analysis, a minimum of 30% increase in the laterally averaged film cooling effectiveness was observed over the baseline case. An extensive set of experimental studies on 16 different fan-shaped film cooling holes over a wide blowing ratio range (0.5 to 2.5) was carried out by Gritsch et al. [42]. Various geometrical parameters such as inlet-to-outlet area ratio, hole coverage ratio, hole pitch ratio, hole length and orientation of compound angle have been investigated for a wide range of blowing ratios from 0.5 to 2.5. They found that the effect of coverage ratio, area ratio and hole length-to-diameter ratio were negligible on film cooling effectiveness, while, as expected, the

pitch-to-diameter ratio had a considerable effect on film cooling performance; this parameter is responsible for defining the amount of coolant spent per unit span [42].

Lee and Kim [43] proposed a new shaped hole scheme based on the fan-shaped film cooling hole, which provides similar film cooling effectiveness results at the low blowing ratio of 0.5 as compared to the fan-shaped hole. However, the novel shaped hole outperformed the fan-shaped hole at the high blowing ratio of 2.5 in terms of more lateral spreading of the CRVP. As a result, the central pair of the vortices has been reduced considerably and consequently, higher values of the lateral film cooling effectiveness are achieved.

Takeishi et al. [44] provided an experimental study on film cooling through a swirling coolant flow method. They applied this method to circular and shaped coolant hole cases. Two inclined impinging jets provide the swirling motion inside of the plenum and helped to inject the coolant with an angular momentum into the mainstream flow. As a result, the coolant spread more into the spanwise direction and adhered more to the blade's surface due to the disappearance of the kidney vortex structure [44]. They also found that the impinging nozzle angle of 10° with the same shaped hole geometry as the optimum configuration offered the maximum value for film cooling effectiveness.

A film cooling geometry called the louver hole scheme is proposed by Zhang and Hassan [22] wherein the coolant has to pass through a bend before exiting the blade. The louver scheme successfully reduced the jet lift-off and provided more uniform protection of coolant on the blade; consequently, the thermal stress is considerably reduced [22].

Baheri et al. [17] performed a numerical simulation on six different shaped hole configurations on the leading edge of a turbine blade and compared the results with the cylindrical hole. They concluded that kidney vortices are strong for the cylindrical hole on the suction side and the jet lift-off considerably reduces the film cooling effectiveness. Due to the reversed flow on the pressure side, less jet lift-off has been observed. Although using the trenched forward-diffused shaped holes increased the strength of the CRVP on the suction side, it provided more spread flow in the lateral direction as compared with the regular shaped holes.

Liu et al. [45] introduced two shaped holes named dumbbell and bean holes. These holes provided an overall improvement of 33% in the predicted laterally averaged film cooling effectiveness results as compared to the fan-shaped film cooling holes. One of the purposes of their proposed shaped holes' design is to counter the CRVP by generating the ACRVP, which are

also called the anti-kidney vortices. The circular exit of the regular hole has been split into two smaller circles for the dumbbell shaped hole. This helped generate the anti-kidney vortices and resulted in the highest film cooling performance for this shaped hole. Kim et al. [46] performed a numerical study to investigate the performance of four different shaped holes, namely fan-shaped, crescent, louver and dumbbell shaped holes, as demonstrated in Figure 2.3. Overall, the dumbbell shaped hole demonstrated the best spatially averaged film cooling effectiveness for a wide range of blowing ratios from 0.5 to 2. In contrast, the efficiency of the louver shaped hole proved only satisfactory. The crescent hole showed wide spreading of the coolant in the lateral direction at the lower blowing ratio of 0.5.

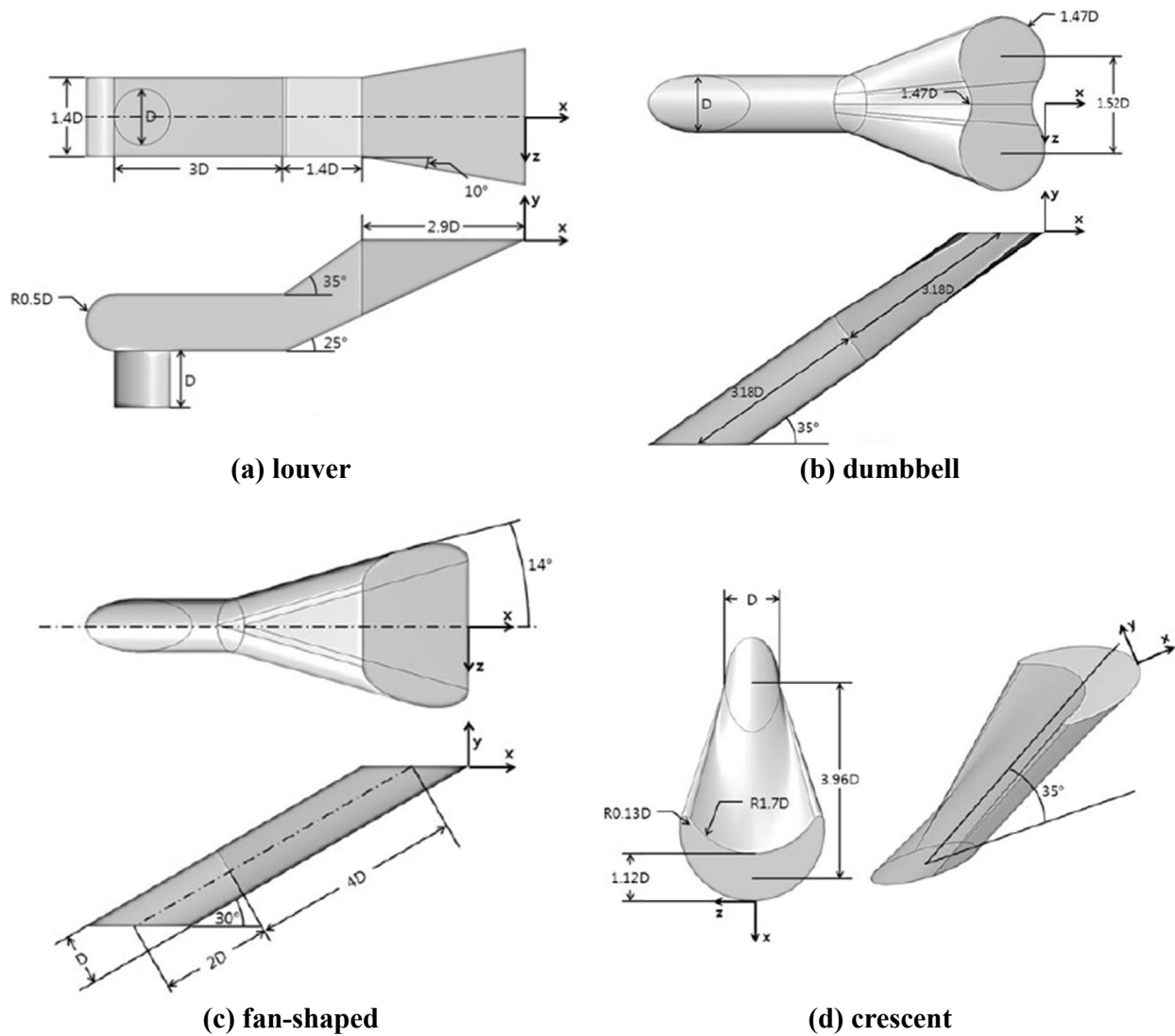
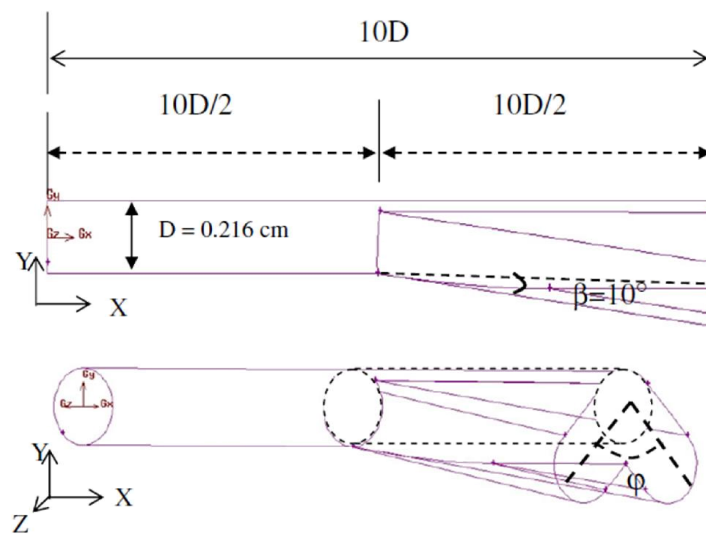


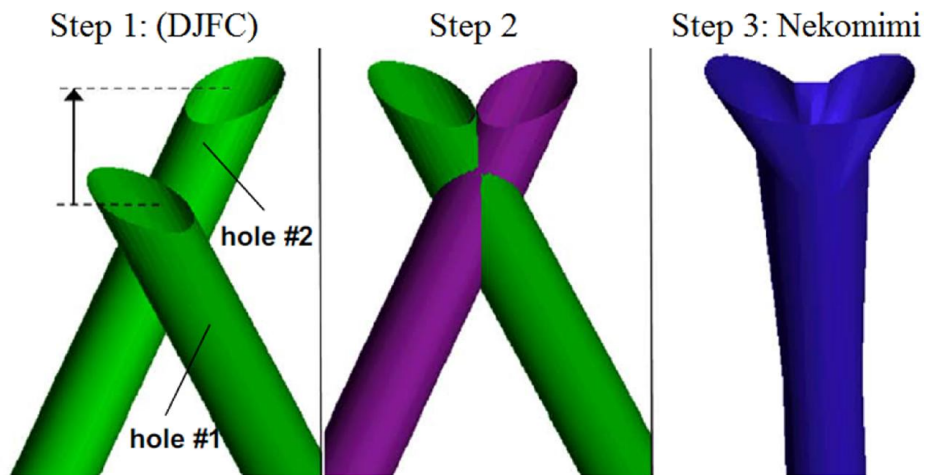
Figure 2.3: Schematic of (a) louver, (b) dumbbell, (c) fan-shaped and (d) crescent shaped holes [46]

Yusop et al. [47] evaluated the film cooling performance of a heart-shaped hole with crown angles of 60° and 90° , as depicted in Figure 2.4(a). In comparison, the shaped hole with a crown angle of 60° provided higher film cooling effectiveness values. They also found considerable reduction in the strength of the CRVP and jet lift-off as compared with the cylindrical hole.

Based on the idea of double-jet film cooling (DJFC), Kusterer et al. [48] merged two holes and a new configuration, named Nekomimi, has been studied numerically and experimentally. The design concept of Nekomimi configuration is shown in Figure 2.4(b).



(a) heart-shaped hole



(b) DJFC and Nekomimi

Figure 2.4: Design concept of (a) heart-shaped hole [47] - (b) DJFC and Nekomimi [48]

Simulations showed that the Nekomimi technology provides higher laterally averaged film cooling effectiveness compared to the cylindrical, trenched, double-jet film cooling and shaped hole configurations. Furthermore, as a result of the anti-kidney vortices generated from the ear-shaped part of the hole geometry, the jet lift-off decreased and more attached flow was observed downstream of the injection hole.

Further improvements to the Nekomimi shaped hole were carried out in their recent studies [49, 50], where the main focus of the design modification was based on the development of the Anti-CRVP (ACRVP) generated from the shaped hole to increase the film cooling efficiency. The influence of various geometric and aerodynamic parameters on Nekomimi, DJFC and anti-vortex holes has been investigated in the experimental work of Han et al. [51].

2.3.2. Anti-Vortex Holes

Decreasing the detrimental effects of CRVP for the film cooling flow has also been studied through methods involving anti-vortex holes' schemes. This concept has been initiated by Javadi et al. [52] by placing two smaller holes downstream of the main hole; this scheme was named combined triple jets, as illustrated in Figure 2.5(a). Note that the jet was injected normal to the crossflow through the rectangular holes. The ACRVP generated from the extra holes countered the CRVP and reduced the mixing of the injected flow with the crossflow. Moreover, uniform distribution of the coolant film and reduction of skin friction drag have been reported by them in [53].

Kusterer et al. [54] performed an analysis on double-jet film cooling by adding a neighbour hole upstream of the main cooling hole with different lateral positions (see Figure 2.4(b), step 1). They found an optimum arrangement for holes that led to the generation of an anti-vortex system. As a result, a higher value of film cooling effectiveness and more attached coolant to the wall was achieved through the use of double-jet film cooling [54]. They concluded that the double-jet keeps the coolant air attached to the wall and more distributed in the lateral direction; hence, high values for the film cooling effectiveness results were obtained.

Heidmann and Ekkad [55] proposed an anti-vortex scheme with two additional anti-vortex holes that branched-out from the main cooling pipe, as shown in Figure 2.5(b). Although they recommended various geometrical parameters, in order to get higher film cooling

effectiveness and more attached coolant flow to the surface, they reported that the optimum design depends on the application.

An experimental study on the anti-vortex hole has been carried out by Dhungel et al. [56]. They showed that the anti-vortex holes are closer to the main film cooling hole and are developing from the base of the main hole, better film cooling performance can be achieved as compared to other anti-vortex schemes. Soe et al. [57] carried out a numerical analysis on various anti-vortex configurations for a range of blowing ratios of 0.5 to 5. The spanwise film cooling effectiveness of anti-vortex configuration was higher than that of a single cylindrical hole for all blowing ratios. In general, their results were in agreement with the work of Heidmann and Ekkad [55]. For all blowing ratios the spanwise film cooling effectiveness of anti-vortex configuration was higher than that of a single cylindrical hole for all blowing ratios [57]. In addition, Yao et al. [58] performed a numerical investigation on breached-out anti-vortex holes. Similar to the previous works in the field of anti-vortices, the strength of the kidney vortices were decreased and higher film cooling effectiveness was achieved compared to the single cylindrical hole. They also reported a lower heat transfer coefficient by placing the exit of the branched-out holes in line with the main cylindrical hole.

The sister holes concept has been suggested by Ely and Jubran [3, 59, 60] by placing smaller discrete holes in the upstream and/or downstream region of the main film cooling hole. The top view of up/downstream sister holes is depicted in Figure 2.5(c). Sister holes provided higher performance for film cooling at higher blowing ratios of 1 and 1.5 in comparison with lower blowing ratios of 0.2 and 0.5. Similar to previous works in the field of anti-vortex film cooling, controlling the effect of CRVP by generating vortices through the sister holes, that are rotating in the opposite direction to CRVP, caused more adhesion of coolant flow to the blade's surface. Additionally, in order to find an optimal discrete sister hole configuration, Ely and Jubran [61] found the left/right sister holes combination as the most optimal configuration for the long hole film cooling ($L/D = 5$), while for the short holes ($L/D = 1.16$) the up/downstream combination (i.e., four active discrete sister holes downstream and upstream of the main hole) provided better cooling performance [62].

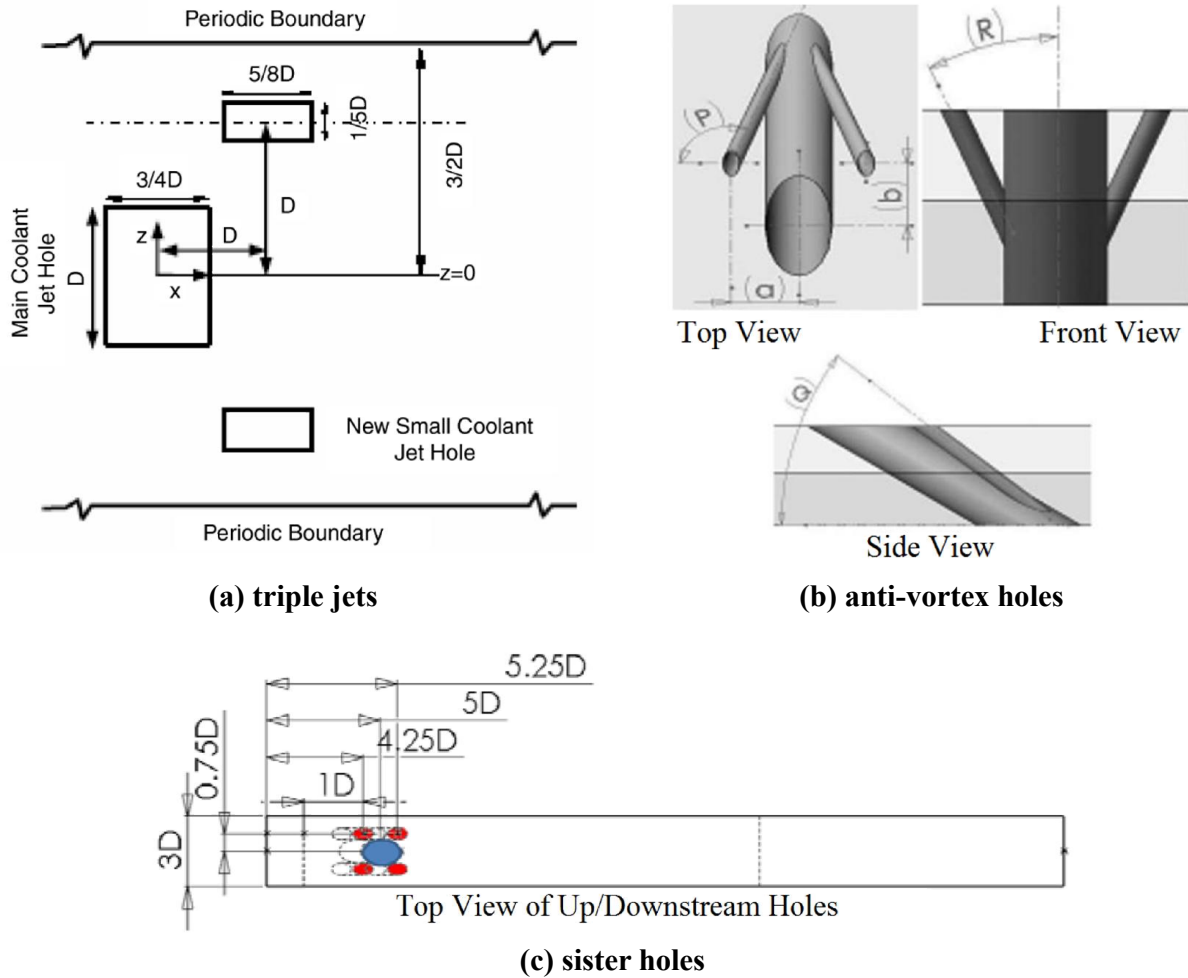


Figure 2.5: Configuration of (a) triple jets [53], (b) anti-vortex holes [56] and (c) sister holes [62]

2.4. NUMERICAL APPROACHES

Numerical simulation has always been of major interest as a useful tool for researchers, in order to reduce the cost of running an experimental setup. This issue of the film cooling flow was much more challenging than more conventional CFD problems, due to the complexity of the field, and the large gradients in the thermal and flow field. Various turbulence models have been introduced over the years, to expectantly provide a desirable accuracy on predicted results. In terms of cost and accuracy, the RANS-based models have proved effective for a number of fluid flow problems.

The limitations and performance of four different two-equation turbulence models in predicting film cooling effectiveness were studied by Hassan and Yavuzkurt [63]. The standard,

RNG and realizable $k-\varepsilon$ models, as well as the standard $k-\omega$ model, were used in their simulations. They found that the standard $k-\omega$ model was unable to provide satisfactory results on the prediction of film cooling effectiveness. Comparatively, the RNG and realizable $k-\varepsilon$ models showed a better prediction for the spreading of the coolant air in the lateral direction compared with the standard $k-\varepsilon$ model. In general, the standard $k-\varepsilon$ model performed better in comparison with other models [63].

Walters and Leylek [21] applied the standard $k-\varepsilon$ model, with the two-layer approach instead of using the wall function, to model a simple cylindrical hole configuration. Although, the two-layer model increased the computational cost of the simulation, its prediction for the recirculation zone (close to the jet exit) was more satisfying. Similar results were achieved downstream of the jet for both near-wall approaches [21].

Zhang and Hassan [22] performed a detailed study on RANS simulation of film cooling through a common cylindrical hole. They concluded that the quality of the grids and the turbulence models had a considerable effect on the simulation outcomes. Accordingly, they found an excellent agreement between the predicted results and the available experimental data for the cylindrical hole using the realizable $k-\varepsilon$ model combined with the standard wall function.

The performance of three different two-equation turbulence models, namely standard $k-\varepsilon$, $k-\omega$ and SST $k-\omega$, in predicting the film cooling effectiveness on a rotating blade has been investigated by Tao et al. [64]. The numerical film cooling effectiveness results were overpredicted by all three models, when compared with the experimental data. Nevertheless, predicted results with the $k-\omega$ models were more satisfying than that with the standard $k-\varepsilon$ model [64].

Harrison and Bogard [65] have evaluated the performance of the realizable $k-\varepsilon$, $k-\omega$ and Reynolds-stress model (RSM) for predicting the film cooling heat transfer and effectiveness. The centerline film cooling effectiveness and lateral effectiveness were well predicted by the realizable $k-\varepsilon$ model and the $k-\omega$ model, respectively. The only advantage of the Reynolds-stress model was in predicting the heat transfer coefficient, while more computational resources were needed to apply this model.

Recently, Johnson et al. [4] investigated the effect of the grid refinement on flat plate film cooling. It has been found that a lack of proper grid refinement in the near-hole region has a significant effect on the accuracy of the predicted results. However, it cannot compensate for the

errant natures of the isotropic $k-\epsilon$ models which overpredict the centerline film cooling effectiveness and wall normal contours, and underpredict the laterally averaged film cooling effectiveness[4]. Further to this, in terms of the centerline film cooling effectiveness results, overprediction of the realizable $k-\epsilon$, SST $k-\omega$ and Spallart-Allmaras models have also been reported in the study of Na et al. [66].

In RANS models, the temporal and spatial fluctuations are represented in the turbulence model, and only the time-averaged mean flow is solved. Hence, the validity of the turbulence model controls the accuracy of the results [67]. Advancements in computing technology in the past decades helped researchers to look into computer-intensive approaches to increase the accuracy level of numerical simulations, such as large eddy simulation (LES) and direct numerical simulation (DNS). In the LES approach, the large scale eddies are solved and a sub-grid scale solver solves the smaller scale turbulence. Examples of LES film cooling simulation can be found in the work of Tyagi and Acharya [68], Konopka et al . [69] and Johnson and Shyam [70]. Detached eddy simulation (DES) is considered as a bridge between the RANS and LES approaches. The grid size is not fine enough to apply the LES (usually near wall region), and a RANS based model is used to model this region instead. While for high Reynolds number regions, DES model performs similar to the LES approach [71].

3. GOVERNING EQUATIONS AND TURBULENCE MODELING

Numerical simulations in the present study are performed using ANSYS FLUENT 14.0.0 [72]. Various Reynolds-Averaged Navier-Stokes (RANS) turbulence models including the standard, RNG and realizable k- ϵ models and the Reynolds-stress model are used to model the flow field. The computational cost for the RANS-based turbulence models is considerably lower compared with other numerical approaches such as LES or DNS. In the following chapters, it will be seen that the level of accuracy for the obtained results, for example, with the realizable k- ϵ is satisfactory. This chapter outlines the governing equations together with the turbulence models used in the present investigation. Further details can be found in [72].

3.1. GOVERNING EQUATIONS

The time averaged form of the continuity, momentum and energy equations can be written as follows [72]

$$\frac{\partial}{\partial x_i}(\rho \bar{u}_i) = 0 \quad (3.1)$$

$$\frac{\partial}{\partial x_j}(\rho \bar{u}_i \bar{u}_j) = -\frac{\partial \bar{p}}{\partial x_i} + \frac{\partial}{\partial x_j} \left[\mu \left(\frac{\partial \bar{u}_i}{\partial x_j} + \frac{\partial \bar{u}_j}{\partial x_i} - \frac{2}{3} \delta_{ij} \frac{\partial \bar{u}_l}{\partial x_l} \right) \right] + \frac{\partial}{\partial x_j}(-\rho \overline{u'_i u'_j}) \quad (3.2)$$

$$\frac{\partial}{\partial x_i}[\bar{u}_i(\rho E + \bar{p})] = \frac{\partial}{\partial x_j} \left(k_{eff} \frac{\partial \bar{T}}{\partial x_j} + \bar{u}_i (\tau_{ij})_{eff} \right) \quad (3.3)$$

The effective thermal conductivity (k_{eff}) in the energy Equation (3.3) for the standard and realizable k- ϵ and Reynolds-stress models is defined in Equation (3.6).

$$k_{eff} = k' + \frac{c_p \mu_t}{Pr_t} \quad (3.4)$$

where k' is the thermal conductivity and Pr_t is the turbulent Prandtl number with the default value of 0.85.

In addition, the deviatoric stress tensor $(\tau_{ij})_{eff}$ is defined as

$$(\tau_{ij})_{eff} = \mu_{eff} \left(\frac{\partial \bar{u}_i}{\partial x_j} + \frac{\partial \bar{u}_j}{\partial x_i} \right) - \frac{2}{3} \mu_{eff} \frac{\partial \bar{u}_k}{\partial x_k} \delta_{ij} \quad (3.5)$$

where $\mu_{eff} = \mu + \mu_t$.

Note that since in the present study a steady analysis of the simulations is carried out, all the partial derivatives with respect to time in the governing equations are set to zero. Other assumptions throughout the simulations in the present study are considered based on the experimental setup conditions such as three-dimensional, viscous and turbulent flow as well as single phase, for air as the working fluid. Furthermore, no source of heat or fluid generation is considered, and negligible gravitational force is also assumed. Moreover, for the flat plate film cooling simulations the working fluid is considered as incompressible ideal gas, while for the cascade blade's simulation the compressibility effect has been taken into consideration. Note that the term including the buoyancy effect is also ignored in the transport equations [73].

It can be seen that in the Reynolds-Averaged Navier-Stokes equations (i.e., Equations (3.1) and (3.2)) an additional term $(-\rho \overline{u'_i u'_j})$ appears which is called the Reynolds stress tensor. In order to close the equations this term has to be modeled.

The common method to model the Reynolds Stress tensor is Boussinesq hypothesis as defined in Equation (3.6), which is used in k- ϵ turbulence models [74].

$$-\rho \overline{u'_i u'_j} = \mu_t \left(\frac{\partial \bar{u}_i}{\partial x_j} + \frac{\partial \bar{u}_j}{\partial x_i} \right) - \frac{2}{3} \left(\rho k + \mu_t \frac{\partial \bar{u}_k}{\partial x_k} \right) \delta_{ij} \quad (3.6)$$

where μ_t is the turbulent viscosity that will be computed as a function of k and ε in k - ε turbulence models.

3.2. STANDARD $k - \varepsilon$ MODEL

The standard k - ε model proposed by Launder and Spalding [75] is a semi-empirical model based on model transport equations for the turbulent kinetic energy (k) and its dissipation rate (ε), which can be obtained from transport Equations of (3.7) and (3.8), respectively.

$$\frac{\partial}{\partial x_i}(\rho k \bar{u}_i) = \frac{\partial}{\partial x_j} \left[\left(\mu + \frac{\mu_t}{\sigma_k} \right) \frac{\partial k}{\partial x_j} \right] + G_k - \rho \varepsilon - Y_M \quad (3.7)$$

$$\frac{\partial}{\partial x_i}(\rho \varepsilon \bar{u}_i) = \frac{\partial}{\partial x_j} \left[\left(\mu + \frac{\mu_t}{\sigma_\varepsilon} \right) \frac{\partial \varepsilon}{\partial x_j} \right] + \left(G_k C_{1\varepsilon} \frac{\varepsilon}{k} \right) - \rho C_{2\varepsilon} \frac{\varepsilon^2}{k} \quad (3.8)$$

where σ_k and σ_ε are the Prandtl numbers for k and ε , respectively.

The generation of turbulent kinetic energy due to the mean velocity gradients is represented by G_k in the k and ε transport equations, as shown in the following equation

$$G_k = -\rho \overline{u'_i u'_j} \frac{\partial \bar{u}_j}{\partial x_i} \quad (3.9)$$

The compressibility effect is considered as Y_M in the k transport equation, where for an incompressible flow it will be ignored. Modeling of this term (Y_M) can be expressed as follows

$$Y_M = 2\rho\varepsilon(Ma)_t^2 \quad (3.10)$$

where $(Ma)_t$ is the turbulent Mach number and can be defined as $(Ma)_t = \sqrt{k/a^2}$ and a is the speed of sound ($\sqrt{\gamma RT}$).

In the standard k- ε model the turbulent viscosity can be computed as follows

$$\mu_t = \rho C_\mu \frac{\varepsilon^2}{k} \quad (3.11)$$

where the default constants in Equations (3.7), (3.8) and (3.9) are

$$C_{1\varepsilon} = 1.44, \quad C_{2\varepsilon} = 1.92, \quad C_\mu = 0.09, \quad \sigma_k = 1.0, \quad \sigma_\varepsilon = 1.3$$

3.3. RNG $k - \varepsilon$ MODEL

Using the renormalization group (RNG) method, the k- ε turbulence model is derived from the instantaneous Navier-Stokes equations. This results in a model with different constants than that of the standard k- ε model where additional terms and functions exist in the transport equations for k and ε transport equations [72], as shown in Equations (3.12) and (3.13), respectively. A comprehensive overview of the RNG method can be found in the study of Yokhot and Orszag [76].

$$\frac{\partial}{\partial x_i} (\rho k \bar{u}_i) = \frac{\partial}{\partial x_j} \left[\alpha_k \mu_{eff} \frac{\partial k}{\partial x_j} \right] + G_k - \rho \varepsilon - Y_M \quad (3.12)$$

$$\frac{\partial}{\partial x_i} (\rho \varepsilon \bar{u}_i) = \frac{\partial}{\partial x_j} \left[\alpha_\varepsilon \mu_{eff} \frac{\partial \varepsilon}{\partial x_j} \right] + \left(G_k C_{1\varepsilon} \frac{\varepsilon}{k} \right) - \rho C_{2\varepsilon} \frac{\varepsilon^2}{k} - R_\varepsilon \quad (3.13)$$

where G_k and Y_M are defined as the same for the standard k- ε model, which have been shown in Equations (3.9) and (3.10).

In order to determine the effective viscosity (μ_{eff}), the following differential equation has to be solved based on the scale elimination method as stated in the RNG theory.

$$d\left(\frac{\rho^2 k}{\sqrt{\varepsilon\mu}}\right) = 1.72 \frac{\hat{v}}{\sqrt{\hat{v}^3 - 1 + C_v}} d\hat{v} \quad (3.14)$$

where $\hat{v} = \mu_{eff}/\mu$ and $C_v \approx 100$. It is believed that for the RNG k- ε model Equation (3.14) provides better results for the near-wall flows. Note that the turbulent viscosity (μ_t) in the high Reynolds number regions is determined according to Equation (3.11) with $C_\mu = 0.0845$, which is quite close to the C_μ value specified for the standard k- ε model (i.e., $C_\mu = 0.09$).

In addition, α_k and α_ε terms in the k and ε transport equations are the inverse effective Prandtl numbers, wherein $\alpha_k = \alpha_\varepsilon \approx 1.393$.

Furthermore, the additional term of R_ε in Equation (3.13) is associated with the mean strain and turbulence quantities which is defined as

$$R_\varepsilon = \frac{C_\mu \rho \eta^3 (1 - \eta/\eta_0) \varepsilon^2}{1 + \beta \eta^3} \frac{1}{k} \quad (3.15)$$

where

$$\eta_0 = 4.38, \quad \beta = 0.012, \quad S = \sqrt{2S_{ij}S_{ij}}, \quad S_{ij} = \frac{1}{2}\left(\frac{\partial \bar{u}_j}{\partial x_i} + \frac{\partial \bar{u}_i}{\partial x_j}\right)$$

where S_{ij} is the mean strain rate tensor.

By substituting R_ε in Equation (3.13) and rearranging the equation, the transport equation for ε can be rewritten as

$$\frac{\partial}{\partial x_i}(\rho \varepsilon \bar{u}_i) = \frac{\partial}{\partial x_j} \left[\alpha_\varepsilon \mu_{eff} \frac{\partial \varepsilon}{\partial x_j} \right] + \left(G_k C_{1\varepsilon} \frac{\varepsilon}{k} \right) - C_{2\varepsilon}^* \rho \frac{\varepsilon^2}{k} \quad (3.16)$$

where

$$C_{2\varepsilon}^* = C_{2\varepsilon} + \frac{C_\mu \eta^3 (1 - \eta/\eta_0)}{1 + \beta \eta^3}, \quad C_{1\varepsilon} = 1.42, \quad C_{2\varepsilon} = 1.68 \quad (3.17)$$

It is reported that a lower turbulent viscosity is predicted for the RNG k- ε model in rapidly-strained flows compared to the standard k- ε model [72].

Note that the definition of the effective thermal conductivity in the energy equation (Equation (3.3)) for the RNG k- ε model is slightly different than that which has been defined in Equation (3.4). The effective thermal conductivity used in the RNG k- ε model is

$$k_{eff} = \alpha c_p \mu_{eff} \quad (3.18)$$

where $\alpha \approx 1.393$ in the fully turbulent region of the flow.

3.4. REALIZABLE $k - \varepsilon$ MODEL

The realizable k- ε model of Shih et al. [77] includes some developments and differs from the standard k- ε where a new formulation for the turbulent viscosity is proposed with different derivation for the ε transport equation. The realizable term indicates that certain mathematical constraints are satisfied for the Reynolds stresses. It is also reported in the literature that the realizable k- ε model could provide better predictions of the flow field for the flows including rotation, separation and recirculation [72].

The transport equation for the turbulent kinetic energy (k) is the same as that for the standard k- ε model, as expressed in Equation (3.7). The transport equation for the dissipation rate (ε) is defined as

$$\frac{\partial}{\partial x_i} (\rho \varepsilon \bar{u}_i) = \frac{\partial}{\partial x_j} \left[\left(\mu + \frac{\mu_t}{\sigma_\varepsilon} \right) \frac{\partial \varepsilon}{\partial x_j} \right] + \rho C_1 S_\varepsilon - \rho C_2 \frac{\varepsilon^2}{k + \sqrt{\nu \varepsilon}} \quad (3.19)$$

where

$$C_1 = \max \left[0.43, \frac{\eta}{\eta + 5} \right], \quad \eta = S \frac{k}{\varepsilon}, \quad S = \sqrt{2S_{ij}S_{ij}}, \quad S_{ij} = \frac{1}{2} \left(\frac{\partial \bar{u}_j}{\partial x_i} + \frac{\partial \bar{u}_i}{\partial x_j} \right) \quad (3.20)$$

The turbulent viscosity is modeled as expressed in Equation (3.11). However, unlike the other k- ε models (standard and RNG), the C_μ as presented in the turbulent viscosity is not

considered as a constant value in the realizable k- ε model. Wherein the C_μ can be calculated through the following equation

$$C_\mu = \frac{1}{A_0 + A_s \frac{kU^*}{\varepsilon}} \quad (3.21)$$

where

$$U^* \equiv \sqrt{S_{ij}S_{ij} + \tilde{\Omega}_{ij}\tilde{\Omega}_{ij}} \quad (3.22)$$

$$\begin{cases} \tilde{\Omega}_{ij} = \Omega_{ij} - 2\varepsilon_{ijk}\omega_k \\ \Omega_{ij} = \bar{\Omega}_{ij} - \varepsilon_{ijk}\omega_k \end{cases} \quad (3.23)$$

where $\bar{\Omega}_{ij}$ denotes the mean rate-of-rotation tensor viewed in a rotating reference frame with the angular velocity ω_k . The constants in Equation (3.21) are as follows

$$A_0 = 4.04, \quad A_s = \sqrt{6}\cos\phi$$

where: $\phi = \frac{1}{3}\cos^{-1}(\sqrt{6}W)$, $W = \frac{S_{ij}S_{jk}S_{ki}}{\sqrt{S_{ij}S_{ij}}}$

The default constants for the realizable k- ε model are provided as

$$C_{1\varepsilon} = 1.44, \quad C_2 = 1.9, \quad \sigma_k = 1.0, \quad \sigma_\varepsilon = 1.2$$

It is worth mentioning here that the production of k is not included in the production term (i.e. ρC_{1S_ε}) for the transport equation for ε (Equation (3.19)). To clarify, the same G_k as other k- ε models does not exist here. It is reported in the literature that the spectral energy transfer can be represented better by the present form of the production term for ε transport equation. Furthermore, no singularity can occur in the denominator of the destruction term (the last term

on the right-hand side of Equation (3.19)), even if $k \rightarrow 0$. This prevents the singularity that could happen in other variants of the k- ϵ model.

3.5. REYNOLDS-STRESS MODEL

In Reynolds-stress model (RSM), a transport equation is proposed to model the Reynolds stress tensor ($-\rho\overline{u'_i u'_j}$). The Reynolds stress tensor was assumed to be an isotropic tensor in the Boussinesq hypothesis. However, the anisotropic nature of the Reynolds stress tensor has been taken into account in the RSM model which is more realistic for turbulent flows. Therefore, seven transport equations, one transport equation for ϵ and six transport equations for the Reynolds-stress tensor must be solved for a three-dimensional flow to close the RANS equations. It is expected from the RSM model to increase the accuracy of the predicted results for the complex flows, since the effect of streamline curvature, swirl, rotation and rapid changes in strain rate have been taken into account in this model. However, it has to be noticed that several terms have to be modeled in the transport equation of RSM model; hence, some assumptions are needed for each term to close the equation [72]. This might affect the expected accuracy of the predicted results with the RSM model.

The transport of the Reynolds stresses can be expressed as the following transport equation

$$\begin{aligned}
\underbrace{\frac{\partial}{\partial x_k} (\rho u_k \overline{u'_i u'_j})}_{C_{ij} \equiv \text{Convection}} &= - \underbrace{\frac{\partial}{\partial x_k} \left[\rho \overline{u'_i u'_j u'_k} + p (\delta_{kj} u'_i + \delta_{ik} u'_j) \right]}_{D_{T,ij} \equiv \text{Turbulent Diffusion}} \\
+ \underbrace{\frac{\partial}{\partial x_k} \left[\mu \frac{\partial}{\partial x_k} (\overline{u'_i u'_j}) \right]}_{D_{L,ij} \equiv \text{Molecular Diffusion}} &- \underbrace{\rho \left(\overline{u'_i u'_k} \frac{\partial u_j}{\partial x_k} + \overline{u'_j u'_k} \frac{\partial u_i}{\partial x_k} \right)}_{P_{ij} \equiv \text{Stress Production}} \\
&+ \underbrace{p \left(\frac{\partial u'_i}{\partial x_j} + \frac{\partial u'_j}{\partial x_i} \right)}_{\phi_{ij} \equiv \text{Pressure-Strain}} \\
- \underbrace{2\mu \frac{\partial u'_i}{\partial x_k} \frac{\partial u'_j}{\partial x_k}}_{\epsilon_{ij} \equiv \text{Dissipation}} &- \underbrace{2\rho \Omega_k (\overline{u'_j u'_m} \epsilon_{ikm} + \overline{u'_i u'_m} \epsilon_{jkm})}_{F_{ij} \equiv \text{Production by System Rotation}} \tag{3.24}
\end{aligned}$$

where there is no need to model the following terms C_{ij} , $D_{L,ij}$, P_{ij} and F_{ij} . However, $D_{T,ij}$, ϕ_{ij} and ε_{ij} have to be modeled in order to close the equations. As mentioned before, some assumptions are required for modelling the mentioned terms.

The turbulent diffusion term ($D_{T,ij}$) can be modeled according to the generalized gradient diffusion model which is proposed by Daly and Harlow [78]. However, it can cause numerical instabilities in the ANSYS FLUENT software. Therefore, a simplified version of the generalized gradient diffusion model is employed, as shown in Equation (3.25) based on a scalar turbulent diffusivity of Lien and Leschziner [79].

$$D_{T,ij} = \frac{\partial}{\partial x_k} \left(\frac{\mu_t}{\sigma_k} \frac{\partial \overline{u'_i u'_j}}{\partial x_l} \right) \quad (3.25)$$

where $\sigma_k = 0.82$ and the turbulent viscosity can be computed from Equation (3.11) with $C_\mu = 0.09$.

In the present study, the linear pressure-strain model is implemented to model the pressure-strain term (ϕ_{ij}) in Equation (3.24). Wherein this term is decomposed into three terms as follows

$$\phi_{ij} = \underbrace{\phi_{ij,1}}_{\text{Slow Pressure-Strain}} + \underbrace{\phi_{ij,2}}_{\text{Rapid Pressure-Strain}} + \underbrace{\phi_{ij,w}}_{\text{Wall-Reflection}} \quad (3.26)$$

The details of the modelling procedures for each term in the above equation can be found in [72].

The dissipation tensor in Equation (3.11) can be modeled as follows

$$\varepsilon_{ij} = \frac{2}{3} \delta_{ij} (\rho \varepsilon + Y_M) \quad (3.27)$$

where Y_M can be expressed as in Equation (3.10).

Note that the transport equation for the dissipation rate in the RSM model is similar to that employed in the standard k- ε model, which can be defined as

$$\frac{\partial}{\partial x_i}(\rho \varepsilon \bar{u}_i) = \frac{\partial}{\partial x_j} \left[\left(\mu + \frac{\mu_t}{\sigma_\varepsilon} \right) \frac{\partial \varepsilon}{\partial x_j} \right] + \left(P_{ii} C_{1\varepsilon} \frac{\varepsilon}{2k} \right) - \rho C_{2\varepsilon} \frac{\varepsilon^2}{k} \quad (3.28)$$

where

$$C_{1\varepsilon} = 1.44, \quad C_{2\varepsilon} = 1.92, \quad \sigma_\varepsilon = 1.0$$

It is well-known that the aforementioned turbulence models are mainly valid for turbulent core flow which is far from the wall region. To solve the flow field in the near wall region, various approaches exist in the literature such as standard wall function, scalable wall function and enhanced wall treatment. A comprehensive detailing regarding various near wall approaches can be found in [72].

4. CIRCULAR EXIT SHAPED HOLE WITH DISCRETE SISTER HOLES' INFLUENCE

In traditional film cooling configuration, coolant air is injected through a circular pipe cross-sectional area with an inclined angle $0 < \alpha < 90$ which results in an elliptical exit shaped hole (EESH) at the plate's surface. Conversely, the motivation of the present chapter is based on injecting the coolant through an elliptical pipe which leads to a circular exit shaped hole (CESH). The film cooling effectiveness and the associated flow structure for both cases of circular and elliptical exit shaped holes are numerically investigated at four blowing ratios of 0.25, 0.5, 1 and 1.5. Moreover, the influence of the discrete sister holes on flow structure and film cooling effectiveness is studied.

4.1. PROBLEM STATEMENT

The simulation of the elliptical exit shaped hole is carried out based on the experimental setup of Sinha et al. [8]. As shown in Figure 4.1(a), the computational domain is extended for 19D and 30D distances from the leading edge (LE) and trailing edge (TE) of the primary (main) injection hole, respectively. The primary injection hole is highlighted in blue. Moreover, according to the pitch-to-diameter ratio of 3, the domain is extended 3D in the lateral direction. The primary hole has a diameter of $D = 12.7$ mm and is injected at 35° to the crossflow with a length-to-diameter ratio of 1.75. Using a plenum has an important positive effect on computational simulation; therefore, a plenum with dimensions of $8D \times 4D \times 3D$ is considered before injecting the coolant to the crossflow based on the numerical simulation of Walters and Leylek [21], as depicted in Figure 4.1(b).

The present test case is the short-hole film cooling ($L/D = 1.75$). As mentioned before, Ely and Jubran [62] reported that the up/downstream combination of the discrete sister holes provides higher film cooling performance compared to other combinations of the discrete sister holes (e.g., left/right, downstream or upstream sister holes). Accordingly, the up/downstream combination of sister holes is applied in the present simulation. Four active discrete sister holes

(up/downstream), which are highlighted in red, with the diameter of $0.5D$ are placed at $x/D = \pm 0.75$ and $z/D = \pm 0.75$ with respect to the center of the exit of the primary hole.

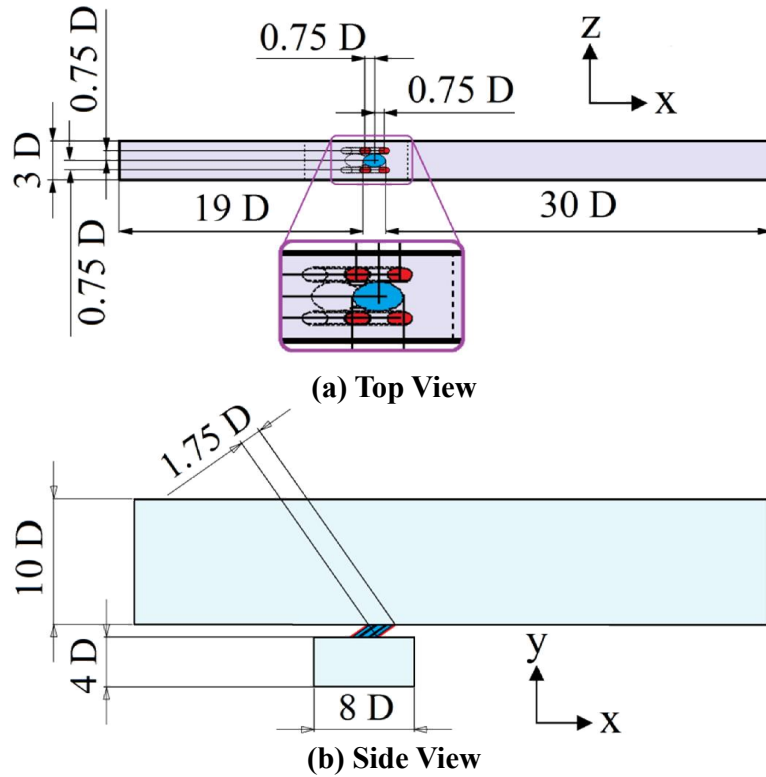


Figure 4.1: Geometry of EESH with up/downstream discrete sister holes

The semi-minor axis (a) and semi-major axis (b) of the ellipse for the elliptical exit shaped hole at the plate's surface can be easily found, wherein $a = D/2$ and $b = a/\sin(35^\circ)$. The ratio of the semi-major axis and the semi-minor axis of the EESH is defined as $e = b/a$. To keep the consistency between the elliptical and the circular exit shaped holes, both cases must have the same coolant pipe cross-sectional area (A_{cs}), therefore A_{cs} for the CESH geometry can be easily calculated, as presented in Equation (4.1):

$$A_{cs} = \frac{\pi D^2}{4} \quad (4.1)$$

all 4 sister holes are active, twice the amount of coolant is required than in the case of a single hole at the same blowing ratio. The inlet coolant velocity can be simply calculated using the continuity equation. The plenum inlet velocity for both single and sister hole cases at different blowing ratios can be found in Table 4.1.

Table 4.1: Plenum inlet velocity

Blowing Ratio (M)	Plenum inlet velocity [m/s]	
	Single Hole	Up/Downstream Discrete Sister Holes
0.25	0.136	0.273
0.5	0.273	0.545
1	0.545	1.091
1.5	0.818	1.636

The freestream turbulence intensity is set to 0.2% as stated in the experimental data of Sinha et al. [8]. According to the numerical simulation of Azzi and Lakehal [80], this value is considered as 2% at the plenum inlet. The viscosity ratios of $\mu_t/\mu = 30$ and 50 are specified at the plenum and freestream inlets, respectively.

It is worth mentioning that Sargison [81] pointed out that several dimensionless parameters in an experiment should be matched to engine conditions. A typical mainstream and coolant air temperatures in the engine condition are of the order of 1750 K and 900 K, respectively [81]. In an experimental setup lower order of the mainstream and cooling gas flow temperatures can be used. Accordingly, some dimensionless parameters in an experiment such as density ratio and blowing ratio, which are depending on temperature, have to be matched to the engine conditions.

4.2. COMPUTATIONAL OVERVIEW AND DOMAIN

For modeling of the flow field modeling, four Reynolds-Averaged Navier-Stokes (RANS) turbulence models, including the standard, realizable and RNG $k-\epsilon$ as well as the Reynolds-stress model are used. Moreover, different approaches to model the near-wall region are examined. Finally, the realizable $k-\epsilon$ model combined with the standard wall function is chosen for the rest of simulations, which will be discussed in the following section. ANSYS

FLUENT 14.0.0 is used for the numerical simulation. Note that the density of the grids in the near-wall region has been varied with respect to each wall function used to satisfy its recommended value of y^+ . For the enhanced wall treatment and standard wall function, y^+ is set to around unity and 30, respectively [72]. The purpose of the scalable wall function is to force the usage of the log-law combined with the standard wall function approach, where the computed value of y^+ is not allowed to fall below the limit of 11.23. The schematic view of the computational domain and applied boundary conditions are depicted in Figure 4.3.

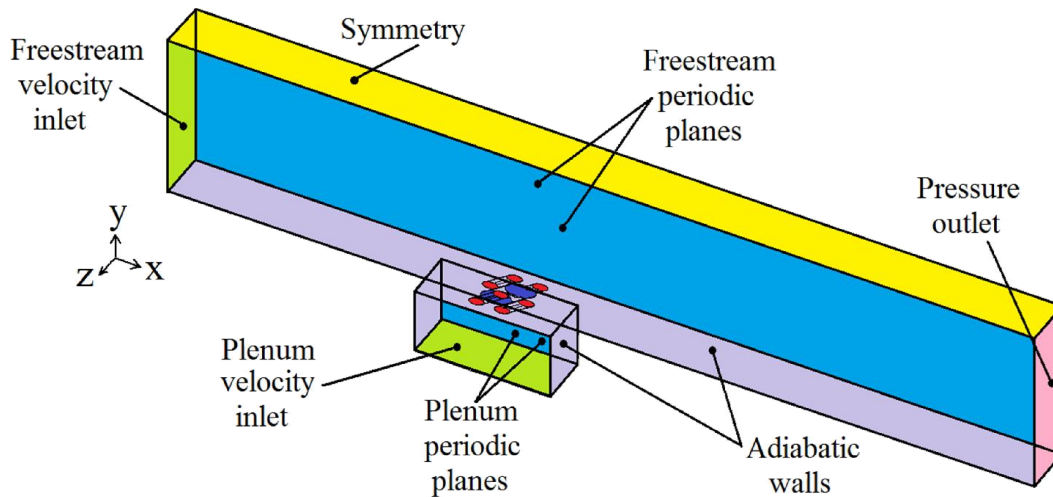


Figure 4.3: Schematic view of computational domain and boundary conditions

The second order upwind solution scheme is used to solve the momentum, energy and turbulence model equations. The SIMPLEC algorithm is employed to solve the pressure-velocity coupling. The flow is considered as incompressible ideal gas. The simulations are terminated when the normalized residuals reach 10^{-5} for all variables and 10^{-7} is considered for the energy equation.

ANSYS GAMBIT 2.4.6 is used to generate the geometry and required grid for the solver. Grid sizes of 0.77, 1.01, 1.48 and 1.96 million hexahedral cells were generated by increasing the number of nodes by a factor of 10% on each edge. The maximum stretch factor of 1.1 is applied as the limitation for each edge. Finally, the grid size of 1.48 million cells is established as the grid-independent solution for all simulations. The side view of computational grids for the EESH with up/downstream sister holes can be found in Figure 4.4.

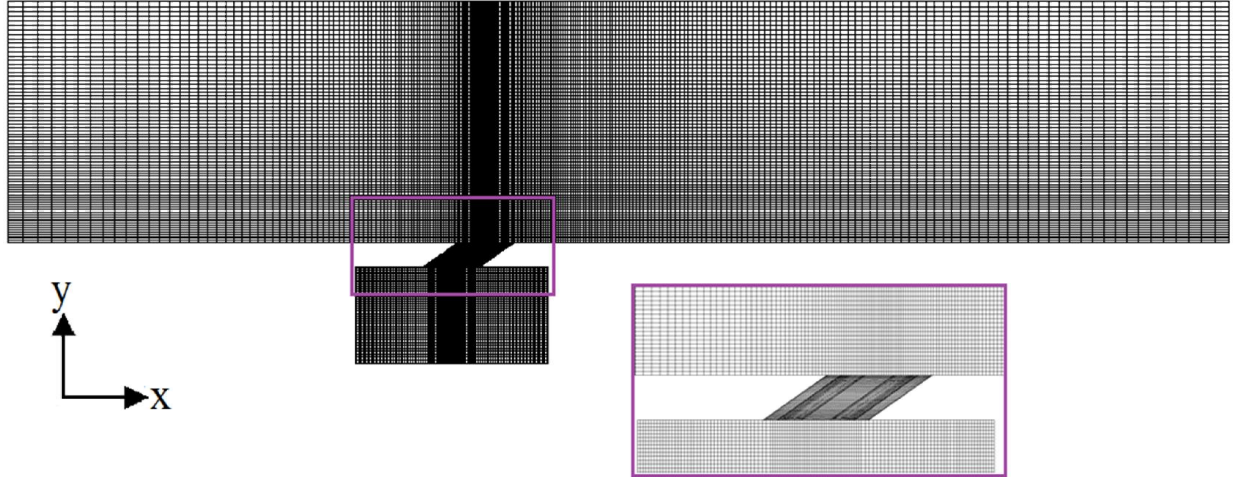


Figure 4.4: Side view of the computational grids (EESH with Up/Downstream sister holes)

The adiabatic film cooling effectiveness including the centerline and laterally averaged film cooling effectiveness results are calculated at the adiabatic wall surface (either plate or blade) based on Equations (4.3) and (4.4), respectively; trapezoidal numerical integration is used to find the laterally averaged film cooling effectiveness values.

$$\eta = \frac{T_{\infty} - T_{aw}}{T_{\infty} - T_c} \quad (4.3)$$

$$\bar{\eta} = \frac{1}{L} \int_0^L \eta dz \quad (4.4)$$

where L in Equation (4.4) is the length of the lateral distance between the periodic boundaries.

4.3. RESULTS

The obtained results for this chapter are broken into four subsections. First, the performance of four RANS-based turbulence models as well as different near-wall approaches is evaluated. Then, the adiabatic film cooling effectiveness results including the centerline and laterally averaged film cooling effectiveness for four blowing ratios are presented. Next, the associated flow structure with the aid of the velocity vectors and temperature contours are discussed. Finally, the effect of the exit hole shape on both EESH and CESH is investigated.

4.3.1. Turbulence Modeling

The comparison between the available experimental data of Sinha et al. [8] and predicted centerline film cooling effectiveness of EESH case for three different wall functions at the blowing ratios of 0.5 and 1 is shown in Figure 4.5. Moreover, the realizable $k-\epsilon$ model combined with the standard and scalable wall functions as well as the enhanced wall treatment (two-layer approach) are used to investigate the influence of near-wall modeling on the centerline film cooling effectiveness.

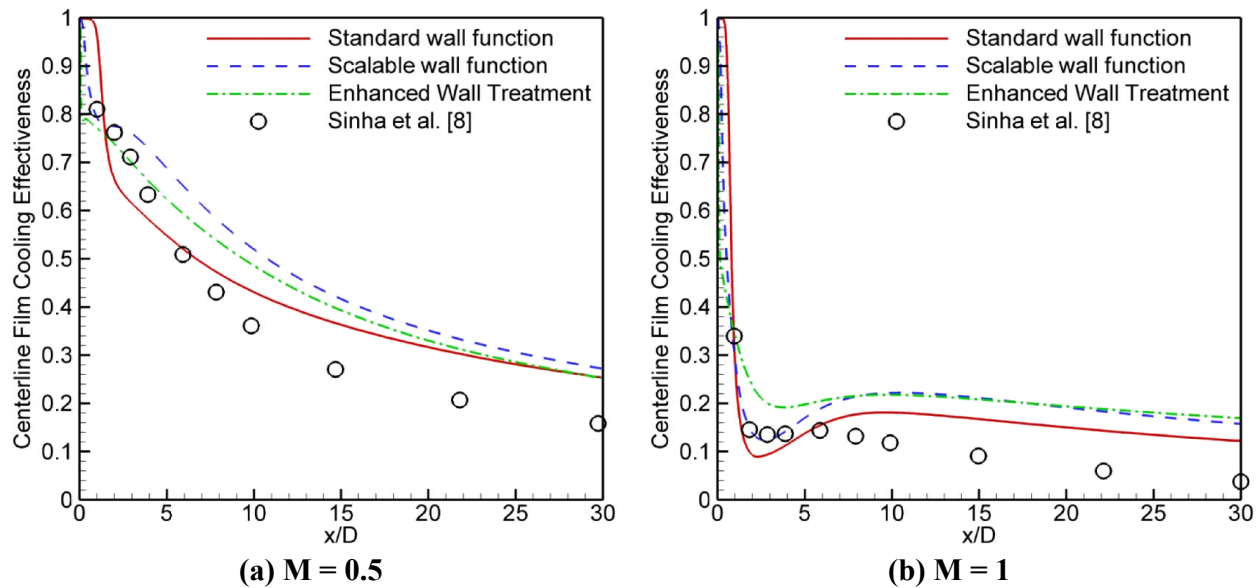


Figure 4.5: Performance of different near-wall approaches in terms of centerline film cooling effectiveness

For the low blowing ratio of $M = 0.5$ for the near-hole region ($x/D < 5$), predicted results with the enhanced wall treatment are in better agreement with the experimental data compared to other wall functions, as illustrated in Figure 4.5(a). It can be seen that the scalable wall function, except in the near-hole region, overpredicts the centerline film cooling effectiveness at both blowing ratios. Although the enhanced wall treatment, which is also known as the two-layer model, shows less overprediction than the scalable wall functions at low blowing ratio, its prediction for the near-hole region at the high blowing ratio is weaker than expected. On the other hand, the standard wall function is in better agreement with the experimental data. However, the standard wall function performed better compared with other wall approaches in the downstream region. As shown in Figure 4.5(b), the outperformance of the standard wall

function becomes more recognizable at $M = 1$, where it can capture the jet detachment in the near-hole region; its overprediction on centerline film cooling effectiveness is less than the other two near-wall approaches in the downstream region. Outperforming the standard wall function for the film cooling application has also been reported in the work of Zhang and Hassan [22].

The performance of four different turbulence models is evaluated for blowing ratios of 0.5 and 1, as illustrated in Figure 4.6(a and b), respectively.

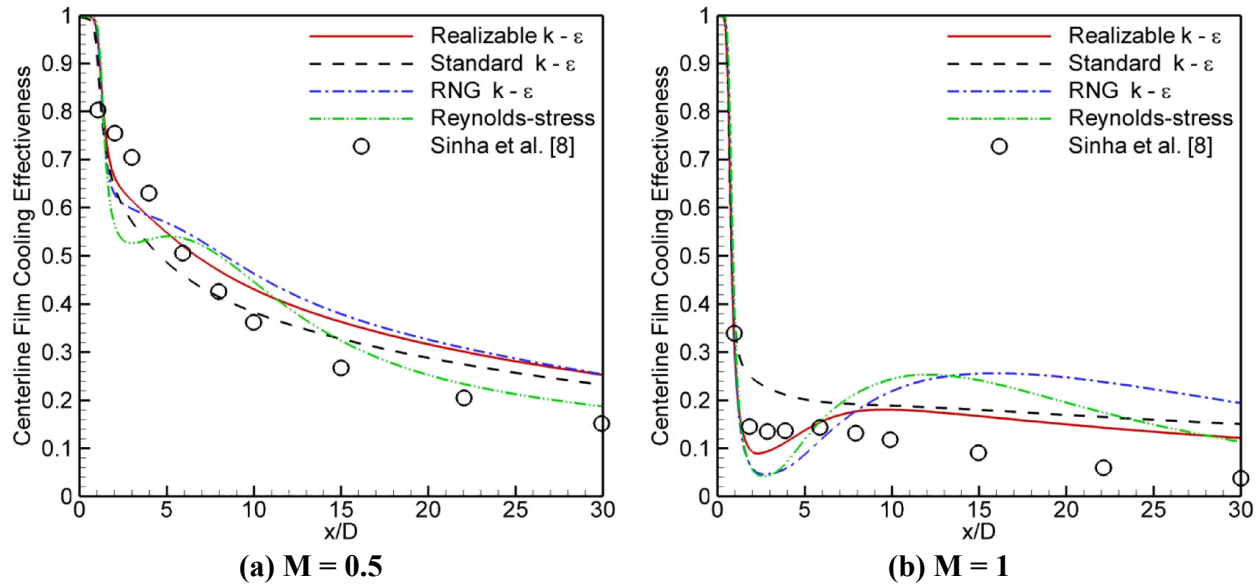


Figure 4.6: Performance of different RANS-based turbulence models in terms of centerline film cooling effectiveness

The standard, realizable and RNG version of $k-\epsilon$ model as well as the Reynolds-stress model are applied to model the flow field. Although the standard $k-\epsilon$ model has a reasonable trend for centerline film cooling effectiveness at the low blowing ratio of 0.5, it is not able to capture the jet lift-off effect in the near hole region of $x/D < 5$ at high blowing ratios, since the flow field in the near hole region is highly swirling. On the other hand, some turbulence models such as the RNG $k-\epsilon$, realizable $k-\epsilon$ and Reynolds-stress models are performing better in this region. In addition, the RNG $k-\epsilon$ models provides a similar trend to the realizable $k-\epsilon$ model at $M = 0.5$, whereas its underprediction for $x/D < 8$ and overprediction for the far field region at the high blowing ratio is not acceptable. Again, the Reynolds-stress model gives under and overprediction of the centerline film cooling effectiveness, before and after $x/D = 6$, respectively; which will be magnified at high blowing ratios. However, post halfway in the downstream

region, RSM is in better agreement with the experimental data at the blowing ratio of 0.5. In general, the realizable $k-\epsilon$ model outperforms all other tested turbulence models, where the jet lift-off at high blowing ratio can be well captured, as depicted in Figure 4.6(b). The deviation of the predicted results with the RNG $k-\epsilon$ and RSM models from the experimental data is more than that with the realizable $k-\epsilon$ model in the downstream region ($x/D > 6$). Generally speaking, the realizable $k-\epsilon$ model is in reasonable agreement with experimental data and performed better, compared with other turbulence models; hence, the rest of calculations are carried out with this model combined with the standard wall function.

4.3.2. Film Cooling Effectiveness

The performance of the elliptical and circular exit shaped hole cases as well as the influence of the discrete sister holes on the centerline and laterally averaged film cooling effectiveness are presented in this section. The centerline and laterally averaged effectiveness at blowing ratios of 0.25, 0.5, 1 and 1.5 are shown in Figure 4.7 and Figure 4.8, respectively. Note that the blowing ratios of 0.25 and 0.5 are considered as the low blowing ratio cases and the high blowing ratio cases are based on $M = 1$ and 1.5.

It should be mentioned here that other combinations of sister holes namely upstream, downstream and left/right sister holes have also been studied. However, due to the outperformance of up/downstream sister holes for the present tested-configurations, only the results for up/downstream are discussed here. This is in-line with the numerical results reported by Ely and Jubran [62], for the short hole film cooling geometry where the up/downstream sister holes gives better cooling performance.

Using the circular exit shaped hole geometry at the low blowing ratio of 0.25 a slight improvement for the centerline film cooling effectiveness is seen, compared with the single EESH case. By applying the sister holes to both shaped holes, the maximum increase in centerline film cooling effectiveness that can be achieved is nearly 37% and 24% for the EESH and CESH cases, respectively. The performance of the sister holes becomes more notable at the low blowing ratio of 0.5 for both cases, where the highest centerline film cooling effectiveness is achieved for the up/downstream CESH scheme.

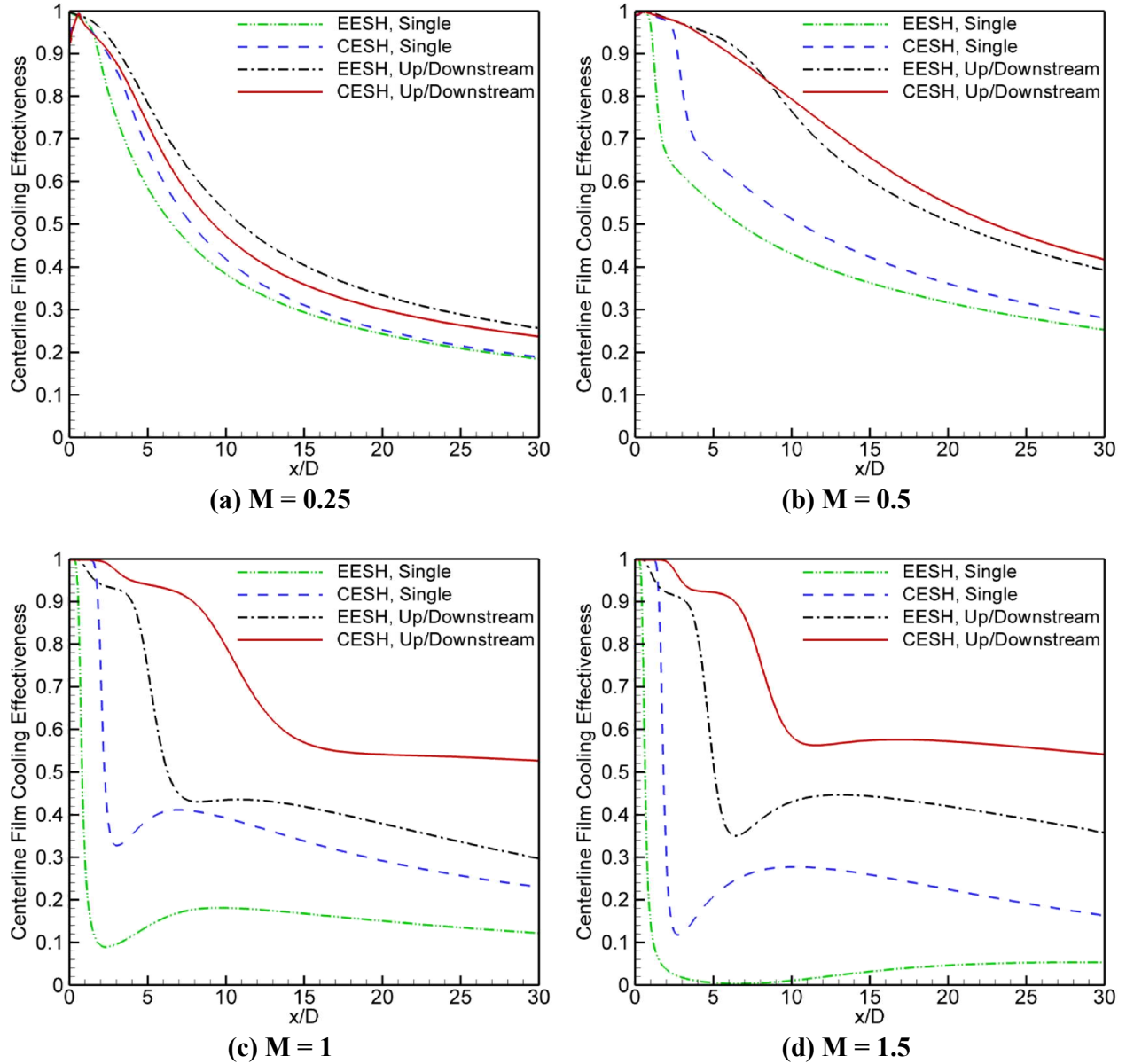


Figure 4.7: Centerline film cooling effectiveness

It can be seen that both the centerline and laterally averaged film cooling effectiveness values gradually decrease as x/D increases at low blowing ratios, even in the presence of sister holes. However, at high blowing ratios of 1 and 1.5, there is a plateau at the centerline effectiveness after $x/D = 15$ and 10, respectively. It dictates that the mixing rate of the coolant with the hot mainstream flow is diminished after the downstream region.

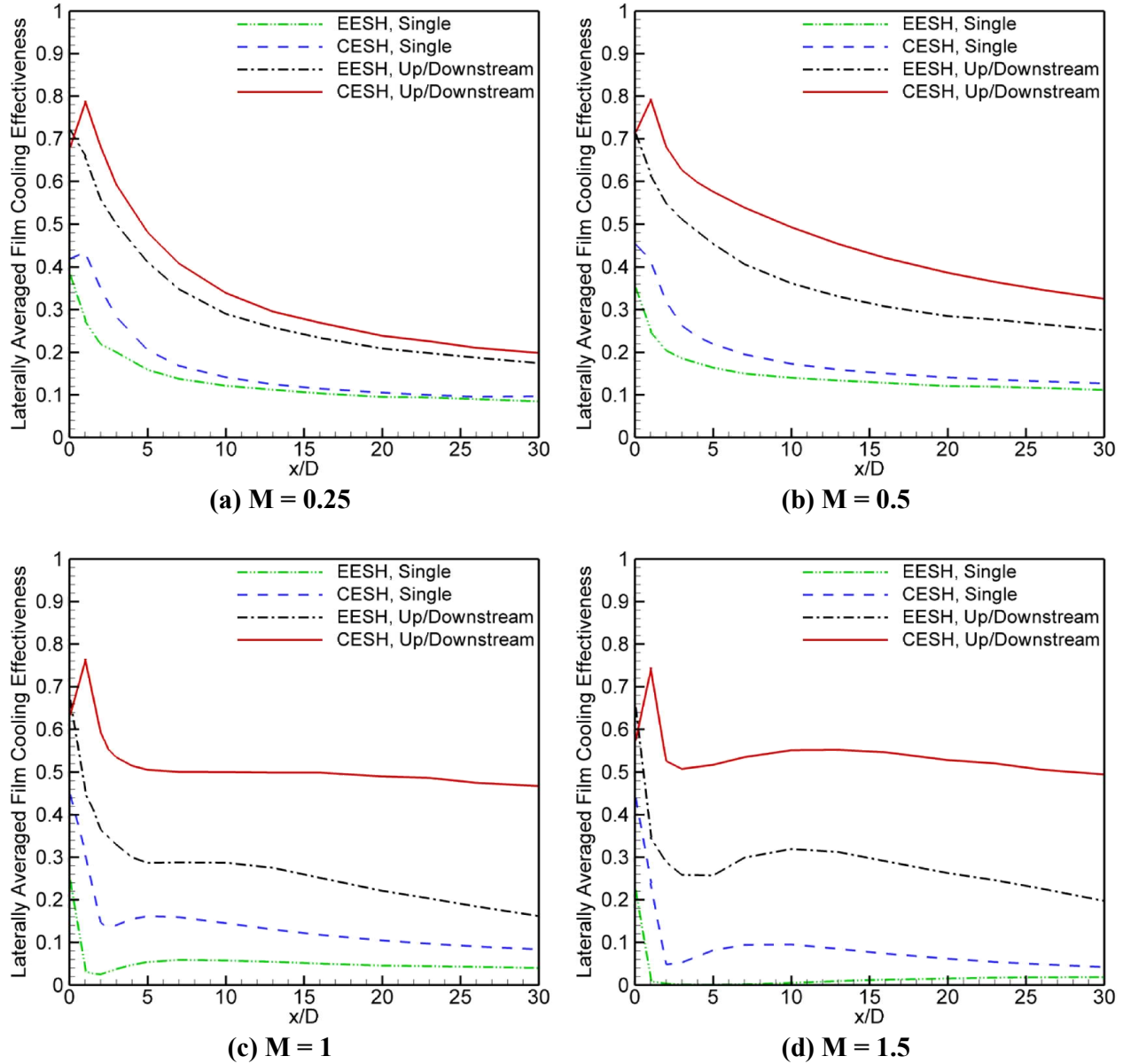


Figure 4.8: Laterally averaged film cooling effectiveness

In addition, the circular exit shaped hole provides a considerable enhancement in the centerline film cooling effectiveness at high blowing ratios, where the elliptical exit shaped hole gives poor results. Interestingly, the CESH case offers the optimal film cooling effectiveness in the near hole region of $x/D < 2$. As depicted in Figure 4.7(a and b), applying the discrete sister holes at this blowing ratio on both schemes indicates a notable increase in film cooling effectiveness.

In general, the trends of the results for the laterally averaged film cooling effectiveness are similar to those for the centerline film cooling effectiveness. However, the CESH case combined with the up/downstream sister holes is more successful than other configurations, as shown in Figure 4.8.

It is worth to point out that the film cooling effectiveness plateau also happens here for the laterally averaged film cooling effectiveness at $x/D > 5$ and provides a constant effectiveness value of around 0.5. This can be attributed to the reduction in mixing of coolant air with the hot freestream gas and hence a decrease in vortex strength, which will be the main focus of the subsequent section.

In summary, applying discrete sister holes to both shaped holes considerably increases the centerline and laterally averaged film cooling effectiveness, where the highest effectiveness is achieved by the combination of circular exit shaped hole with up/downstream discrete sister holes.

4.3.3. Flow Structure

Many researchers have reported different vortex structures; particularly the counter-rotating vortex pairs have a predominant effect on film cooling performance. Herein the flow structure using the temperature contours along with the velocity vectors is evaluated at blowing ratios of 0.5 and 1. As shown in the effectiveness section, the trend of the results for the low blowing ratio cases (i.e., $M = 0.25$ and 0.5) and for the high blowing ratio cases (i.e., $M = 1$ and 1.5) were almost similar; therefore, the blowing ratios of 0.5 and 1 are chosen for this section to study the associated flow structure which represent the low and high blowing ratios, respectively.

Figure 4.9 and Figure 4.10 display the flow structure for the blowing ratio of 0.5 at $x/D = 1$ and 5, respectively; both the single and up/downstream discrete sister holes cases for the elliptical and circular exit shaped holes are shown. Results for the blowing ratio of 1 are presented in Figure 4.11 and Figure 4.12, correspondingly.

As displayed in Figure 4.9 and Figure 4.10, comparison between single elliptical and circular exit shaped hole cases does not show any notable difference at the low blowing ratio of 0.5. However, the coolant jet from the CESH spreads more in the lateral direction rather than the vertical direction compared with the EESH, due to the expansion of the hole geometry in the lateral direction (i.e., $0.91D$). In terms of the flow structure, counter rotating vortex pairs are

deeply affected by the vortices generated from the sister holes, which are rotating in the opposite direction. Hence, the warmer flow penetrates the cold jet and more attached coolant will be provided in the spanwise direction.

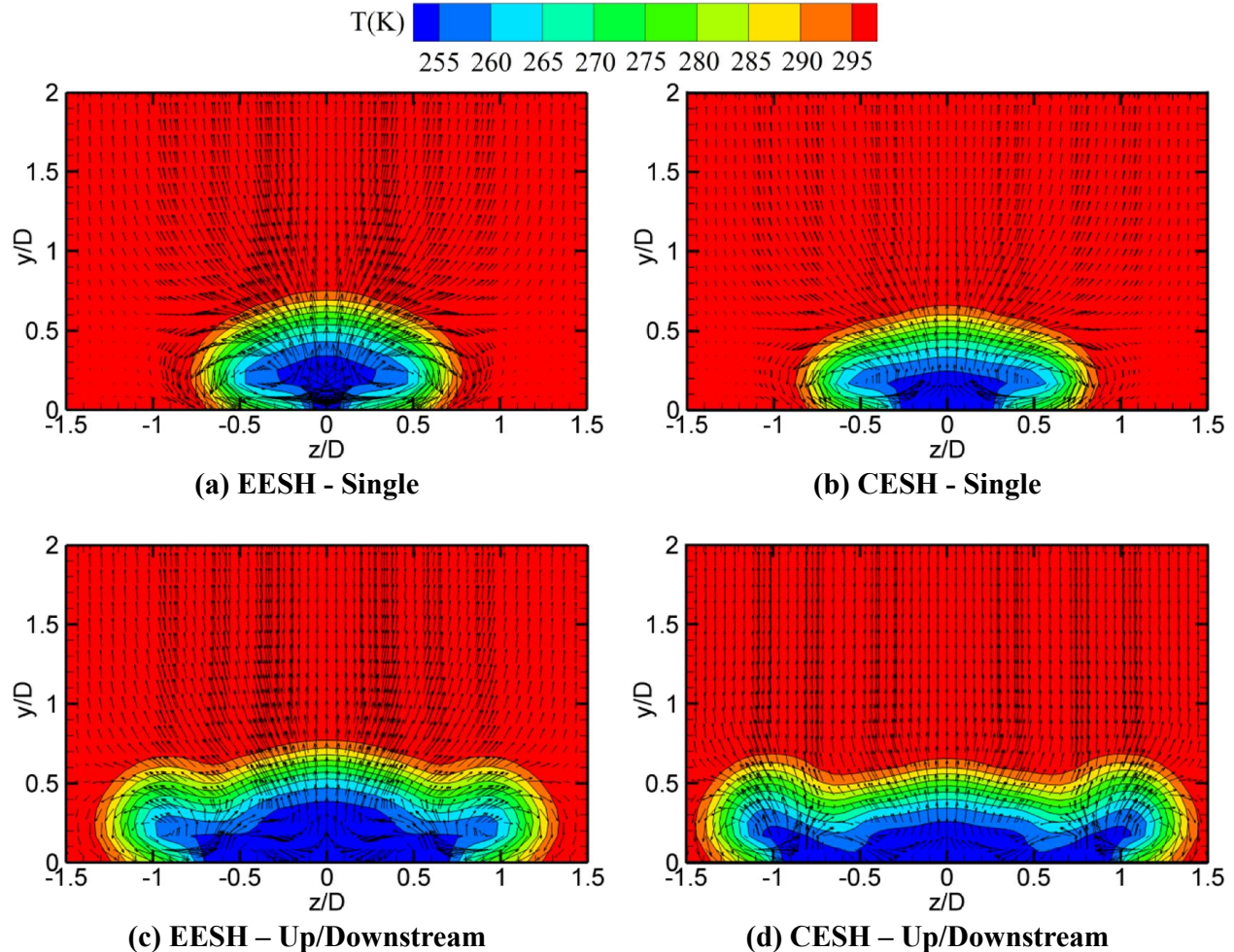


Figure 4.9: Temperature contours and velocity vectors for blowing ratio of $M = 0.5$ at $x/D = 1$

It is interesting to note that the resultant vortex pairs for up/downstream case are pushed away from the centerline surface and become weaker compared with the vortices of the single hole; therefore, it offers uniform spreading of coolant jets along the spanwise direction, which can be recognizable by the aid of temperature contours. As depicted in Figure 4.10, these effects will become more evident in the downstream region ($x/D = 5$), where the hot mainstream flow exists in $z/D = \pm 0.7$ close to the wall region for the single EESH, while for the sister holes case it is present at $z/D = \pm 1.3$. The circular exit shaped hole benefits more from the sister holes

compared with the traditional elliptical ones, where, in the vicinity of periodic planes and near the wall surface the hot mainstream flow does not exist, as can be seen in Figure 4.10(d).

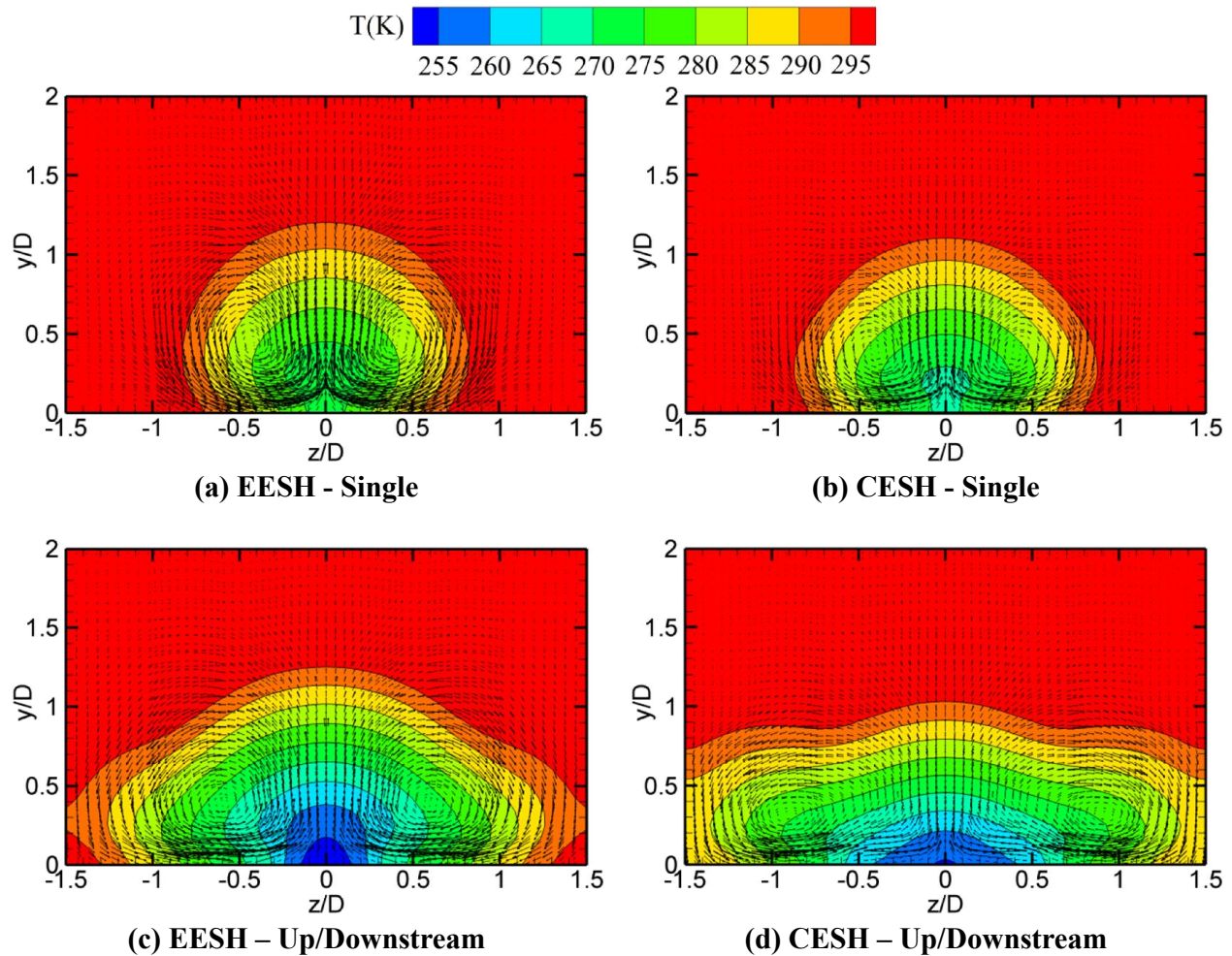


Figure 4.10: Temperature contours and velocity vectors for blowing ratio of $M = 0.5$ at $x/D = 5$

On the other hand, at the higher blowing ratio of 1, while the coolant jet becomes almost separated from the surface for the elliptical exit shaped hole case, the cold flow is still attached to surface at both x/D positions of 1 and 5. This can also be proved in Figure 4.7(c), where the centerline film cooling effectiveness for CESH demonstrates almost double effectiveness values compared to the EESH case. The jet lift-off for the CESH is lower than that for the EESH. It is true that the strength and the formation process of CRVP can be dependent on the injection hole configuration and the shape of the hole at the exit plane. This has also been observed by Haven and Kurosaka [24].

Moreover, as a result of vortex pairs, the jet lift-off effect will become considerable as the blowing ratio increases to the value of 1. As expected, the strength of the CRVP increases at higher blowing ratio and circulation of vortices attempts to push the hot mainstream flow underneath the cold jet. Consequently, undesired separation of the coolant from the surface will occur.

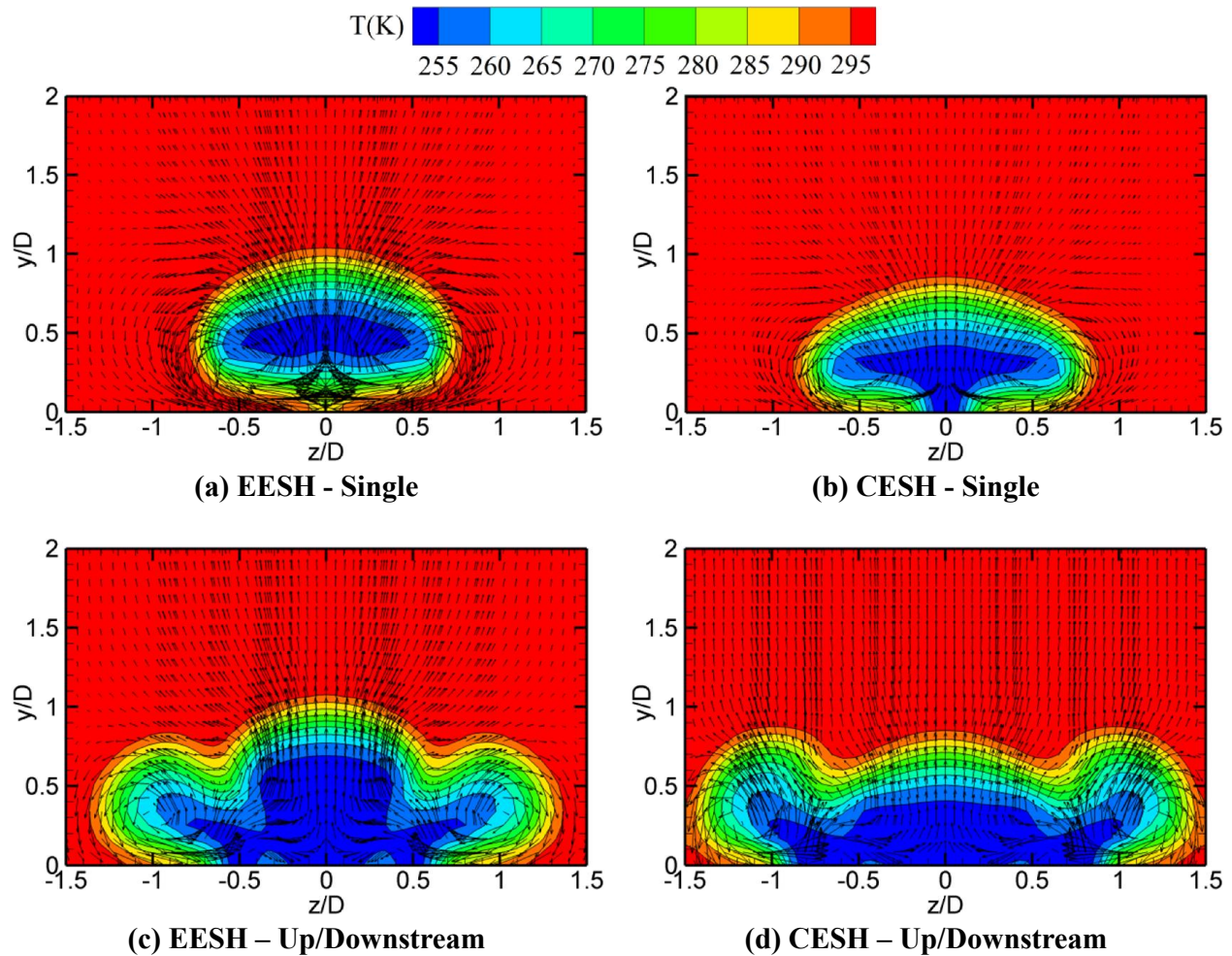


Figure 4.11: Temperature contours and velocity vectors for blowing ratio of $M = 1$ at $x/D = 1$

Using discrete sister holes for the EESH case at high blowing ratios does not act as efficiently as for the blowing ratio of 0.5. This is because sister holes' anti-vortices are not as powerful as the CRVP from the primary EESH and the jet lift-off effect still plays a dominant role. However, as mentioned before, the performance of CESH combined with sister holes at the higher blowing ratio of 1 was superior for centerline and laterally averaged film cooling effectiveness. At the near-hole region of $x/D = 1$, the jet lift-off dramatically decreased, even

more than the case of EESH with sister holes (see Figure 4.11(c and d)). As a result, coolant flow tends to adhere to the surface and gives a desired cooling condition.

Additionally, the position of vortex pairs is not only shifted towards the periodic planes but also moves closer to the wall surface; this makes them weak and they cannot rotate as fast as before. Remarkably, the weakness of vortex pairs in areas farther downstream of the coolant injection ($x/D = 5$) resists against the penetration of hot freestream to the coolant jet. Visibly, the core of the coolant jet is completely lifted up for the EESH hole case, while it remains attached to the surface and tends to spread in the spanwise direction for the up/downstream CESH configuration, as illustrated in Figure 4.12(c and d).

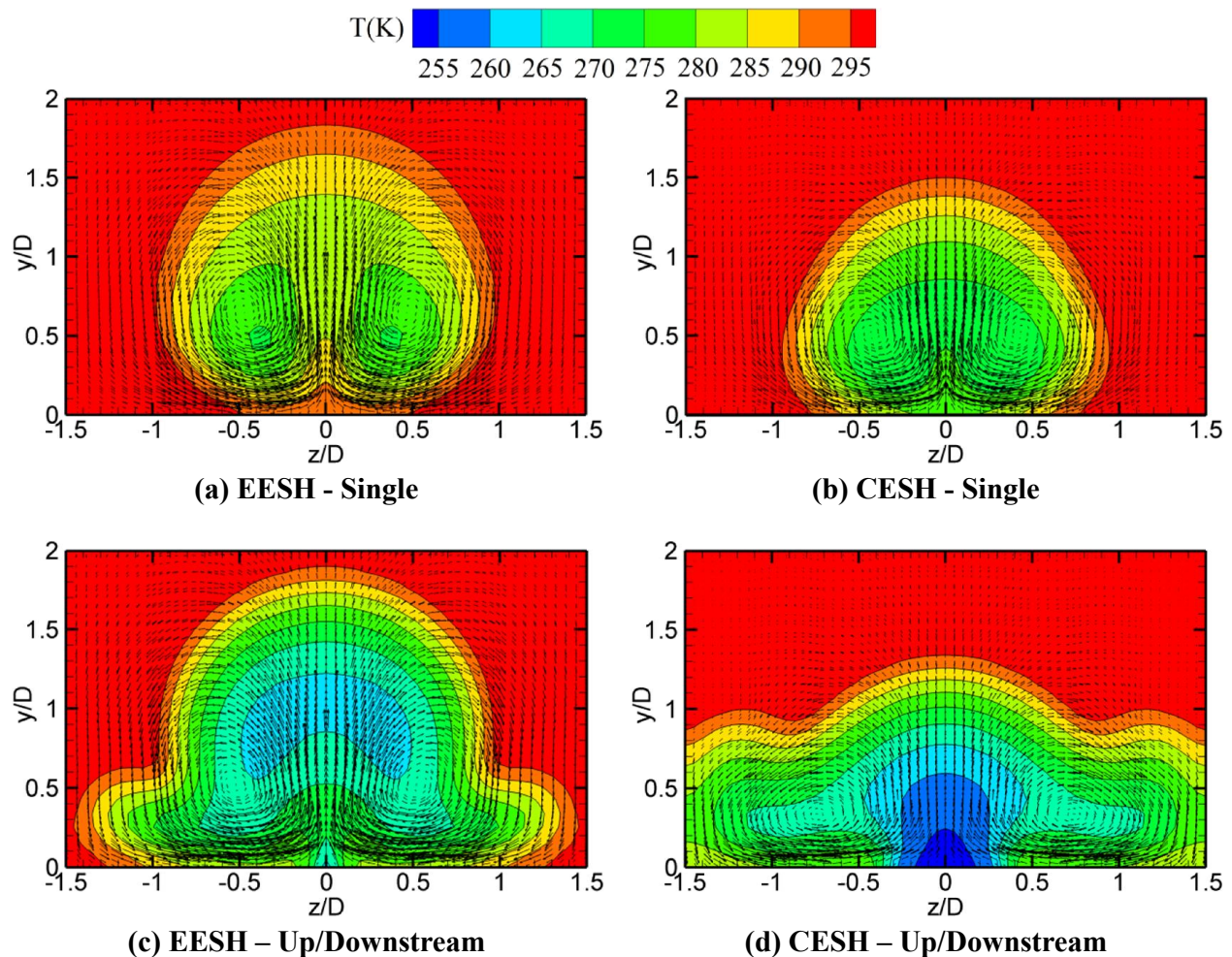


Figure 4.12: Temperature contours and velocity vectors for blowing ratio of $M = 1$ at $x/D = 5$

One reason to give better performance for the CESH with sister holes can be the lateral positioning of the sister holes, which were located at $0.91D$ from the centerline compared to that

of $0.75D$ for the EESH case. It means that the position of discrete sister holes can still be refined to achieve higher film cooling performance. Another reason is related to the decrease in the jet lift-off effect from the circular exit shaped hole, which will be discussed in the following section.

4.3.4. Effect of the Exit Hole Shape

The velocity magnitude contours in the jet exit plane are shown in Figure 4.13 for the blowing ratios of 0.5 and 1, respectively.

Walters and Leylek [21] pointed out that the distribution of the flow variables at the jet exit plane mainly depends on the blowing ratio, density ratio and geometry. In the present chapter, it depends on the blowing ratio and the hole geometry. As shown in Figure 4.13, the higher momentum region for the coolant flow is mainly positioned in the half region of the hole, which is close to the jet trailing edge (TE) for both the elliptical and circular exit shaped holes. It is worthy to point out the gradient of the flow variables for the circular exit shaped hole is lower than that for the elliptical ones, which is also valid for the blowing ratio of 1. This can lead to more uniform coolant flow at the jet exit plane. Note that the maximum velocity magnitude for the circular exit shaped hole has increased by about 0.07 m/s in the lateral edge of the hole when compared with the elliptical exit shaped hole for both $M = 0.5$ and 1. This region is close to where the discrete sister holes are located; and as mentioned in the previous section, the single and sister holes cases of the CESH geometry performed better than the EESH configuration, particularly at a high blowing ratio of 1. Considering that the blowing ratio is directly proportional to the coolant velocity, it can be concluded that the slight increase in velocity magnitude at the jet exit plane for the CESH geometry caused a notable increase in the performance of the sister holes, in comparison with the EESH case.

On the other hand, the flow variables are pushed toward the jet leading edge (LE) by increasing the blowing ratio, which can be seen in Figure 4.13(a and b). Note that the interaction of the coolant jet with the mainstream flow affects the distribution of the flow variables in the jet exit plane. As expected, this effect is more notable for the higher blowing ratios, compared with the low blowing ratio condition. Thus, the low momentum region shrinks and a horseshoe area forms for the high momentum region. It should be noted here that as a result of the jet and mainstream interaction, high and low pressure zones form upstream (LE) and downstream (TE) of the hole, respectively. Consequently, the momentum of the coolant flow increases downstream

of the exit hole, which is caused by the pressure gradient. However, the opposite outcome is achieved at the blowing ratio of 1. This can be attributed to the strong effect of the blowing ratio on the jet exit condition.

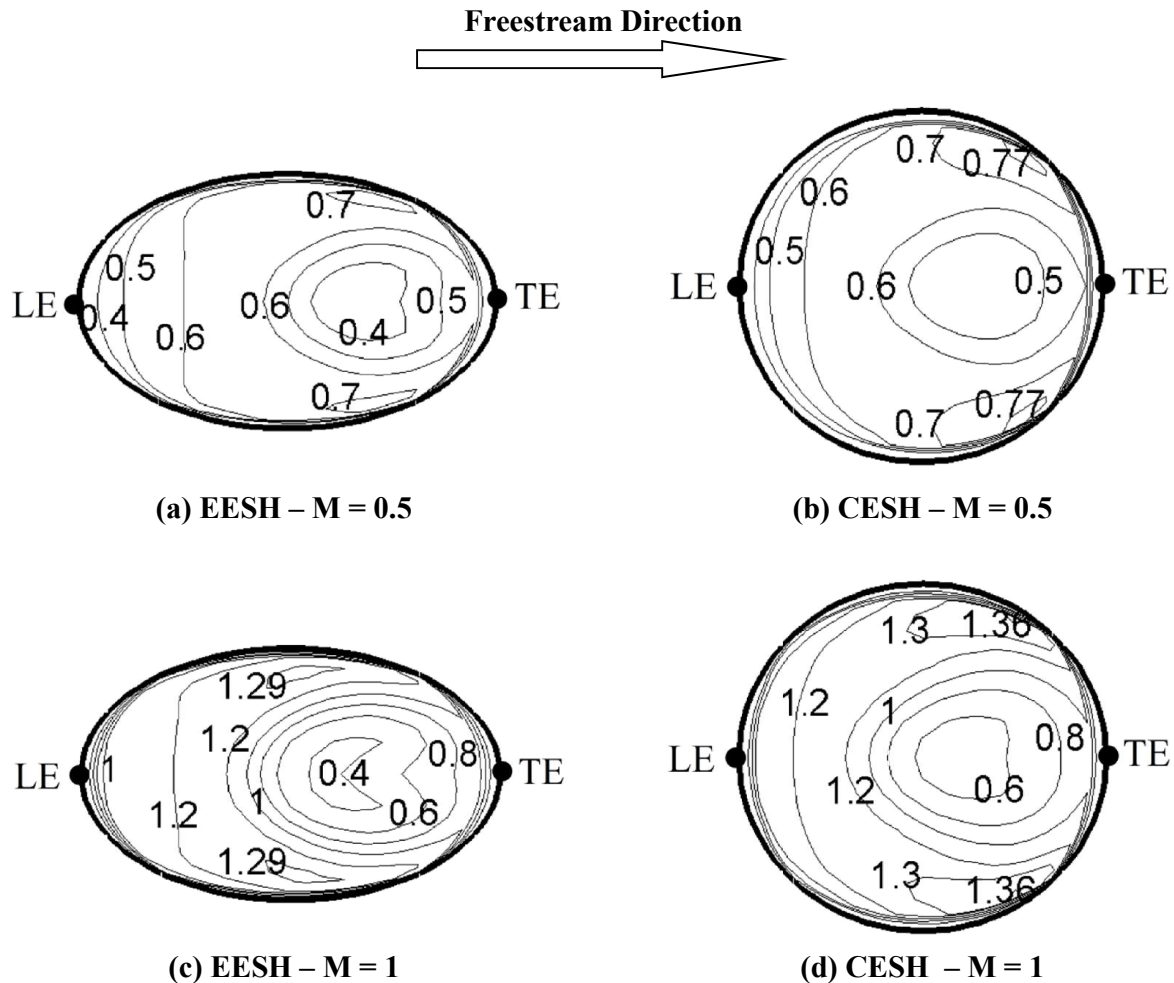


Figure 4.13: Velocity magnitude contours [m/s] in the jet exit plane for $M = 0.5$ and 1.5 (not drawn to scale)

4.4. CONCLUSIONS

The circular exit shaped hole configuration (CESH) provided a higher film cooling effectiveness at the high blowing ratios of 1 and 1.5, in comparison with the traditional elliptical exit shaped hole (EESH) geometry. Furthermore, outstanding film cooling effectiveness results were achieved by adding the discrete sister holes, where adiabatic effectiveness results reached a plateau. Note that altering the hole geometry did not have a major effect on the results at low blowing ratios.

The CFD analysis for the present film cooling simulation shows that the near-wall modeling plays an important role in the accuracy of the results, particularly at high blowing ratios.

Flow structure study demonstrated that the CRVP are responsible for the jet lift-off effect and the decrease in film cooling performance. These vortex pairs became weaker for the CESH scheme and consequently, provide more adhesion for the coolant flow to the surface than for the EESH. Furthermore, the repositioning of the sister holes for the CESH scheme shifted the vortices away from the centerline plane to assist the coolant air flow to spread in the spanwise direction.

Analysis of the jet exit condition confirmed that the blowing ratio and the exit shape hole as well as the hole geometry have a significant effect on flow variables on the jet exit plane.

5. MODIFICATION OF DISCRETE SISTER HOLES' LOCATION

In the previous chapter, the effect of sister holes on the proposed circular exit shaped hole (CESH) configuration has been investigated. The CESH geometry provided higher film cooling effectiveness as compared to the cylindrical hole. Wherein, by altering the location of the sister holes due to the design limitations for the CESH geometry, superior film cooling effectiveness is achieved as compared with the cylindrical hole with the sister holes. This is considered as the motivation for the present chapter.

A numerical parametric study on the effects of the discrete sister holes' location on film cooling performance is carried out in this chapter. The location of the up/downstream combination of the sister holes has been changed individually in the streamwise and spanwise directions. These include five new locations in each direction. Simulations are performed for low and high blowing ratios, where the low blowing ratios are represented by $M = 0.2$ and 0.5 , and the high blowing ratios by $M = 1$ and 1.5 . The obtained results are also compared with a single cylindrical hole.

5.1. PROBLEM STATEMENT

Some of the geometric parameters and/or boundary conditions in each chapter might be similar to the previous chapter/s. However, a quick review on the important aspects of the simulations for each individual chapter is presented in order to keep the unity of each chapter and to prevent any confusion.

The cylindrical hole case is simulated according to the experimental setup of Sinha et al. [8]. As shown in Figure 5.1(a), the computational domain is extended to $19D$ and $30D$ from the leading edge (LE) and trailing edge (TE) of the primary injection hole, respectively. To consider a film hole pitch-to-diameter ratio of 3, the geometry is expanded $3D$ in the lateral (spanwise) direction. The primary hole, which is highlighted in blue, has a diameter of $D = 12.7$ mm and is inclined at 35° to the crossflow with a length-to-diameter ratio of $L/D = 1.75$.

A slight modification is applied to simulate the single cylindrical case of Sinha et al. [8]. As mentioned before, Zhang and Hassan [22] carried out a detailed study on the numerical simulation of the experimental setup of Sinha et al. [8]. Unlike many previous simulations presented in the literature for the experimental setup of Sinha et al. [8] with the mainstream channel height of 10D, they reported that the height of the mainstream channel should be extended to 20D in the y direction in order to be far enough to apply a symmetry boundary condition. This extended domain can slightly increase the accuracy of the predicted film cooling effectiveness. Accordingly, in the present study the mainstream block is extended to 20D in the y direction.

To the best of author's knowledge, only one location is considered for the up/downstream discrete sister holes for the EESH scheme, which was initiated by Ely and Jubran [61]. In their configuration four discrete sister holes with diameters of 0.5D are placed 0.75D up/downstream of the primary hole at the same lateral position from the centerline. Note that these positions are defined with respect to the center of the main hole ellipse in the jet exit plane. This location of the sister holes is considered as the "base case" in this chapter. The up/downstream sister holes case is based on four active discrete sister holes, which are highlighted in red. To clarify, four discrete sister holes are placed at $x/D = \pm 0.75$ and $z/D = \pm 0.75$ with respect to the center of the exit main hole (highlighted in blue) for the base case.

The updated geometry for the simulations in this chapter is presented, the top and side views of the computational domain are shown in Figure 5.1.

The current simulations are carried out at a coolant air temperature of 250 K and mainstream temperature of 300 K, which satisfy the constant density ratio of $DR = 1.2$. In addition to the density ratio of 1.2, the density ratio of 2 is also used for the validation or grid sensitivity analysis of present simulations. Again, the available experimental data of Sinha et al. [8] is considered, where the coolant air temperature is 150 K with the same mainstream temperature (300 K).

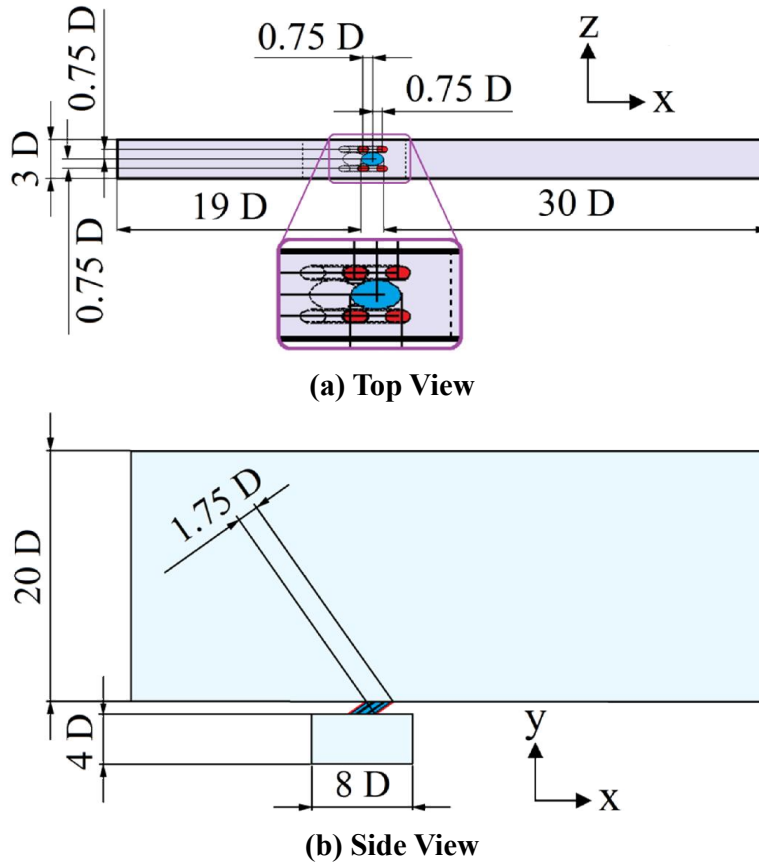


Figure 5.1: Geometry of the cylindrical hole with base case of the up/downstream discrete sister holes

The inlet coolant air velocity for the single (cylindrical) and up/downstream discrete sister holes can be found in Table 5.1.

Table 5.1: Plenum inlet velocity

Blowing Ratio (M)	Plenum inlet velocity [m/s]	
	Single Hole	Up/Downstream Discrete Sister Holes
0.25	0.136	0.273
0.5	0.273	0.545
1	0.545	1.091
1.5	0.818	1.636

The freestream turbulence intensity is set to 0.2% as stated in experimental data [8]. According to the numerical simulation of Azzi and Lakehal [80], this value is considered as 2% at the plenum inlet. The viscosity ratios of $\mu_t/\mu = 30$ and 50 are specified at the plenum and freestream inlets, respectively.

To modify the location of the discrete sister holes in the streamwise direction, the downstream sister holes for the first case are positioned at $x/D = \pm 0.80$ followed by increments of $0.10D$ until a final position of $1.2D$, thus resulting in 5 new discrete sister holes locations; this process is mirrored about the z axis for the upstream sister holes. For instance, the last location of the modified sister holes in the streamwise direction is $x/D = \pm 1.2$ and $z/D = \pm 0.75$. A similar process is undertaken for the sister holes in the spanwise direction and mirrored about the x axis.

5.2. COMPUTATIONAL OVERVIEW AND DOMAIN

In order to analyze the flow and thermal fields in film cooling, three-dimensional RANS analysis is employed using ANSYS FLUENT 14.0.0. The solutions are obtained by using the finite-volume method to discretize the RANS equations. The realizable $k-\epsilon$ turbulence model combined with the standard wall function is used to model the flow field. The ability of the realizable $k-\epsilon$ model to capture the jet separation for the film cooling flow application is reported in the work of Zhang and Hassan [22]. It has also been mentioned in the previous chapter (Section 4.3.1) that the realizable $k-\epsilon$ model combined with the standard wall function provided results which demonstrated better agreement with the experimental data in prediction of film cooling effectiveness than that obtained by the standard and RNG $k-\epsilon$ and the Reynolds-stress models for a flat-plate film cooling. Moreover, the standard wall function for the near-wall modeling approach outperformed the scalable and enhanced wall treatment.

The applied boundary conditions on the computational domain which includes the hot mainstream channel, a film cooling hole and a plenum are shown in Figure 5.2.

Since the quality of mesh plays a vital role in increasing the accuracy of the results, the structured hexahedral mesh is meticulously distributed across the computational domain. Note that the density of the grids in the near-wall region have been carefully set to achieve a y^+ value of greater than 30 and less than 60 [72]. The second order upwind solution scheme is used to solve the momentum, energy and turbulence model equations. The SIMPLEC algorithm is employed to solve the pressure-velocity coupling. The flow is considered as incompressible ideal

gas. The simulations are terminated when the normalized residuals reach 10^{-5} for all variables and 10^{-7} is considered for the energy equation.

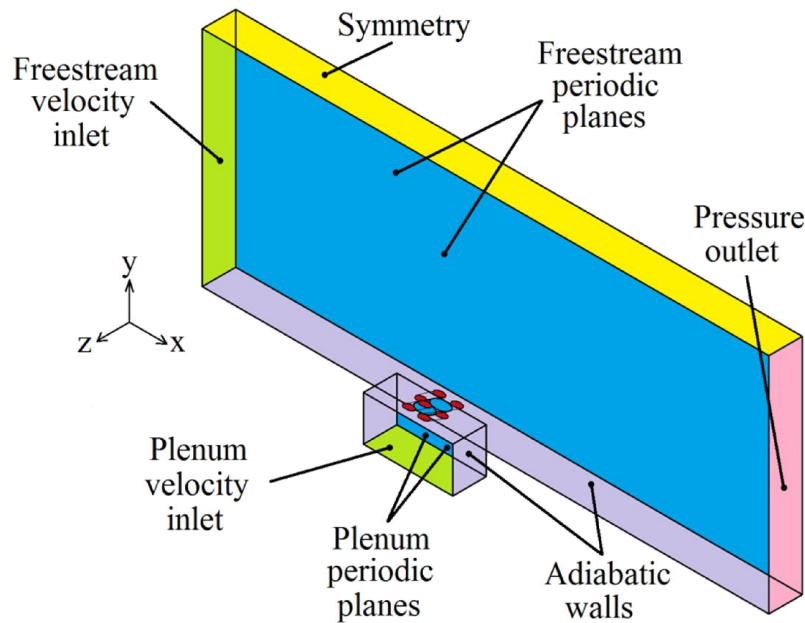


Figure 5.2: Schematic view of computational domain and boundary conditions

The centerline and laterally averaged effectiveness are calculated based on Equations (4.3) and (4.4), respectively.

5.2.1. COMPUTATIONAL GRID

The computational grid is generated by ANSYS GAMBIT 2.4.6. It is well known that the quality of mesh plays an important role in the accuracy level of the numerical results. Hence, the structured hexahedral mesh is meticulously distributed across the computational domain. As the standard wall function is employed, the density of the grids in the near-wall region can be carefully set to achieve the y^+ value which falls into the range of 30 to 60 [72].

Four different numbers of cells have been implemented ranging from 112,000 to 2,100,000 cells. Figure 5.3 shows the predicted centerline film cooling effectiveness results for four applied grids at a blowing ratio of 1 and density ratio of 2. It can be seen that the coarse mesh including 120,000 cells is not able to capture the jet separation close to the injection hole. Increasing the number of cells to 654,000 provided slightly better film cooling effectiveness

results in that region. By using a grid with 1,200,000 hexahedral cells, the jet separation can be captured and more accurate film cooling effectiveness results can be obtained. However, further increase in the number of cells to 2,100,000 does not result in any significant change in the centerline film cooling effectiveness results as the monitored parameter. Hence, the grid number with 1,200,000 cells is chosen as the grid independent solution for subsequent simulations in this chapter and Chapter 6.

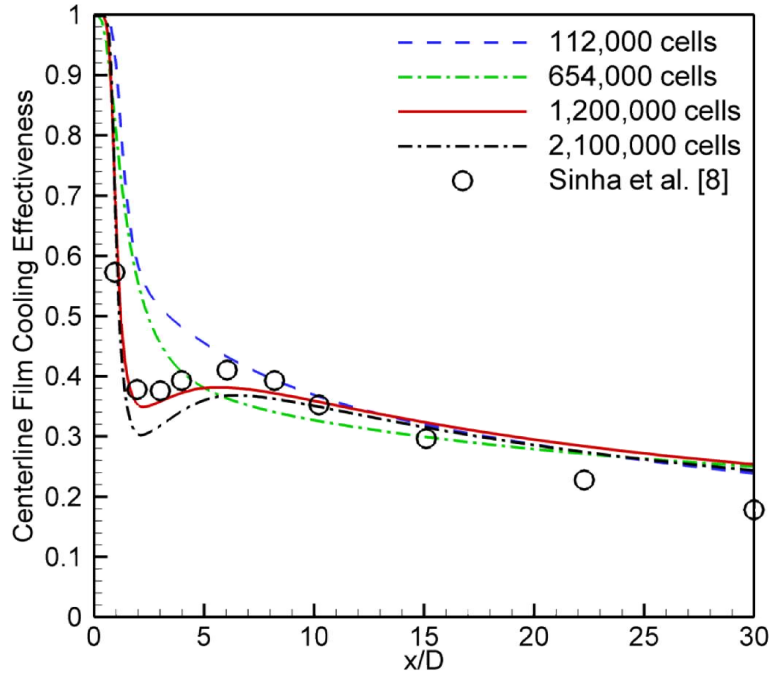


Figure 5.3: The grid sensitivity test ($M = 1$, $DR = 2$)

5.2.2. Effect of Mainstream Channel Height

The test section of the wind tunnel in the experimental setup of Sinha et al. [8] is $0.6 \times 0.6 \times 0.24$ m where the mainstream channel height is $47D$. By applying the free-slip or zero shear stress boundary condition (symmetry boundary condition), a lower height for the mainstream channel can be selected to reduce the computational cost. A detailed numerical study on four different channel heights of $5D$, $10D$, $20D$ and $40D$ is carried out by Zhang and Hassan [22]. They reported that the height of the mainstream channel should be extended to $20D$ in the y direction in order to be far enough to apply a symmetry boundary condition. Accordingly, the mainstream block is extended to $20D$ in the y direction for the present simulation. The obtained centerline film cooling effectiveness results for the channel heights of $10D$ (which was used for

the simulations in the Chapter 4) and 20D are presented for the density ratio of 2 and the blowing ratio of 1, as depicted in Figure 5.4. The results are compared against the available experimental data of Sinha et al. [8] and the numerical simulations of Liu et al. [45] and Zhang and Hassan [22].

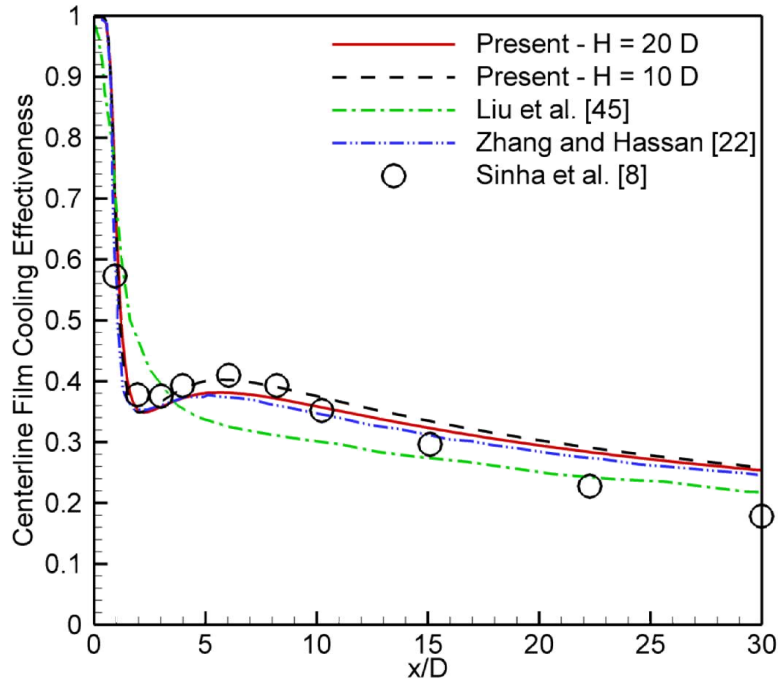


Figure 5.4: Effect of mainstream channel height on centerline film cooling effectiveness ($M = 1$, $DR = 2$)

It can be seen that the obtained centerline film cooling effectiveness with the channel height of 20D shows a slight improvement compared to that with 10D, particularly in the far downstream region. Although the channel height of 10D provided the better centerline film cooling effectiveness values in the reattachment region of the cooling jet $3 < x/D < 6$ in comparison with the experimental data, this can be considered as its general overprediction which continues to the farther downstream region. Moreover, the results with $H = 20D$ are in an excellent agreement with the numerical results of Zhang and Hasan [22]. Further to this, it can be seen that the employed realizable $k-\epsilon$ model with the standard wall function is able to capture the jet separation close to the injection hole at the high blowing ratio of 1, while it is missed in the numerical simulation of Liu et al. [45], where the $k-\epsilon$ model combined with scalable wall function is applied.

5.3. RESULTS

The following sections provide the results for low and high blowing ratios. Wherein the low blowing ratios cover $M = 0.25$ and 0.5 , while the high blowing ratios cover $M = 1$ and 1.5 . The first section presents the validation of the employed turbulence model against the available experimental data and numerical results in the literature. A detailed discussion on the results of the film cooling effectiveness can be found in the second section wherein, the centerline and laterally averaged effectiveness as well as the effectiveness contours over the plate's surface are presented. Finally, the associated flow structure with the aid of the velocity vectors and the temperature contours is analyzed at two different locations downstream of the injection holes. Note that the density ratio of 1.2 is employed to obtain the subsequent results.

5.3.1. Validation

The present predicted film cooling effectiveness results for the single cylindrical hole are validated against the experimental data of Sinha et al. [8]. The film cooling effectiveness results including the centerline and the laterally averaged effectiveness are also compared with the numerical simulation carried out by Ely and Jubran [61], as demonstrated in Figure 5.5.

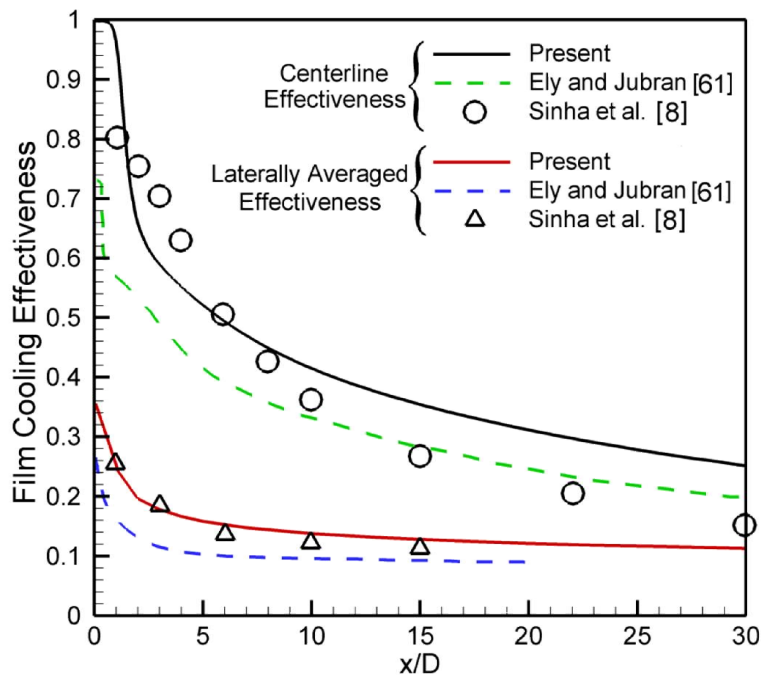


Figure 5.5: Film cooling effectiveness ($M = 1$, $DR = 2$)

In general, the predicted centerline film cooling effectiveness results are in good agreement with the experimental data. For the region close to the injection hole ($x/D < 8$), present results outperform the numerical results of Ely and Jubran [61]. However, the centerline film cooling effectiveness results are overpredicted in the far downstream region of the jet.

This overprediction of the centerline film cooling effectiveness results obtained with the $k-\epsilon$ models has been reported by Johnson et al. [4] as the errant nature of the isotropic assumption used in the $k-\epsilon$ models. On the other hand, the laterally averaged film cooling effectiveness results provided with the realizable $k-\epsilon$ model show an excellent agreement with the experimental data when compared with that obtained by Ely and Jubran [61].

5.3.2. Film Cooling Effectiveness

The predicted centerline film cooling effectiveness results for the streamwise modification of the discrete sister holes at the low blowing ratios of $M = 0.25$ and 0.5 and the high blowing ratios of $M = 1$ and 1.5 are presented in Figure 5.6. It should be mentioned here that the sister holes' film cooling is almost a new concept; therefore, to the best of the author's knowledge, there is no available experimental data in the open literature. Different cases have been investigated for the new location of the sister holes. For example, case 1x as x represents the streamwise locations along the x axis, where the discrete sister holes are placed at $x/D = \pm 0.80$ by keeping the spanwise location constant at $z/D = \pm 0.75$. Similarly, the other cases are named based on the order of changes in the streamwise direction with the increment of 0.10 until a final position of $1.2D$, which is named as case 5x. Note that for all variations in the streamwise direction, the spanwise (lateral) location of the sister holes is kept constant as that of the base case (i.e., $z/D = \pm 0.75$).

As shown in Figure 5.6(a), the effect of the streamwise variation in the location of the sister holes on the centerline film cooling effectiveness for the very low blowing ratio of 0.25 is almost negligible. In particular, this effect is completely vanished in the far downstream region of the injection holes. The increase in the blowing ratio provides a clear vision of the effect of the sister holes' location on the film cooling effectiveness results. It can be seen that for the blowing ratio of $M = 0.5$, in the low blowing ratio range, the farther locations of the discrete sister holes provide lower centerline film cooling effectiveness values compared to the base case in the region close to the injection hole ($x/D < 8$), as demonstrated in Figure 5.6(b). This can be

attributed to the effect of the sister holes on the counter rotating vortex pairs' strength close to the injection hole. The CRVP generated from the primary hole are significantly stronger after the injection location; hence, the closer sister holes to the primary hole can efficiently assist to counter the CRVP rotation. Therefore, the base case provides the maximum centerline film cooling effectiveness in the region $x/D < 8$. The centerline film cooling effectiveness values for the base case decay faster than other cases after $x/D \approx 8$ and it would not last long, as magnified in Figure 5.6(b). On the other hand, since the sister holes are placed farther upstream and downstream than the base case, the positive effect of the sister holes on the primary hole vortices would not be faded as fast as the one for the base case. For instance, a comparison between the base case and case 5x validates the aforementioned discussion. Note that for the higher blowing range, the centerline film cooling effectiveness at the high blowing ratios of 1 and 1.5 tends to decay continuously until $x/D \approx 5$ after the primary injection hole for the base case, case 1x and case 2x, as shown in Figure 5.6(c and d). This is attributed to a notable decrease in the jet lift-off effect by the desirable effect of the sister holes closer to the primary hole in the streamwise direction.

On the other hand, a minimum and a maximum can be distinguished in the film cooling effectiveness values for cases 3x, 4x and 5x close to the injection hole. This region is magnified in Figure 5.6(c) and highlighted as zone 1 in Figure 5.6(d). In the region very close to the injection hole ($x/D = 1$), the coolant jet is lifted-off from the plate's surface due to the high momentum of the jet and causes a minimum in the centerline film cooling effectiveness for cases 3x, 4x and 5x. The coolant jet is reattached to the surface due to the mainstream momentum in the streamwise direction which pushes the jet towards the wall surface and increases the centerline film cooling effectiveness in zone 1. The cooling jet detaches from the wall right after zone 1 for all cases; hence, a considerable decrease occurs in the centerline film cooling effectiveness from around 0.8 to the effectiveness of about 0.4 for all cases. This shows that the ACRVP are not sufficiently strong to defeat the CRVP generated from the primary hole. Farther downstream in zone 2, the centerline film cooling effectiveness increases again due to the mainstream momentum pushing the coolant jet and the vortices towards the surface. This is more easily recognized at the blowing ratio of 1.5 rather than $M = 1$. Overall, variations in the centerline film cooling effectiveness due to the changes in the position of the sister holes in the streamwise direction was not considerable; while the base case provided the highest

effectiveness value in the vicinity of the injection hole. Wherein, case 3x tends to remain at the mid-range of the centerline effectiveness values. For example, the centerline effectiveness for case 3x in the region of $x/D > 6$ demonstrates an increase of about 47% and 36% as compared to the base case for $M = 1$ and 1.5 , respectively.

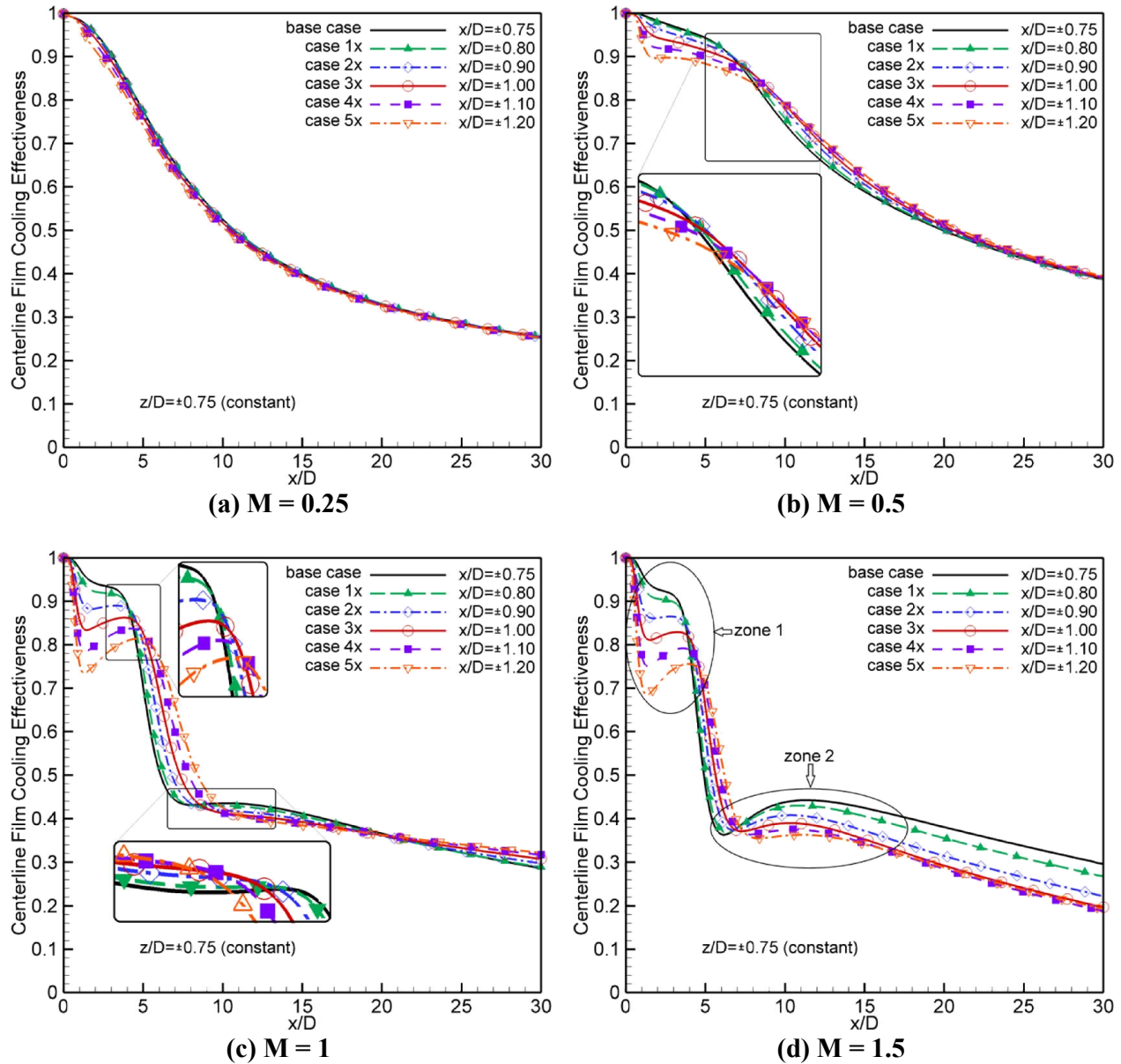


Figure 5.6: Centerline film cooling effectiveness – streamwise variation of the discrete sister holes' location

The effects of the spanwise variation in the location of the sister holes on the predicted centerline film cooling effectiveness for the low and high blowing ratios are demonstrated in

Figure 5.7. Unlike the streamwise variations of the sister holes' location, the spanwise variations show a profound effect on the centerline film cooling effectiveness results even at the low blowing ratio of 0.25. As shown in Figure 5.7(a), the film cooling effectiveness values gradually decrease from the base case to case 5z for $M = 0.25$. This indicates that the sister holes close to the main hole in the spanwise direction provide a significant effect on the cooling jet's flow to push it more towards the plate's surface.

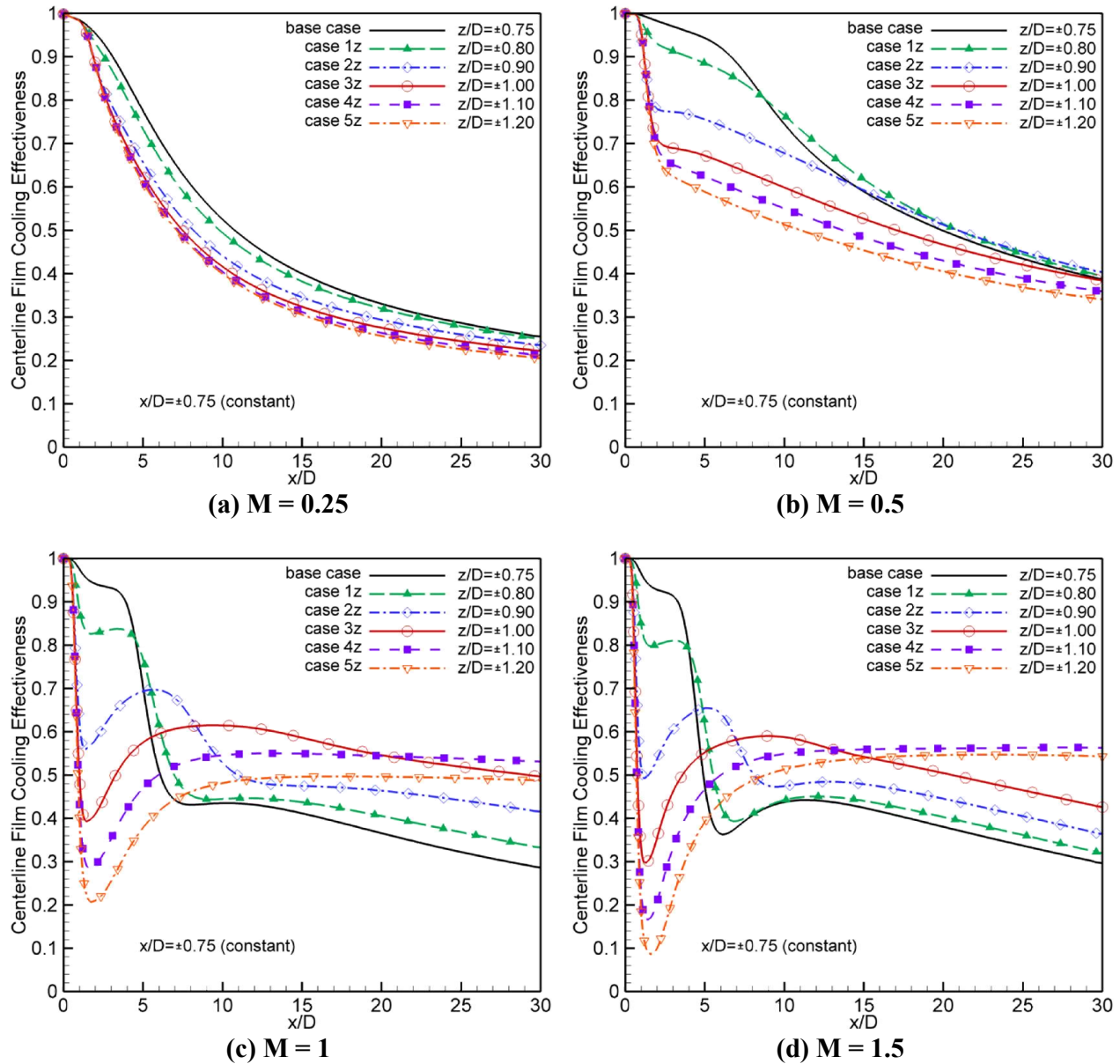


Figure 5.7: Centerline film cooling effectiveness – spanwise variation of the discrete sister holes' location

For the blowing ratio of 0.5, the trend of the film cooling effectiveness results is almost similar to that of $M = 0.25$ in the region close to the injection hole ($x/D < 10$). Note that the rate of decay for the base case is higher than other cases. Cases 1z and 2z outperform the base case in the farther downstream region.

Due to the high momentum of the injecting jet at the jet exit plane and the strength of the CRVP for the high blowing ratios, the jet lifts-off rapidly right after the injection hole. The notable decrease in the centerline film cooling effectiveness values for the cases that the sister holes are placed laterally farther to the main hole, indicates that the spanwise variations have a direct effect on the film cooling effectiveness results as depicted in Figure 5.7(c and d). Furthermore, the ACRVP's performance may depend on the location of the sister holes, which will be discussed in the flow structure section. However, there is no jet lift-off for the base case and case 1z in the vicinity of the injection hole. Surprisingly, the centerline film cooling effectiveness values for cases 2z elevates considerably after $x/D \approx 1$, where a plateau can be even recognized for cases 4z and 5z in the far downstream region of $x/D > 10$. This will be discussed more in the flow structure section by analysis of the vortex structure downstream of the injection hole. In general, case 3z plays a moderate role among other cases where it stands at a reasonable centerline film cooling effectiveness range in the whole domain. Note that case 2z provides higher film cooling effectiveness values close to the injection hole in comparison with case 3z.

In Figure 5.8, the laterally averaged film cooling effectiveness results for changes in the location of the sister holes along the streamwise direction are presented for the low and high blowing ratios. It is expected from the centerline film cooling effectiveness results that streamwise variations of the sister holes' location do not have a considerable effect on the low blowing ratio cases of $M = 0.25$ and 0.5, as shown in Figure 5.8(a and b), respectively. Putting the sister holes farther upstream and downstream of the main hole cannot positively affect the film cooling effectiveness results as compared to the base case even for the high blowing ratio cases. Note that the base case provides higher values for the laterally averaged film cooling effectiveness close to the injection hole ($x/D < 8$) for $M = 0.5$. In addition, the base case outperforms other cases in the far downstream region for the high blowing ratio of $M = 1.5$ (see Figure 5.8(d)). This verifies that the location of $x/D = \pm 0.75$ can be considered as the best candidate among all other cases for the streamwise variation of the sister holes' location. In the

other words, streamwise variation of the discrete sister holes' location does not have a notable effect on the laterally averaged film cooling effectiveness results.

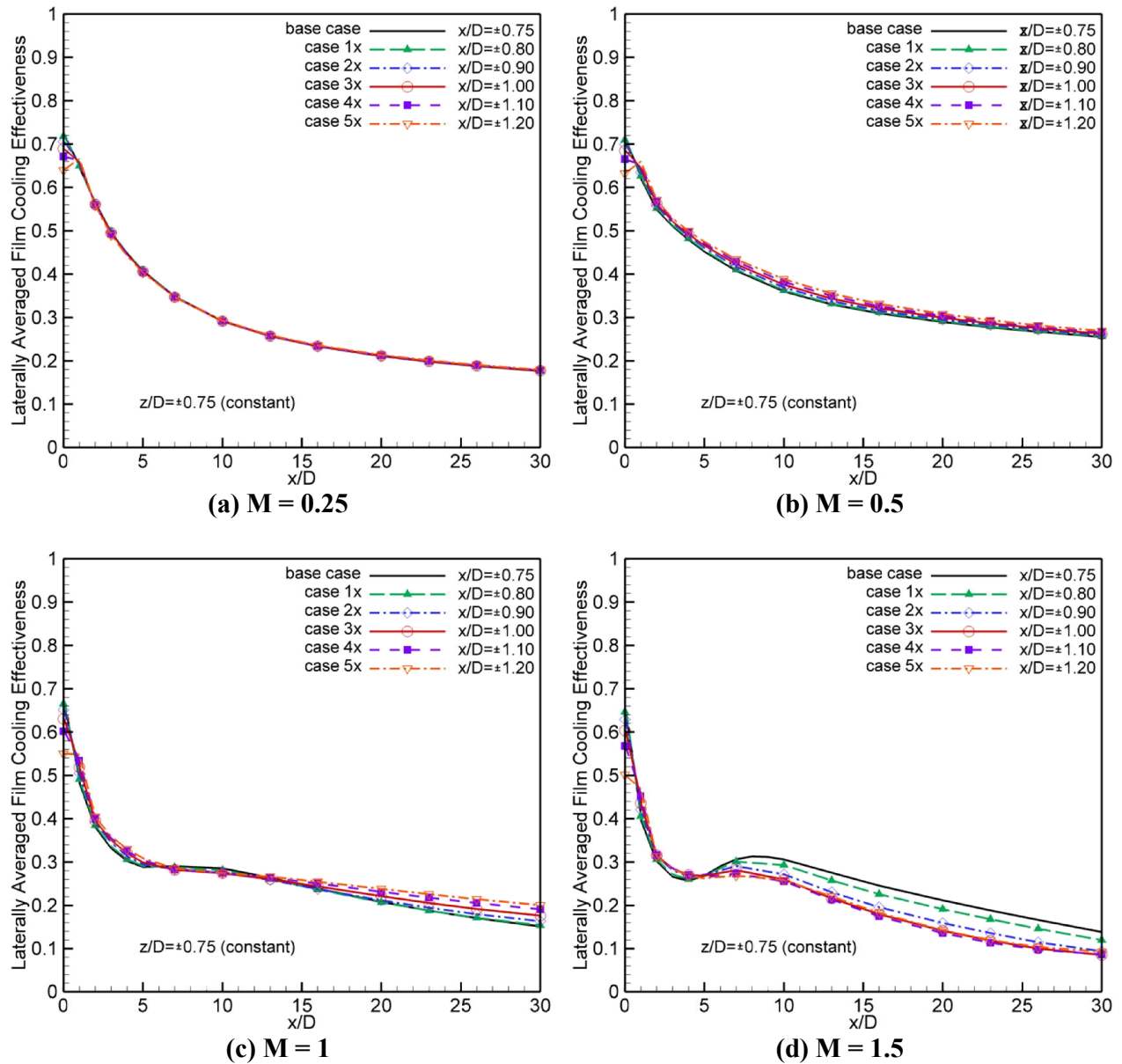


Figure 5.8: Laterally averaged film cooling effectiveness – streamwise variation of the discrete sister holes' location

On the other hand, the spanwise variations of the sister holes provide a more clear vision on the performance of the new locations. The laterally averaged film cooling effectiveness for the aforementioned variations is demonstrated in Figure 5.9 for four blowing ratios. Since the jet lift-off effect due to the counter-rotating vortices is not considerable for the very low blowing

ratio of $M = 0.25$, cases 1z to 5z provide similar effectiveness results as that of the base case, as shown in Figure 5.9(a). For the blowing ratio of 0.5, the effectiveness value for the base case, case 1z and case 2z continuously decline from 0.7 to 0.3. However, cases 3z, 4z and 5z perform different in the vicinity of the jet ($x/D \approx 2$). The decay rate in the film cooling effectiveness has decreased for cases 3z, 4z and 5z.

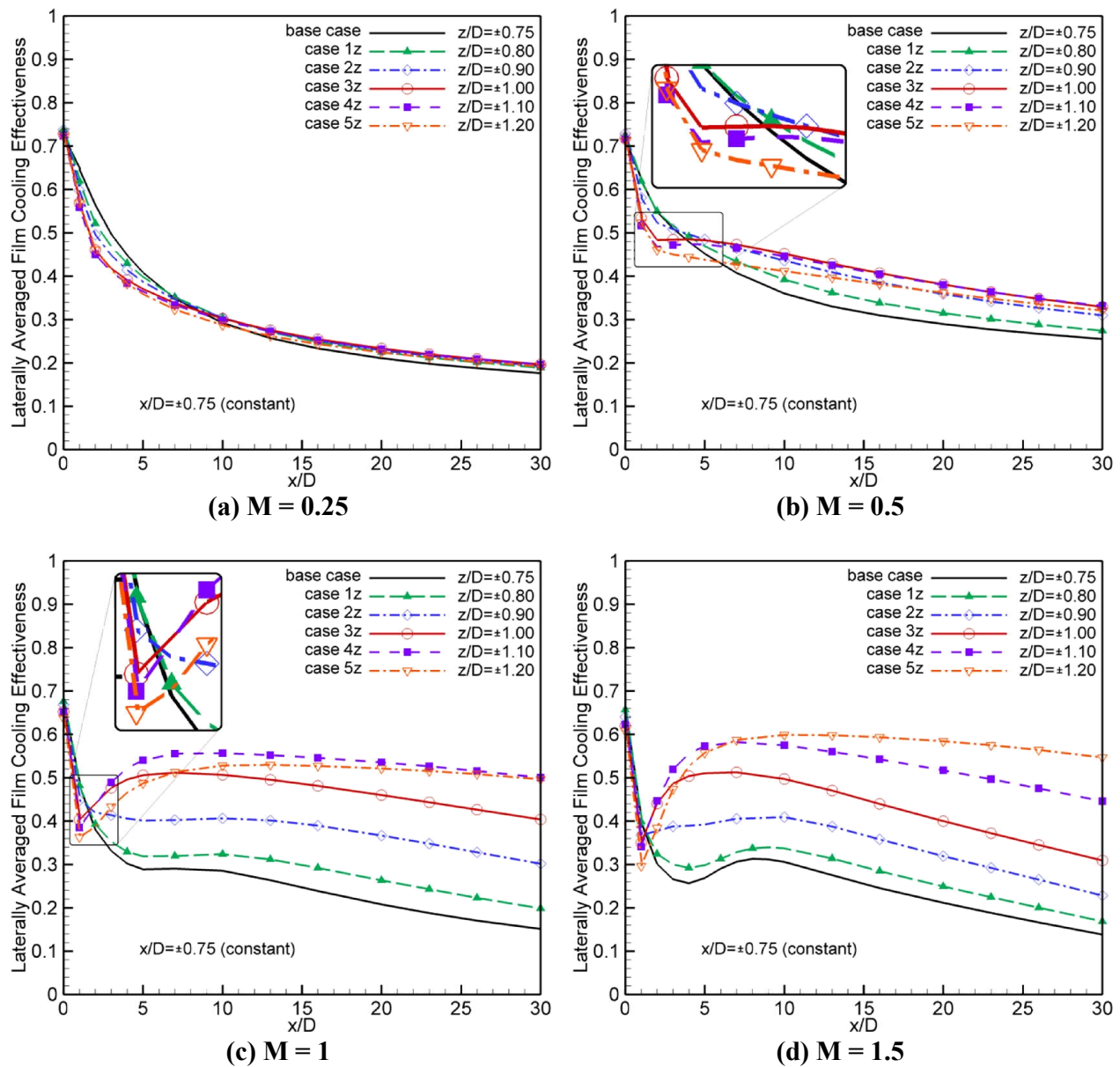


Figure 5.9: Laterally averaged film cooling effectiveness – spanwise variation of the discrete sister holes' location

At the high blowing ratios, a sudden decrease occurs in the film cooling effectiveness results right after the injection hole, which can be seen in the magnified region at $M = 1$, as shown in Figure 5.9(c and d). It can be interpreted as the jet lift-off effect where the cooling air jet detached from the plate's surface right after the injecting hole. Note that the direct effect of the ACRVP on the CRVP in the vicinity of the injecting hole caused reattachment of the coolant air to the plate's surface for cases 3z, 4z and 5z after $x/D \approx 1$. For the base case as well as cases 1z and 2z, the jet lift-off is vanished; wherein the maximum laterally averaged film cooling effectiveness value is obtained for case 2z. In spite of the sudden drop in the film cooling effectiveness values for cases 3z, 4z and 5z in $x/D \approx 1$, their outstanding performance downstream the vicinity of the jet is remarkable at the high blowing ratios of 1 and 1.5. For instance, the laterally averaged film cooling effectiveness for case 3x shows about 78% and 49% increase as compared to the base case for $M = 1$ and 1.5, respectively. It should be mentioned here that although cases 4z and 5z provide a plateau in the film cooling effectiveness results in the downstream region of $x/D > 8$ at high blowing ratios, they have to be manufactured close to their neighbor sister holes. The manufacturing limitations have to be taken into the considerations regarding the material strength and the application of the film cooling holes such as leading edge film cooling. As mentioned before, the effect of the streamwise variations in the location of the sister holes on the centerline and laterally averaged film cooling effectiveness results were negligible; while the spanwise variations provide a significant improvement in the effectiveness results. Accordingly, the main focus of the subsequent analysis is on the variations in the spanwise direction and comparing the results with the base case discrete sister holes.

The local film cooling effectiveness contours on the plate's surface can bring a better insight into the effect of the modification of the sister holes' location on the adiabatic film cooling effectiveness. A two-dimensional distribution of the local film cooling effectiveness on the plate's wall surface for the base case as well as cases 2z, 3z and 4z at the blowing ratios of $M = 0.25, 0.5, 1$ and 1.5 are depicted in Figure 5.10.

In Figure 5.10(a), the film cooling effectiveness contours for the base case show that the coolant is more concentrated in the region close to the main injection hole for all blowing ratios as compared to other cases. This has also been confirmed by the aforementioned film cooling effectiveness graphs and may be attributed to the dominant effect of the very close sister holes on the main coolant air flow as a result of a decrease in the jet lift-off effect.

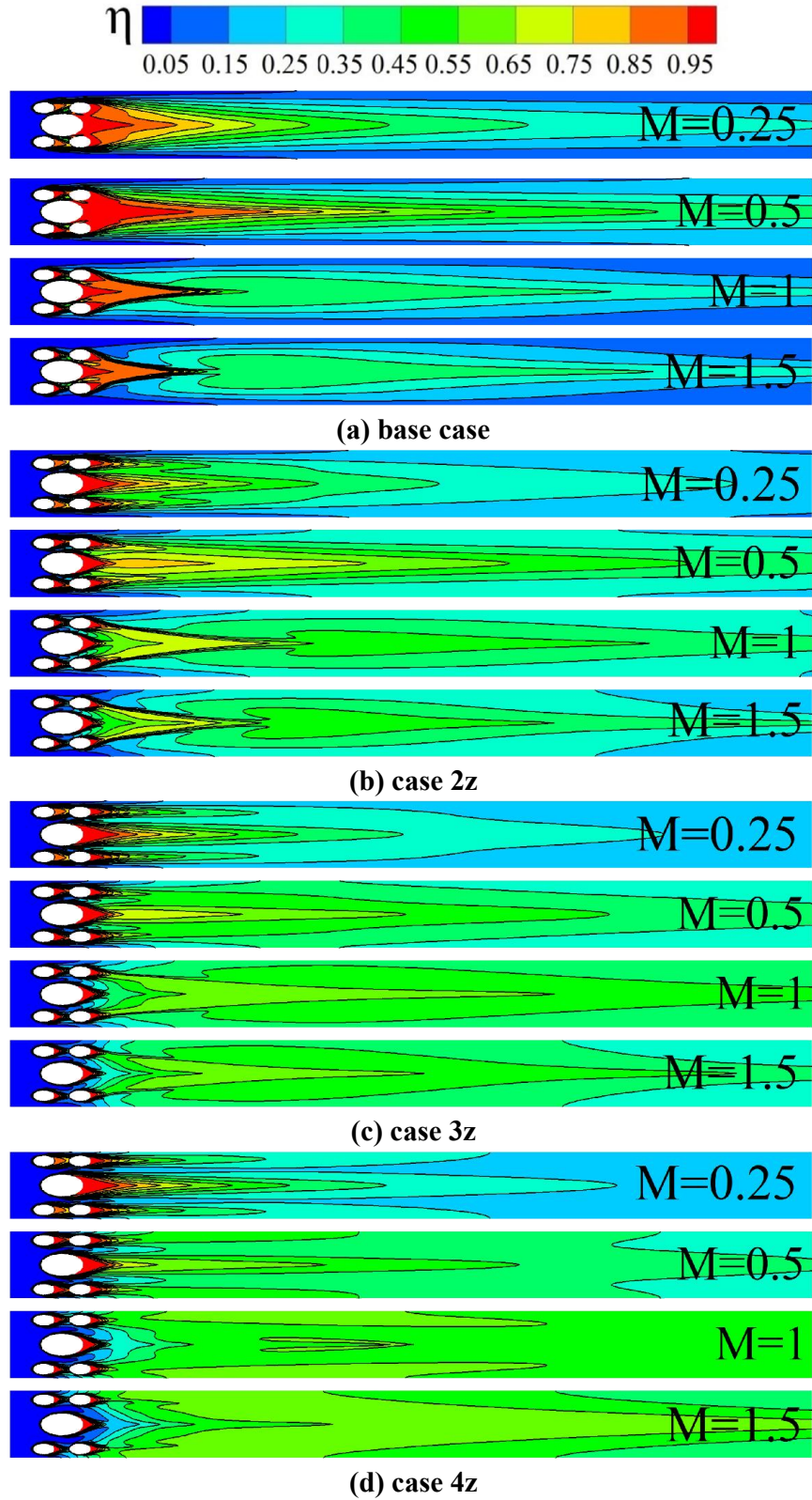


Figure 5.10: Local film cooling effectiveness for different blowing ratios

Moreover, the coolant air flow exiting from the sister holes does spread in the lateral direction as much as other cases; hence, it cannot provide enough coverage for the coolant close to the periodic boundaries (i.e., $z/D = \pm 1.5$). For the case 2z, the lateral spreading of the coolant air is evident even for the low blowing ratios as compared to the base case.

The film cooling effectiveness is gradually shifted from high values to low values downstream of the main injection hole for cases 2z, 3z and 4z for the low blowing ratios of 0.25 and 0.5. This shows that the coolant air jet may remained attached to the surface farther downstream of the hole, which can be seen in Figure 5.10(b–d).

In general, placing the sister holes in farther spanwise locations from the primary hole can result in lower film cooling effectiveness values in the region close to the injection hole. However, it provides better lateral distribution of the cooling air in the farther downstream region for high blowing ratios of $M = 1$ and 1.5. It can also be seen in Figure 5.10(c and d) that the hot mainstream flow has penetrated to the areas between the main hole and the sister holes for cases 3z and 4z at the high blowing ratios. This region should also be taken into consideration where the upstream sister holes cannot provide a suitable coverage of the coolant for surrounding area of the main jet. Overall, the lateral spread of the coolant from the sister holes in the far downstream region of the injection hole is directly dependent on the spanwise location of the sister holes. Placing the sister holes in farther locations from the centerline increases the lateral spread of the coolant air over the plate's surface.

5.3.3. Flow Structure

The visualization of the flow field is necessary to provide a better understanding of the film cooling effectiveness results, which have already been discussed. Herein the secondary flow with the aid of the velocity vectors combined with the temperature contours are depicted in the planes perpendicular to the plate's surface (yz plane) at $x/D = 1$ and 5 downstream of the trailing edge of the primary hole.

It has been found that the base case provided the higher film cooling effectiveness values in comparison with other cases in the region close to the injection hole for the low blowing ratios of 0.5 and 0.25. Also, case 3z provided similar laterally averaged film cooling effectiveness values as that of cases 4z and 5z; wherein the maximum effectiveness in far downstream region is obtained with case 3z for the blowing ratio of 0.5, as shown in Figure 5.9(b). Accordingly,

comparisons of the flow structure between the base case and case 3z at $x/D = 1$ and 5 for the blowing ratios of $M = 0.25$ and 0.5 are shown in Figure 5.11 and Figure 5.12. The obtained flow structures have also been compared with the results from the single cylindrical case in the absence of sister holes.

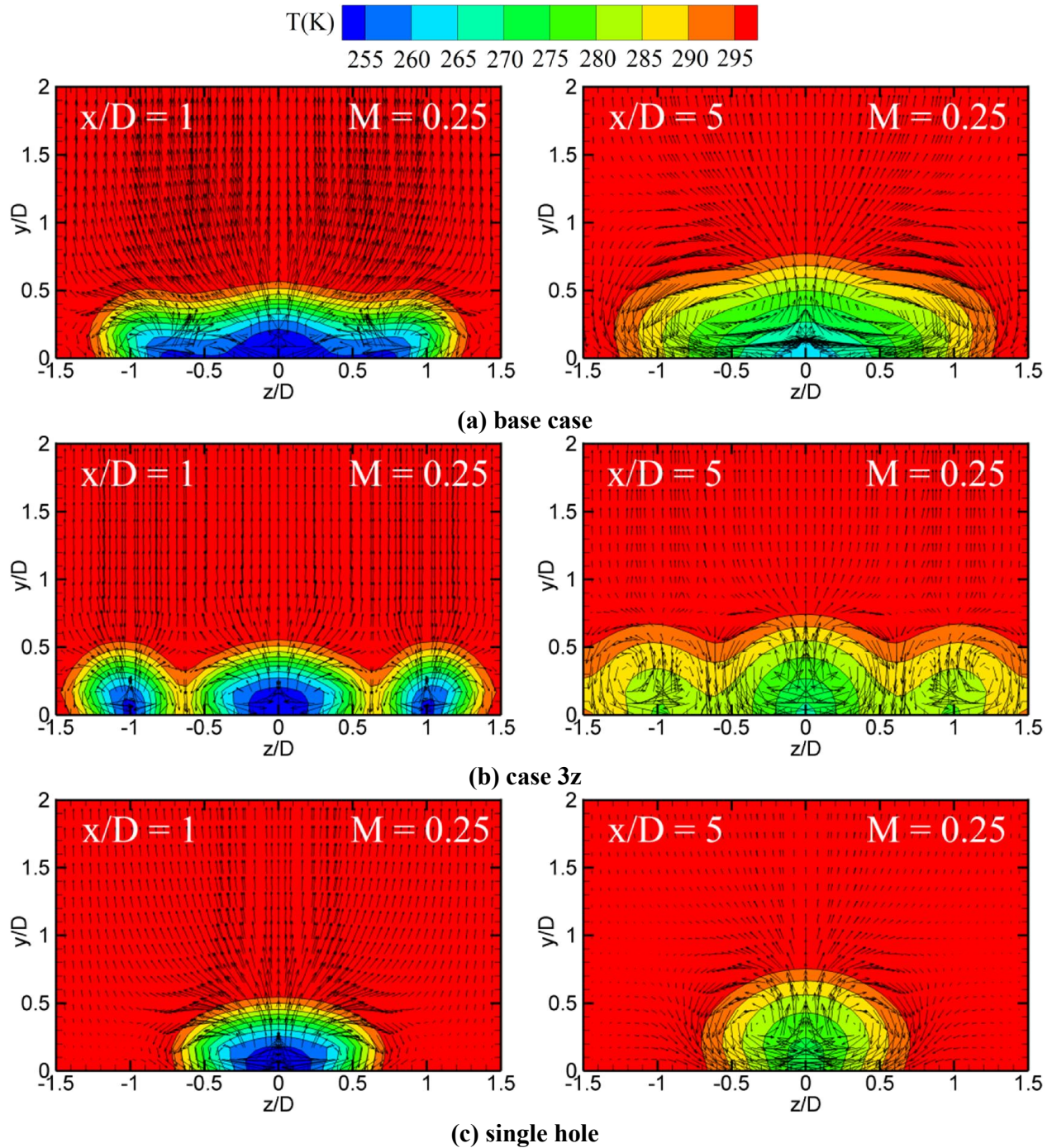


Figure 5.11: Temperature contours and velocity vectors at $x/D = 1$ and 5 for $M = 0.25$

In the vicinity of the jet ($x/D = 1$), the CRVP for the base case are almost vanished and the vortices that can be seen at $z/D = \pm 0.9$ are the ACRVP generated from the sister holes for $M = 0.25$. This provides a fully attached coolant air to the plate's surface (see Figure 5.11(a and b)).

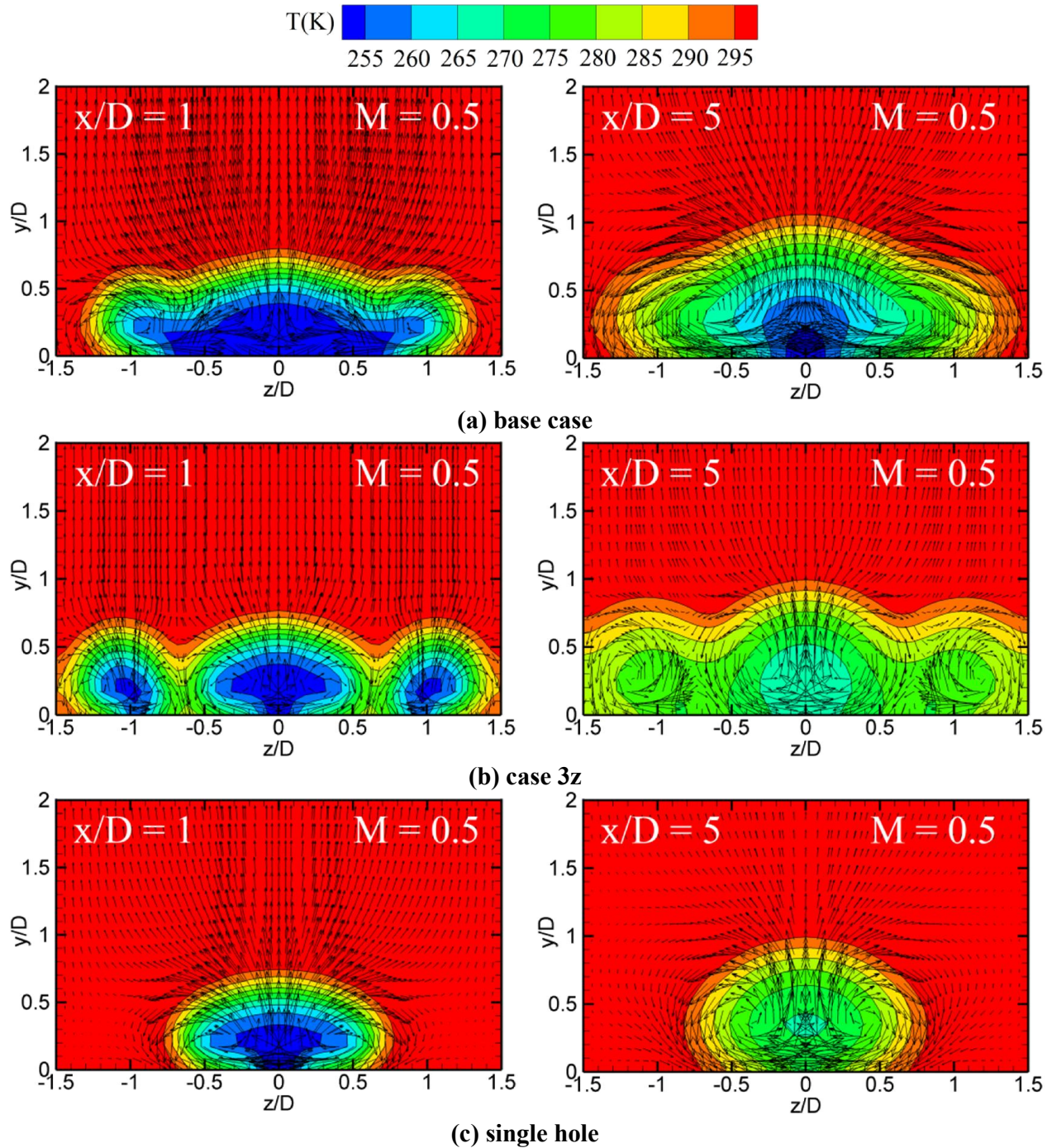


Figure 5.12: Temperature contours and velocity vectors at $x/D = 1$ and 5 for $M = 0.5$

For case 3z, The strength of the ACRVP for the sister holes is not sufficient to overcome the CRVP generated from the primary hole, as they have been placed in farther spanwise locations compared to the base case. Overall, the sister holes' flow not only did not affect the primary CRVP, but also they have generated their own smaller CRVP, which can be seen in Figure 5.11(b) at $x/D = 1$. These results are also extended to the farther downstream region of $x/D = 5$.

The more lateral coverage of the coolant is obtained from case 3z than the base case at $x/D = 5$ for $M = 0.25$, which results from the farther placement of the sister holes from the centerline. This could lead to an increase in the laterally averaged film cooling effectiveness for case 3z in comparison with the base case farther downstream of $x/D > 10$ which has been shown in Figure 5.9(a). The hot mainstream flow close to the periodic boundaries is completely vanished at $x/D = 5$, as depicted in Figure 5.11(b).

Similar results can also be seen for the blowing ratio of $M = 0.5$, as shown in Figure 5.12. Likewise, for the very low blowing ratio of 0.25, the cooling jet remains attached to the plate's surface for the single hole case and no jet lift-off occurs at $M = 0.5$. It should be noticed here that as a result of the increasing jet momentum for $M = 0.5$ the ACRVP from the sister holes became stronger to defeat the primary hole's CRVP. This effect becomes more clear at $x/D = 5$ where the ACRCP meet the vortices from the primary hole at $z/D = \pm 0.7$; hence, a higher laterally averaged film cooling effectiveness is achieved for case 3z at $M = 0.5$ as demonstrated in Figure 5.9(b).

For the high blowing ratios of $M = 1$ and 1.5, the flow structure combined with the temperature contours are depicted in Figure 5.13 and Figure 5.14, respectively. The obtained results include the base case, cases 2z, 3z, 4z and the single hole. While the coolant is almost detached from the wall at $x/D = 1$, the CRVP for the base case are vanished and the ACRVP can be recognized at $z/D = \pm 1$, as shown in Figure 5.13(a and e). The height of the cooling jet increases in the farther downstream region of $x/D = 5$ and a pair of vortices are seen at $z/D = \pm 0.6$ for the base case. It seems that the cooling jets from the primary and sister holes are combined together and have formed as a unified cooling jet. This can be attributed to the mixing of the coolant with the mainstream due to the decrease in the strength of the ACRVP as the coolant loses its momentum farther downstream of the injection hole.

It is worth mentioning here that the decrease in the centerline film cooling effectiveness from the base case to case 5z for the high blowing ratio cases, which are shown in

Figure 5.7(c and d), can be easily recognized by looking at the coolant's jet lift-off at $z/D = 0$ for different cases. In Figure 5.13(b), the ACRVP of the sister holes played a successful role to defeat the CRVP for case 2z at $x/D = 1$, wherein the coolant core of the main hole is still connected to the coolants from the sister holes at a moderate temperature of about 270 K.

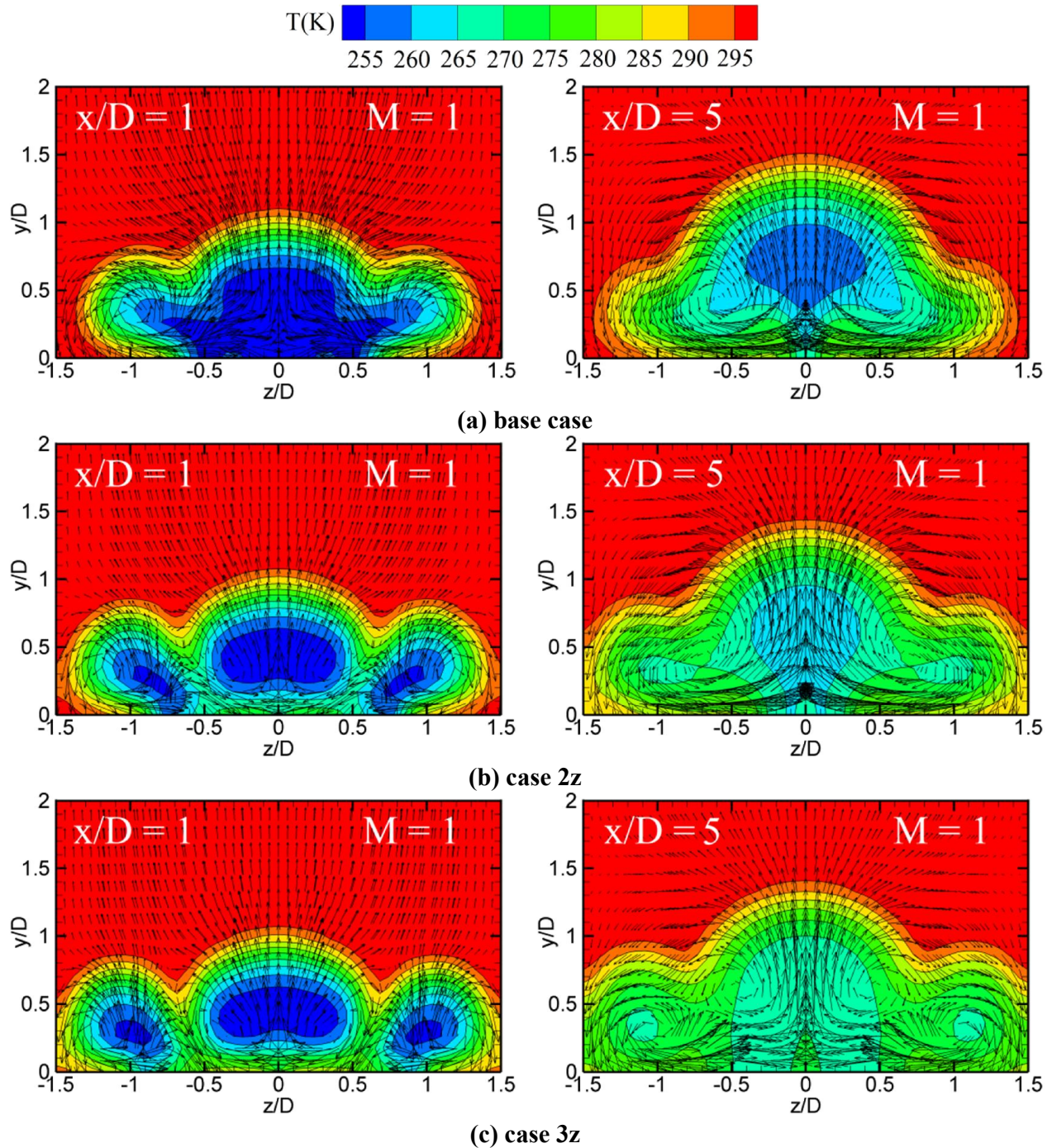


Figure 5.13: Temperature contours and velocity vectors at $x/D = 1$ and 5 for $M = 1$

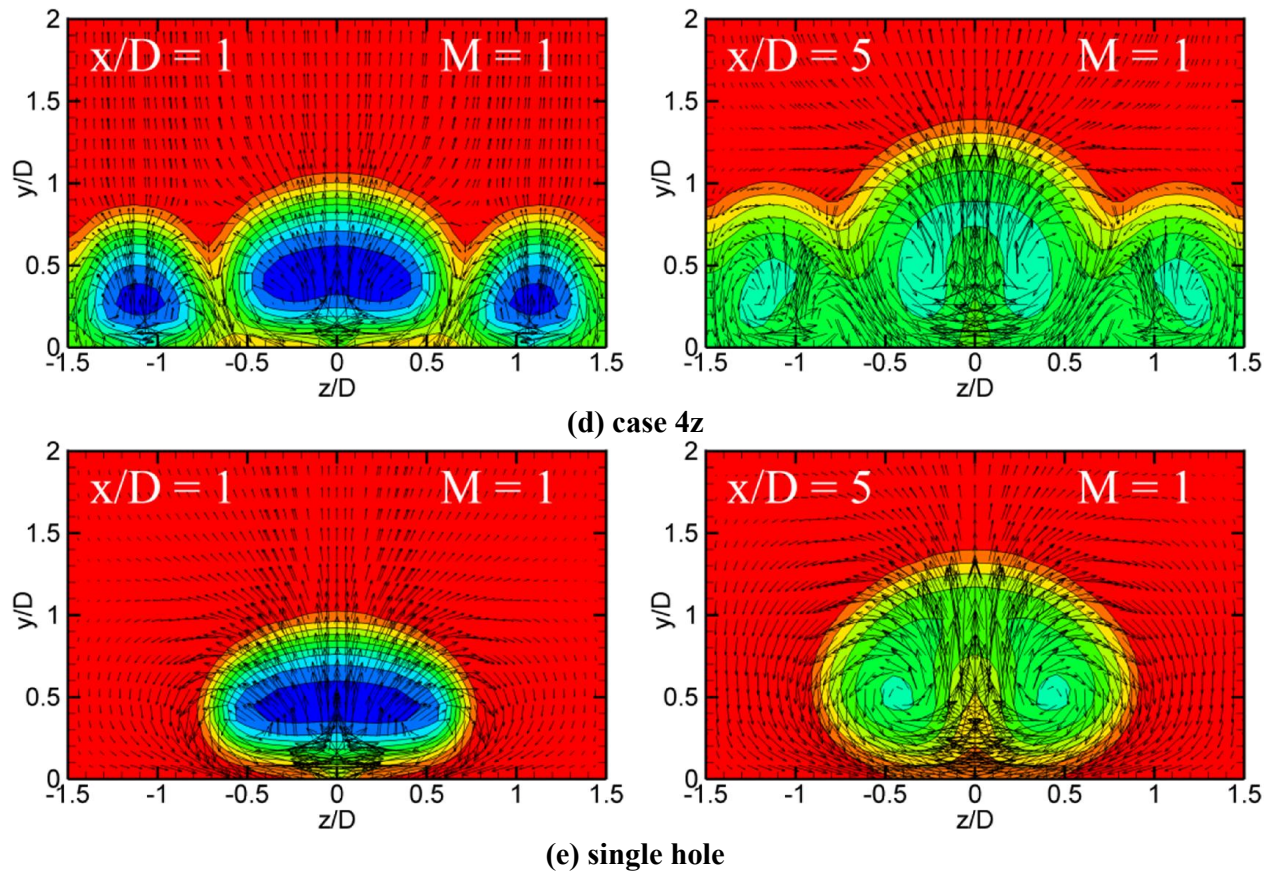


Figure 5.13 (cont.): Temperature contours and velocity vectors at $x/D = 1$ and 5 for $M = 1$

Moreover, the vortices which have been seen for the base case at $x/D = 5$ became weaker for case 2z and were at relocated $z/D = \pm 0.7$. This elevates the lateral coverage of the coolant for case 2z. For cases 3z and 4z, the ACRVP are not able to act as efficiently as the ones for the base case and case 2z at $x/D = 1$, as illustrated in Figure 5.13(c and d).

It is interesting that two pairs of vortices are formed for cases 3z and 4z at $x/D = 5$ instead of one vortex pair for the base case and case 2z. These extra vortex pairs located at $z/D = \pm 0.5$ and $y/D = \pm 0.6$ assist to spread the top side of the jet for case 3z as compared to case 2z. The hot mainstream flow is penetrated underneath the coolant for case 4z at $x/D = 1$ and the ACRVP are not able to successfully affect the primary hole's vortices, however a uniform flow with mid-range temperature is distributed close to the wall region.

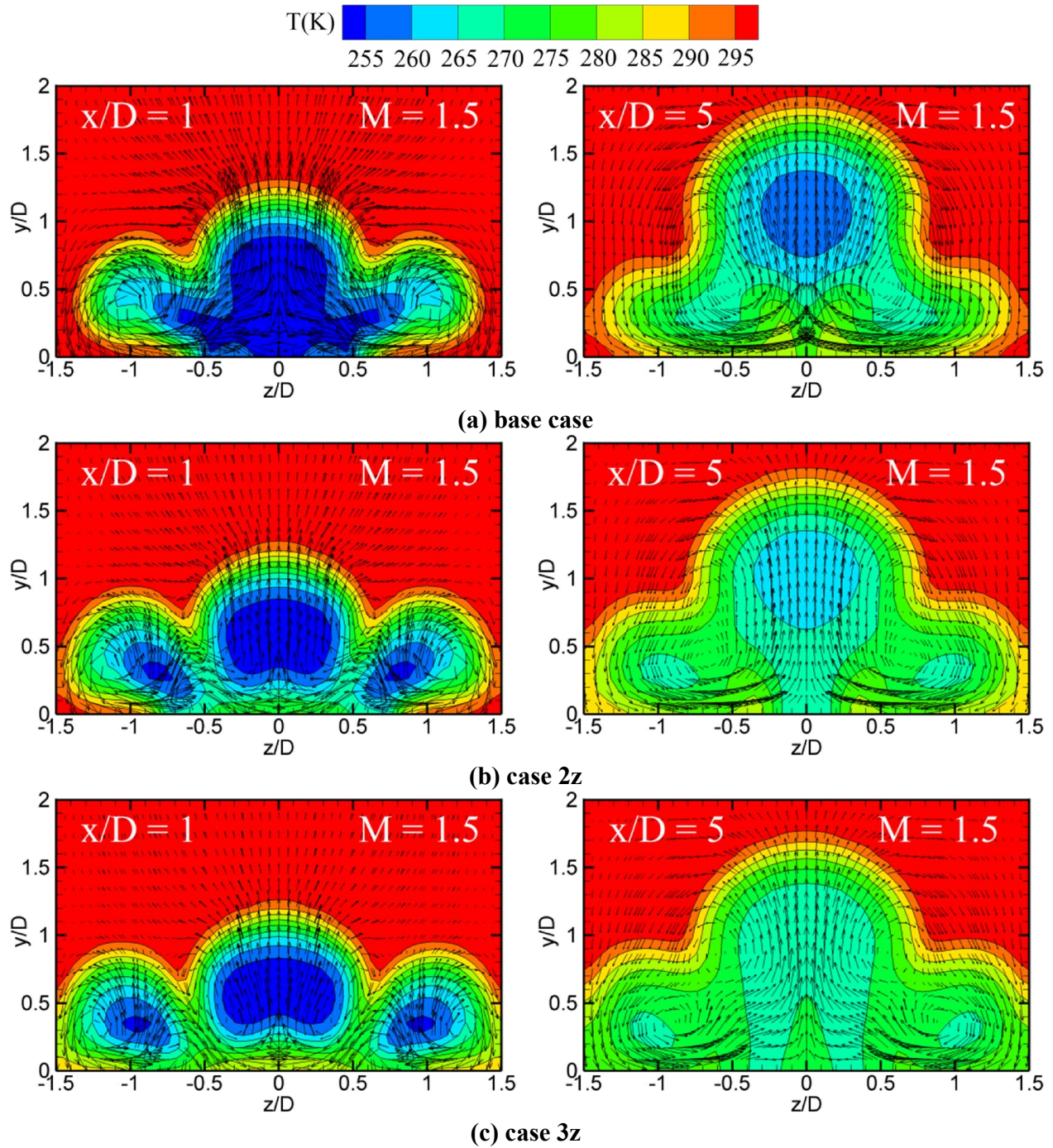


Figure 5.14: Temperature contours and velocity vectors at $x/D = 1$ and 5 for $M = 1.5$

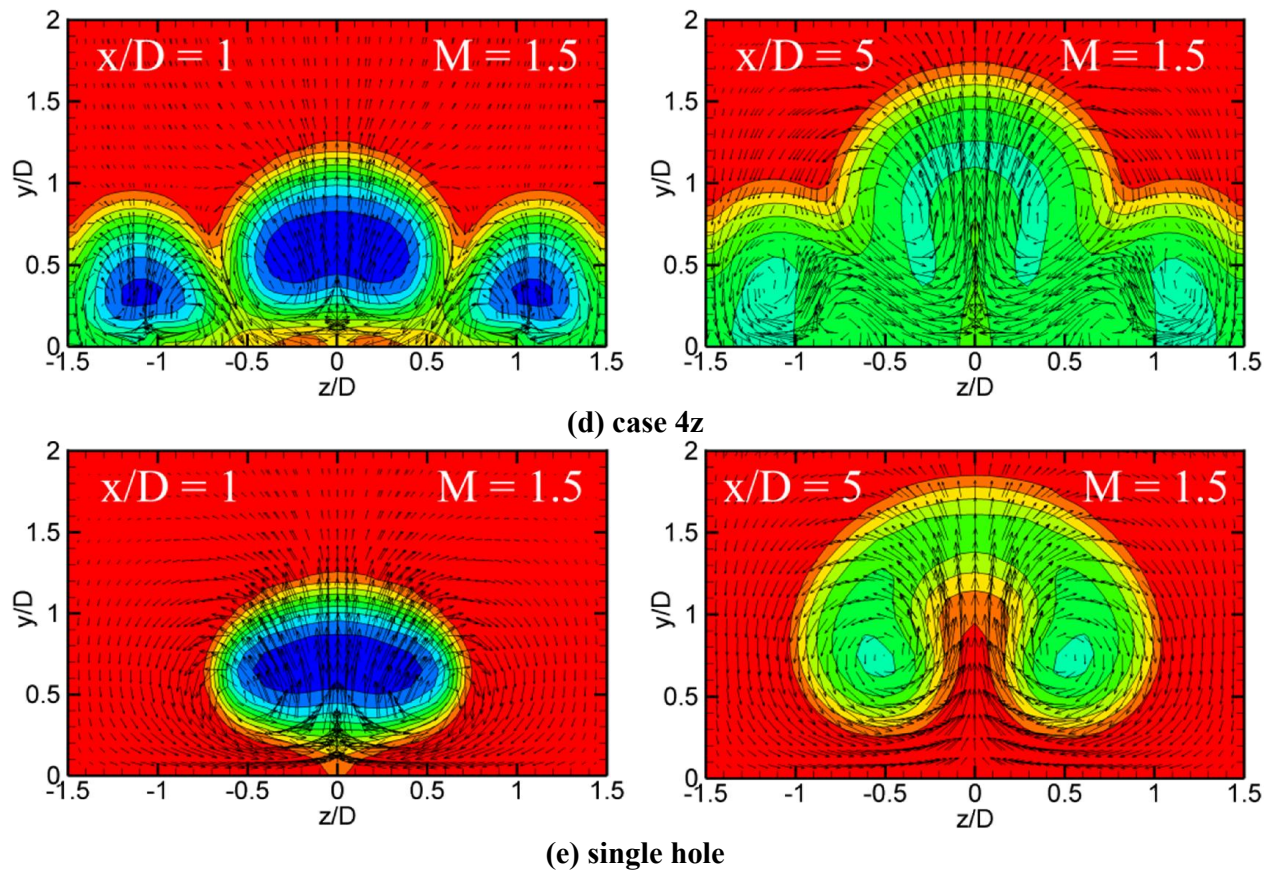


Figure 5.14 (cont.): Temperature contours and velocity vectors at $x/D = 1$ and 5 for $M = 1.5$

In general, the trend of results herein for the highest blowing ratio of 1.5 is almost similar to that of $M = 1$. Some aspects of the results which are noticeable are discussed as follows. As depicted in Figure 5.14(e), the cooling jet is completely lifted-off from the surface for the single hole. The vertical expansion of the cooling jet in the y direction at $x/D = 5$ has noticeably decreased from $y/D = 1.9$ for the base case to the value of 1.7 for case 4z. This decreasing trend can also be seen for cases 2z and 3z. It shows the desirable effect of the sister holes on the jet lift-off in the farther downstream locations as they are positioned in farther spanwise locations. This could be attributed to the plateau that has occurred in the laterally averaged film cooling effectiveness results for cases 4z and 5z at $M = 1$ as well as that for case 5z at $M = 1.5$.

5.4. CONCLUSIONS

In this chapter, numerical simulations of the film cooling performance using modified locations of the discrete sister holes have been investigated. The location of the up/downstream

discrete sister holes was changed individually in the streamwise and spanwise directions with respect to the base case where the sister holes are located at $x/D = z/D = \pm 0.75$ from the main hole's center.

Analysis results for the centerline and laterally averaged film cooling effectiveness show that insignificant effects are produced with variations in the streamwise direction and similar results are obtained to that of the base case. Hence, the base case with sister holes' location of $x/D = \pm 0.75$ is considered the better candidate among all other cases for the streamwise variations.

On the other hand, spanwise variation of the sister holes' location had a significant effect on the effectiveness results. Wherein, case 3z tends to remain in the mid-range of the film cooling effectiveness results across the whole domain. For example, the obtained laterally averaged film cooling effectiveness results for case 3x demonstrates an increase of about 78% and 49% as compared to the base case for $M = 1$ and 1.5, respectively.

The lateral spreading of the coolant air from the sister holes in the far downstream region of the injection hole is directly dependent on the spanwise location of the sister holes. Wherein placing the sister holes in the farther locations from the centerline increases the lateral spread of the coolant air over the plate's surface. This has also been verified through the flow structure analysis.

6. SISTER SHAPED SINGLE-HOLE SCHEMES

In the present chapter, a numerical investigation is conducted on the film cooling performance from novel sister shaped single-hole. Three types of the novel sister shaped single-hole (SSSH) schemes namely downstream, upstream and up/downstream SSSH, are designed based on merging the discrete sister holes to the primary hole in order to reduce the jet lift-off effect and increase the lateral spreading of the coolant air on the plate's surface as well as a reduction in the amount of coolant in comparison with the discrete sister holes. Simulations are performed at four blowing ratios of 0.25, 0.5, 1 and 1.5. The obtained results are compared with a cylindrical hole and a forward diffused shaped hole.

6.1. PROBLEM STATEMENT

The flat-plate film cooling with a cylindrical hole geometry is simulated based on the experimental work of Sinha et al. [8]. As depicted in Figure 6.1, the computational domain is extended to $19D$ and $30D$ from the leading edge (LE) and trailing edge (TE) of the primary injection hole, respectively. The geometry is also extended to $3D$ in the lateral (spanwise) direction to satisfy the pitch-to-diameter ratio of 3. The primary injection hole is inclined at 35° to the freestream flow with the length-to-diameter ratio of 1.75. The primary hole diameter (D) is 12.7 mm. The height of the freestream channel is extended to $20D$ in the vertical direction (y). A plenum with dimensions of $8D \times 4D \times 3D$ is considered before injecting the coolant air to the freestream flow. Further details of the simulation of the cylindrical hole case can be found in Chapter 4 (Section 4.1).

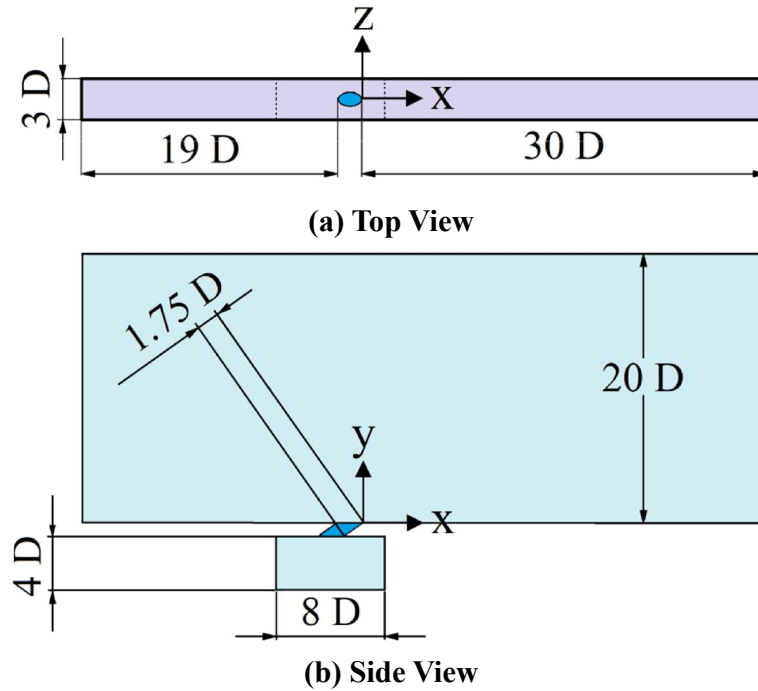


Figure 6.1: Geometry and computational domain of the cylindrical hole

The close-up of the top and side views of the cylindrical hole and 15° forward diffused shaped hole are shown in Figure 6.2. The original Cartesian coordinate system is placed at the trailing (downstream) edge of the jet exit hole (i.e., x, y, z), which is used to address all the simulation results. In order to ease the design process of the sister shaped single-hole, a secondary coordinate system (i.e., x', y', z') is placed after a length of $1D$ from the injection pipe entrance at the center of the primary cylindrical part.

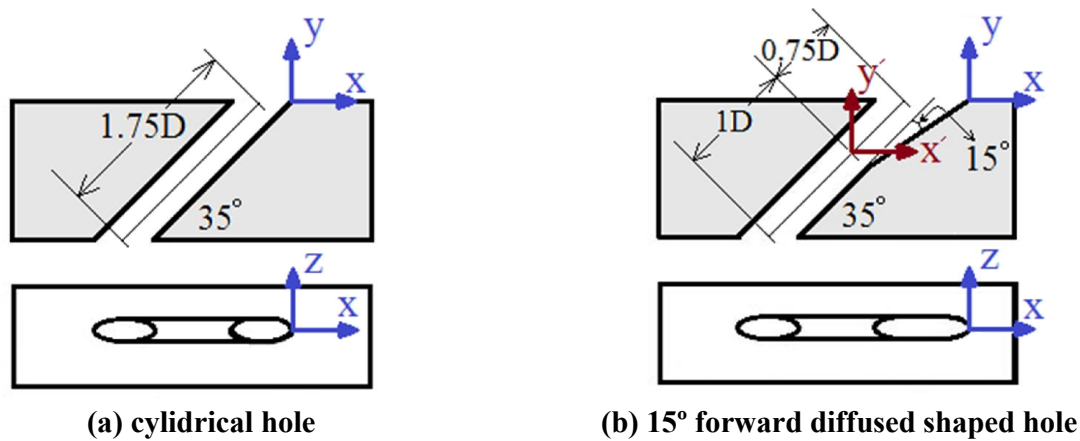


Figure 6.2: Close-up of the side and top views of (a) cylindrical hole and (b) 15° forward diffused shaped hole (not drawn to scale)

To make the sister shaped single-holes schemes, the discrete sister holes should be relocated at the origin of the secondary coordinate system with a specific inclination and rotation with respect to that coordinate system. Finally, the discrete sister holes will be merged to the main hole.

The formation of downstream SSSH scheme is depicted in Figure 6.3 which can be explained in three individual steps as follows, Step 1: after placing the two downstream discrete sister holes at the origin of the secondary coordinate system position (aligned with the primary hole inclination of 35°), they are rotated by 15° with respect to the negative direction of the z' axis. Step 2: the downstream sister holes are spread into the spanwise direction by 25° with respect to the y' axis. Step 3: finally the downstream sister shaped single-hole configuration is formed by merging the primary hole to the rotated discrete sister holes and cutting them at the plate's surface plane.

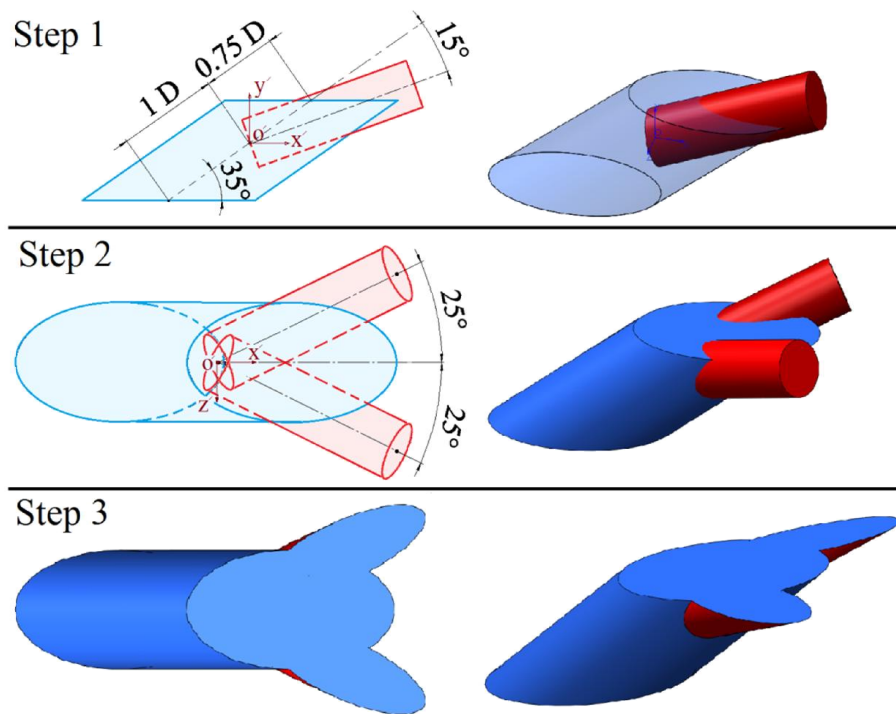


Figure 6.3: Design concept of downstream sister shaped single-hole (Downstream SSSH)

Similarly, three steps have to be taken in order to make the upstream SSSH scheme as demonstrated in Figure 6.4.

Step 1: after placing the two downstream discrete sister holes at the origin of the sub-coordinate system position (aligned with the primary hole inclination of 35°), they are rotated by 55° with respect to the positive direction of the z' axis. They will be positioned parallel to the y' axis. Step 2: the upstream sister holes are spread into the spanwise direction by 45° with respect to the x' axis. Step 3: the upstream SSSH is formed by merging all holes together and cutting them at the plate's surface plane.

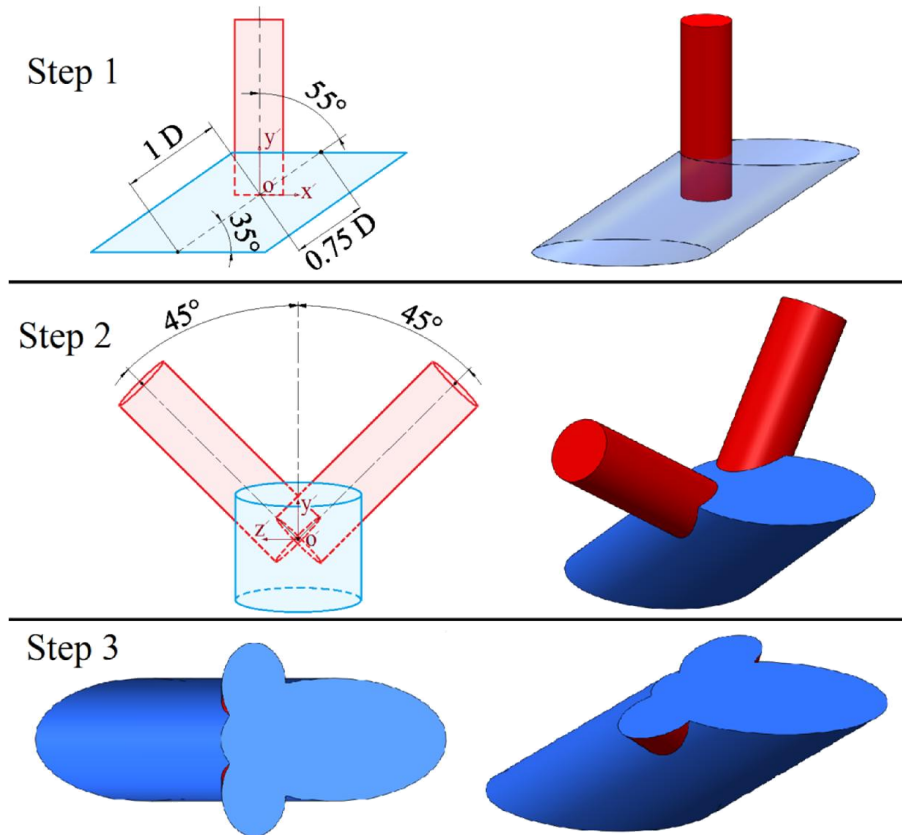


Figure 6.4: Design concept of upstream sister shaped single-hole (upstream SSSH)

Finally, for the up/downstream sister shaped single-hole both steps 1 and 2 for the upstream and downstream SSSH have to be taken into consideration. The final up/downstream SSSH will be formed by merging the primary hole with the downstream and upstream sister holes together and cutting the resultant geometry with the plate's surface plane, as illustrated in Figure 6.5.

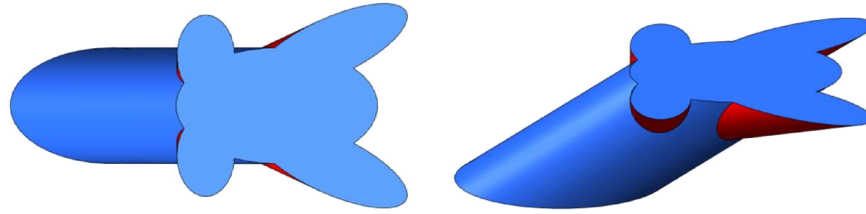


Figure 6.5: Up/downstream sister shaped single-hole (Up/Downstream SSSH)

6.2. COMPUTATIONAL OVERVIEW AND DOMAIN

Simulations are performed at four different blowing ratios; wherein the low blowing ratios involve $M = 0.25$ and 0.5 , while the high blowing ratios involve $M = 1$ and 1.5 . Accordingly, variation of the inlet coolant air velocity can meet the blowing ratios requirement with the constant uniform freestream inlet velocity of $V_\infty = 20$ m/s. The turbulence intensity (Tu) of 0.2% is prescribed at the freestream inlet as stated by Sinha et al. [8], while the value $Tu = 2\%$ is set at the plenum inlet according to Azzi and Lakehal [80]. The viscosity ratios of $\mu_t/\mu = 30$ and 50 are specified at the plenum and freestream inlets, respectively. The boundary conditions applied to the prescribed computational domain are depicted in Figure 6.6.

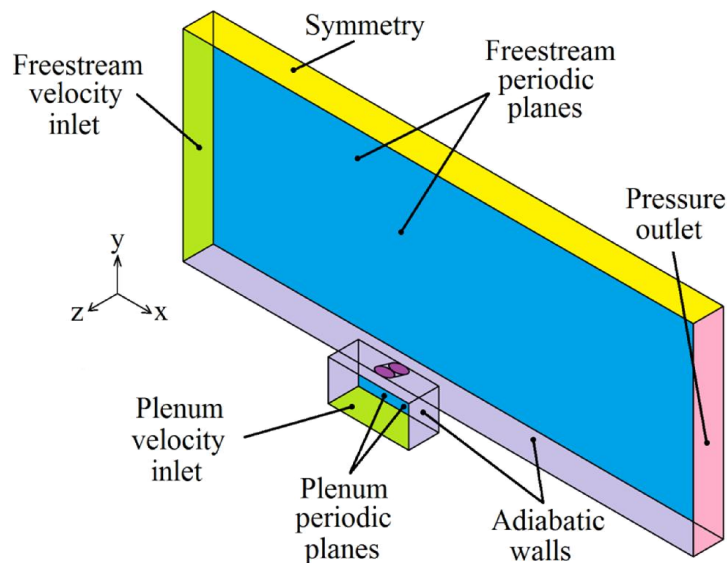


Figure 6.6: Computational domain and boundary conditions

The inlet coolant air velocity can be simply calculated using the continuity equation. The plenum inlet velocity at low and high blowing ratios can be found in Table 6.1.

Table 6.1: Plenum inlet velocity

Blowing Ratio (M)	0.25	0.5	1	1.5
Coolant air velocity [m/s]	0.136	0.273	0.545	0.818

The simulations were performed using ANSYS FLUENT 14.0.0. The solution of Reynolds-Averaged Navier-Stokes equations is obtained by using the finite volume method for discretization of the continuity, momentum and energy equations. The realizable k - ϵ turbulence model combined with the standard wall function is used to model the flow field. The outperformance of the realizable k - ϵ model with the standard wall function compared to other RANS-based models such as the standard and RNG k - ϵ and the Reynolds-stress models has been shown in Chapter 4 (Section 4.3.1). The second order upwind solution scheme is used to solve the momentum, energy and turbulence model equations. The SIMPLEC algorithm is employed to solve the pressure-velocity coupling. The flow is considered as incompressible ideal gas. The simulations are terminated when the normalized residuals reach 10^{-5} for all variables and 10^{-7} is considered for the energy equation.

As shown in Chapter 4, the predicted centerline and laterally averaged film cooling effectiveness results are obtained directly using Equations (4.3) and (4.4), respectively.

The same grid sensitivity test as presented in Chapter 5 is used to obtain the results herein; wherein the grid independent solution is achieved by using 1,200,000 hexahedral cells, as shown in Figure 5.3.

6.3. RESULTS

The following sections provide the results for low and high blowing ratios. Wherein the low blowing ratios cover $M = 0.25$ and 0.5 , while the high blowing ratios cover $M = 1$ and 1.5 . The first section presents a detailed discussion on the results of the film cooling effectiveness. In this section, the centerline and laterally averaged film cooling effectiveness as well as the effectiveness contours over the plate's surface are presented. In the second section, the associated flow structure is analyzed at two different locations downstream of the injection hole. Finally, effects of the exit hole shape and the blowing ratio on the distribution of the flow variables at the jet exit plane are investigated.

6.3.1. Film Cooling Effectiveness

The predicted centerline and laterally averaged film cooling effectiveness for the new sister shaped single-holes (SSSH) including downstream, upstream and up/downstream SSSH are compared to the cylindrical and 15° forward diffused shaped holes (shaped hole), as shown in Figure 6.7 and Figure 6.8, respectively. Results are presented for four different blowing ratios of $M = 0.25, 0.5, 1$ and 1.5 . Note that the density ratio of 1.2 is used here for the subsequent simulations. It should be mentioned here that the sister shaped single-hole film cooling is a new concept; therefore, to the best of the author's knowledge, there is no experimental data available in the open literature.

In general, the variations in the centerline film cooling effectiveness values are not considerable and all schemes provide similar results at $M = 0.25$, as depicted in Figure 6.7(a). This may be attributed to the low blowing ratio of 0.25, where the coolant air flow remains attached to the plate's surface. At this low blowing ratio, different hole schemes do not provide a significant effect on the flow exiting from the hole due to the low value of momentum of the jet close to centerline. Note that the forward diffused shaped hole outperforms other schemes in the region close to the injection hole ($x/D < 10$); while the up/downstream SSSH scheme provides the lowest values for the centerline film cooling effectiveness in that region.

By increasing the blowing ratio to $M = 0.5$, other schemes outperform the cylindrical hole in terms of the centerline film cooling effectiveness, as depicted in Figure 6.7(b). The upstream SSSH provided similar results to that of the shaped hole in the downstream region of $x/D > 5$; wherein the higher film cooling effectiveness values are obtained for the shaped hole in the vicinity of the jet ($x/D < 5$). On the other hand, the highest centerline film cooling effectiveness values at $M = 0.5$ are obtained through the downstream and up/downstream SSSH schemes. The downstream SSSH provides 41% increase in centerline film cooling effectiveness as compared to the cylindrical hole. These increases in the centerline film cooling effectiveness can attribute to the success of the downstream and up/downstream shaped holes in providing more attached coolant to the surface. This might be a result of the reduction in the strength of the CRVP, which will be discussed in Section 6.3.2.

As demonstrated in Figure 6.7(c and d), the forward diffused shaped hole provided similar film cooling effectiveness values to that of the cylindrical hole at the high blowing ratios, except for the closed region to the injection hole ($x/D < 3$). The reattachment of the cooling jet

causes a rise in the centerline film cooling effectiveness for the upstream SSSH in the far downstream region followed by a sudden decrease in the vicinity of the injecting hole, which is due to the jet lift-off. While the highest centerline film cooling effectiveness values in the very far downstream region of $x/D > 15$ is obtained by the upstream SSSH. Overall, the upstream SSSH provides 70% and 85% increase in centerline film cooling effectiveness as compared to the forward diffused shaped hole and the cylindrical hole, respectively.

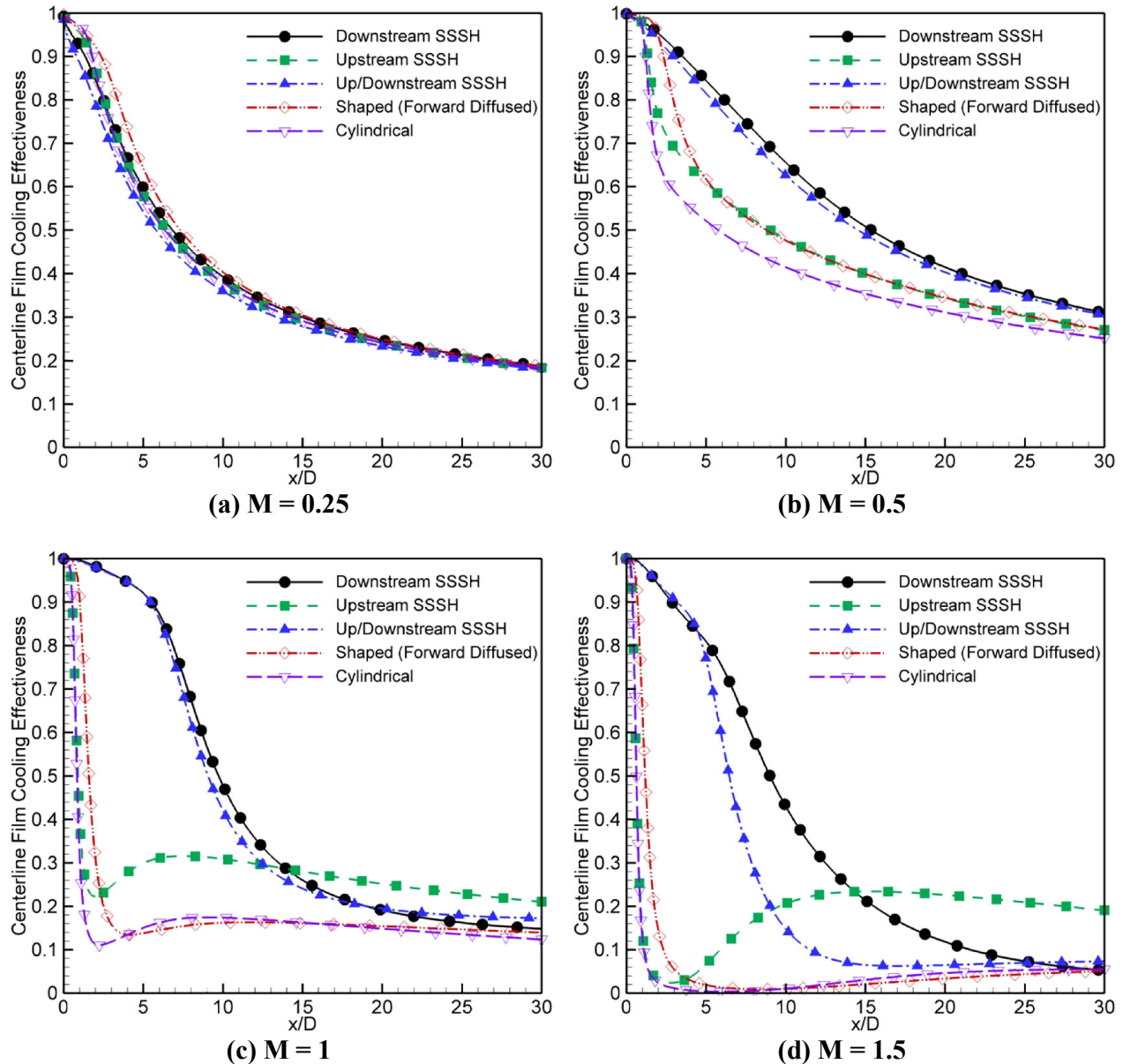


Figure 6.7: Centerline film cooling effectiveness

The laterally averaged film cooling effectiveness results for the low and high blowing ratios are shown in Figure 6.8.

As mentioned before, the effect of various hole configurations on the centerline film cooling effectiveness was almost negligible at $M = 0.25$. However, the increase in the predicted laterally averaged film cooling effectiveness results for the downstream and up/downstream SSSH demonstrates the better spanwise coverage of the cooling jet compared to other configurations at the very low blowing ratio of 0.25, as shown in Figure 6.8(a).

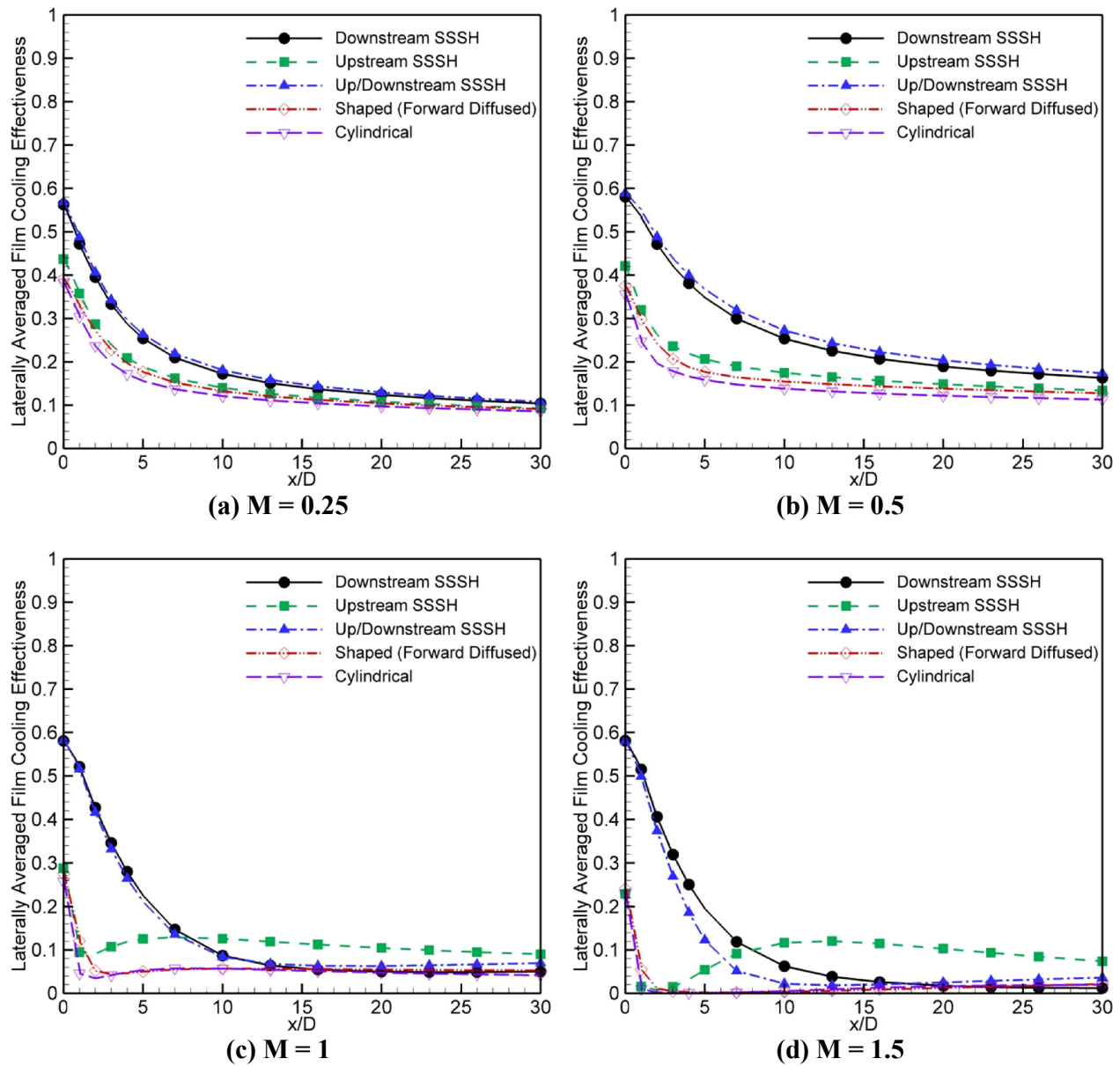


Figure 6.8: Laterally averaged film cooling effectiveness

As illustrated in Figure 6.8(b), similar trend of results also can be seen for the low blowing ratio of 0.5. Wherein, the laterally averaged film cooling effectiveness is increased by approximately 5.5% for the shaped (forward diffused) scheme and around 18% for the upstream SSSH, in comparison with the cylindrical hole scheme. The downstream and up/downstream SSSH schemes provide an increase of around 65% compared to that of the cylindrical hole.

The privilege of the downstream and up/downstream SSSH schemes at high blowing ratios in terms of the laterally averaged film cooling effectiveness results becomes evident when very poor results are obtained for to shaped and cylindrical holes in the region of $x/D < 13$, as demonstrated in Figure 6.8(c and d). For example, the laterally averaged film cooling effectiveness for the downstream SSSH configuration shows an overall improvement of approximately three and four times more on average in that region as compared to the forward diffused shaped hole for the blowing ratios of 1 and 1.5, respectively. It is worth mentioning that although the performance of the upstream SSSH is not considerable in the near-hole region at high blowing ratios, it outperforms other cases in the farther downstream region.

Figure 6.9 depicts a two-dimensional distribution of the local film cooling effectiveness on the plate's surface for three types of the sister shaped single-holes (SSSH), forward diffused shaped and cylindrical hole at blowing ratios of 0.25, 0.5, 1 and 1.5.

The high film cooling effectiveness zone for upstream SSSH is almost similar to the shaped and cylindrical holes at the low blowing ratios of 0.25 and 0.5. However, the moderate range of film cooling effectiveness is kept constant in the far downstream region, that provided a plateau for the laterally averaged film cooling effectiveness at $M = 1$, as shown in Figure 6.8(c). This is due to the diffuser shape of the upstream SSSH hole that causes a decrease in the jet momentum rather than the effect of anti-vortices. It will be shown in Figure 6.10 and Figure 6.11 that the upstream SSSH has similar flow structure to that of the single and forward diffused shaped hole close to the injection hole. The coolant is also completely detached from the wall surface after the region very close to the injecting hole at $M = 1.5$ and it is attached to the surface farther downstream. Note that the lower lateral spreading of the coolant for the upstream SSSH is expected, since its upstream sister-shaped parts are not as wide as the downstream SSSH due to design limitations. Because further spread of the sister holes for the upstream SSSH design (i.e., more than 45° , as shown in Figure 6.4) makes them branch-out from the primary hole.

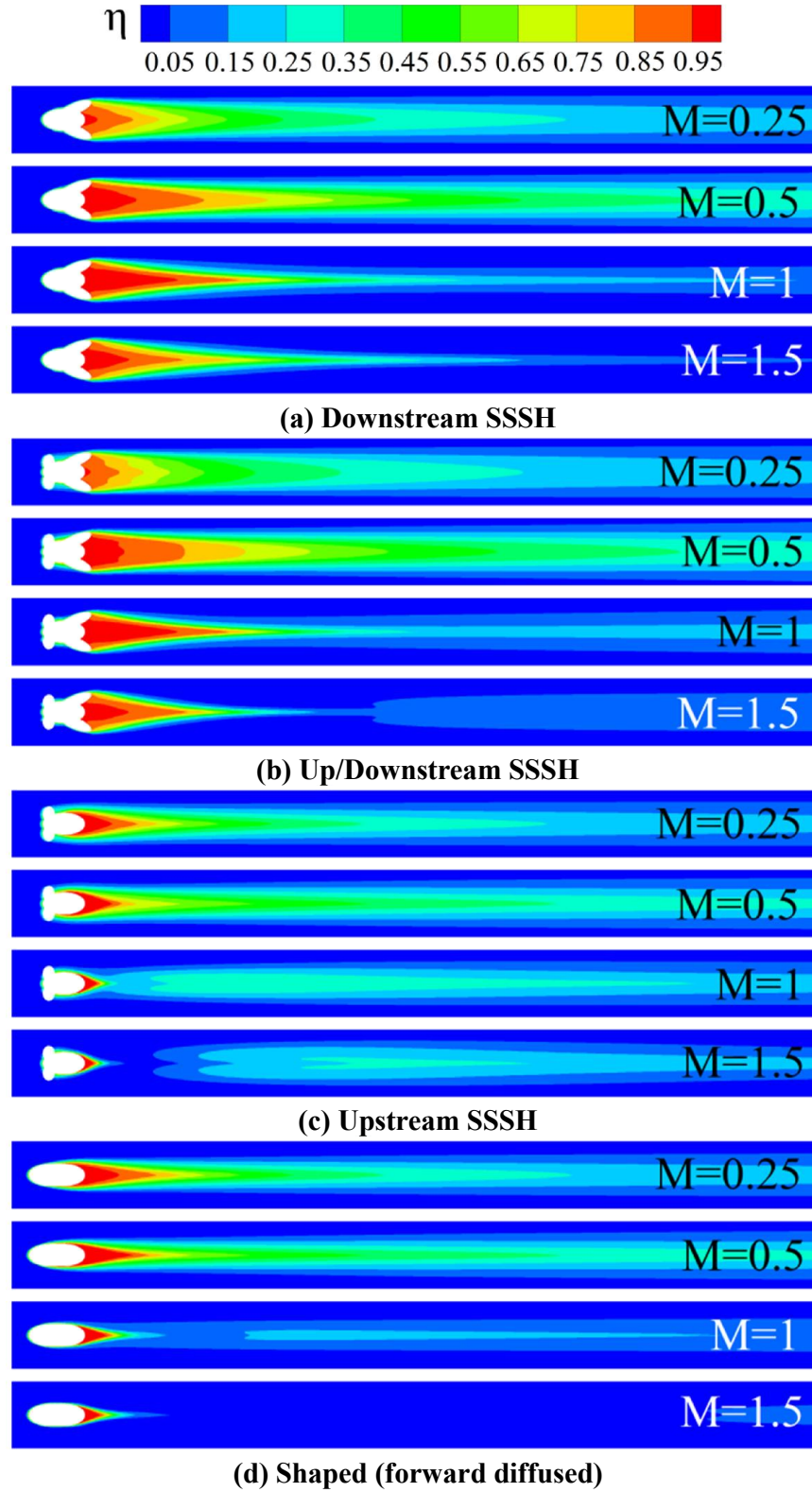
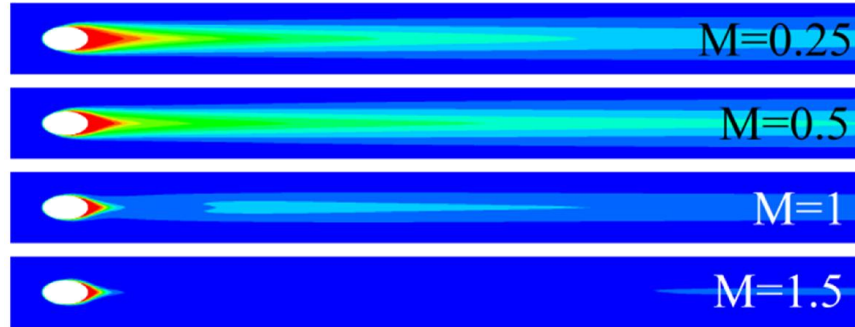


Figure 6.9: Local film cooling effectiveness for different blowing ratios



(e) Cylindrical

Figure 6.9 (cont.): Local film cooling effectiveness for different blowing ratios

As discussed before, the downstream and up/downstream SSSH schemes perform almost equally in terms of the film cooling effectiveness. Note that the downstream SSSH has a less complex design process than the up/downstream SSSH scheme. The coolant is spread better in the lateral direction for these two schemes than other cases at low blowing ratios of 0.25 and 0.5, as displayed in Figure 6.9(a and b). One reason for this is due to the expansion of the downstream sister-shaped parts in the spanwise direction. More importantly, the anti-vortices generated from the downstream sister-shaped parts play a vital role in decreasing the undesired effect of the CRVP generated from the main hole part which will be discussed in the following section. The zone of high film cooling effectiveness for the downstream and up/downstream SSSH schemes at the high blowing ratios is not limited to the very close region of the injection hole in comparison with the shaped and cylindrical holes and it continues to the farther downstream regions. Wherein, there is almost no coverage of the cooling jet on the plate's surface after the vicinity of the injection hole for the shaped and cylindrical holes at $M = 1.5$.

6.3.2. Flow Structure

Flow structures and vortices play a vital role in film cooling performance. Therefore, visualization of the flow field through the aid of velocity vectors and temperature contours is necessary to have a better understanding of the film cooling effectiveness results, which have already been discussed. Many researchers have reported that the counter rotating vortex pairs (CRVP) have a predominant effect on film cooling performance. These vortices are known as the main factor for the jet lift-off effect. Herein, the secondary flow with the aid of the velocity vectors combined with the temperature contours are depicted in the planes perpendicular to the

plate's surface (yz plane) at different downstream locations from the trailing edge of the primary hole. The performance of the discussed film hole geometries according to the general trend of film cooling effectiveness results for the low blowing ratios of $M = 0.25$ and 0.5 were almost similar as well as for the high blowing ratio range ($M = 1$ and 1.5). Therefore, the blowing ratios of 0.5 and 1.5 are chosen for the subsequent analysis to represent the high and low blowing ratios, respectively.

Comparisons of the flow structure between the proposed SSSH schemes at $x/D = 1$ and 5 for the blowing ratios of $M = 0.5$ and 1.5 is presented in Figure 6.10 and Figure 6.11, respectively. The obtained flow structures have also been compared with the results from the forward diffused shaped hole and the cylindrical hole.

The CRVP strength is directly affected by the blowing ratio, where the lower jet lift-off effect is expected at the low blowing ratio of 0.5 than $M = 1.5$. As depicted in Figure 6.10 for $M = 0.5$, it can be seen that the coolant is still attached to the wall surface for all hole configurations at $x/D = 1$ and 5 . In the film cooling effectiveness section, it is found that that the upstream SSSH scheme generally performs similar to the shaped and cylindrical hole at low blowing ratios. This can also be verified herein in terms of its flow structure, as shown in Figure 6.10.

The up/downstream SSSH has the maximum jet exit area at the plate's surface which is attributed to the greater reduction in momentum of the cooling flow at the jet exit plane compared to other cases. Therefore, the coolant height is considerably decreased for the up/downstream SSSH at both locations of $x/D = 1$ and 5 in comparison with other cases. Hence, the coolant jet shows minimum penetration into the freestream flow and provides more attached coolant to the plate's surface for the blowing ratio of 0.5 .

The effect of CRVP vortices becomes prominent in the farther downstream region ($x/D = 5$) and the mixing rate increases between the cold and hot flows; as a result, the hot freestream flow is pushed underneath the cold jet. Note that the lateral location of the CRVP for the upstream SSSH, shaped and cylindrical hole is changed from $z/D \approx \pm 0.4$ to a farther location of $z/D \approx \pm 0.6$ for the downstream and up/downstream SSSH. Visibly, the main difference between the downstream and up/downstream SSSH schemes with other cases is in the lateral spreading of the coolant in the z direction.

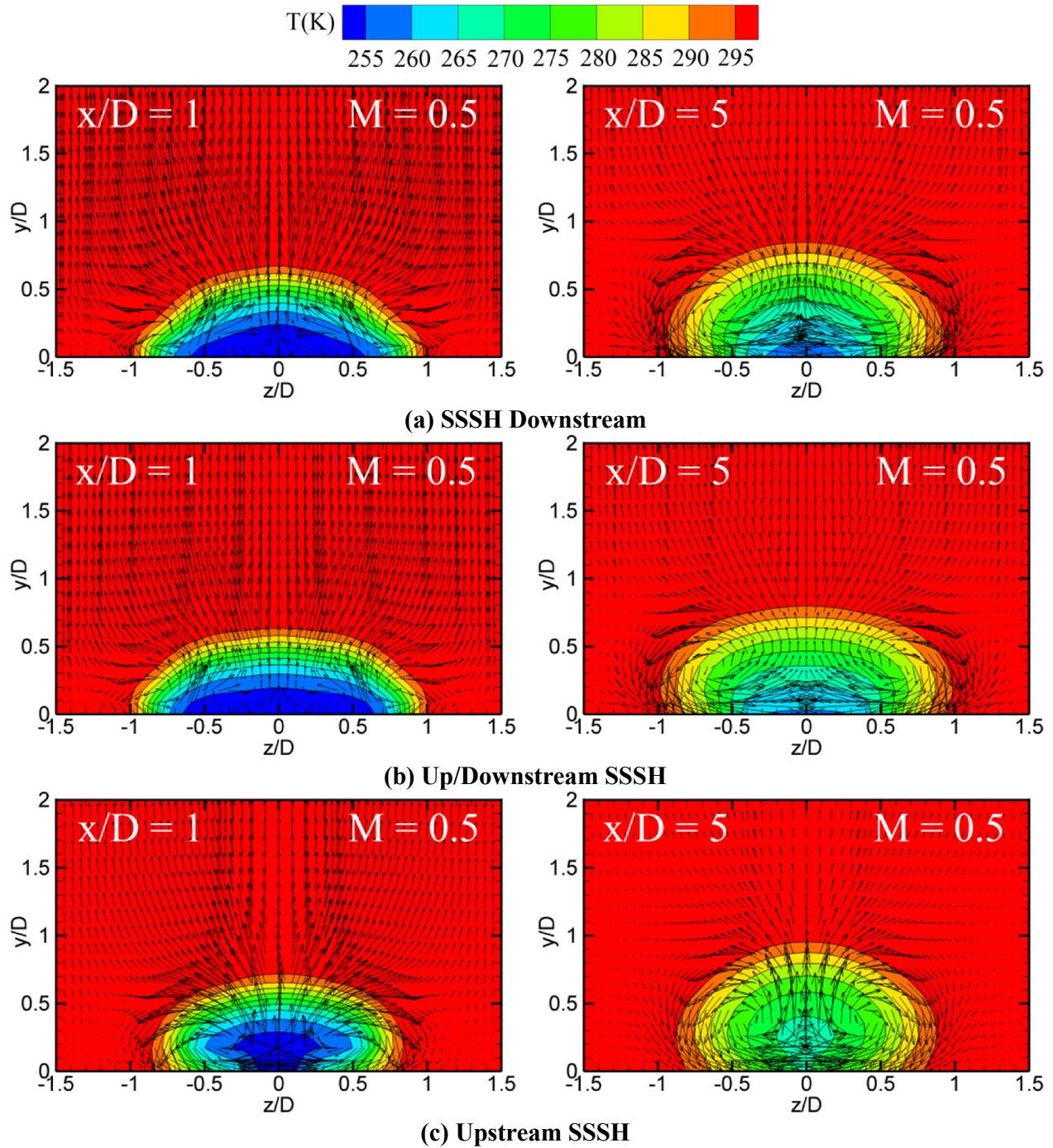


Figure 6.10: Temperature contours and velocity vectors at $x/D = 1$ and 5 for $M = 0.5$

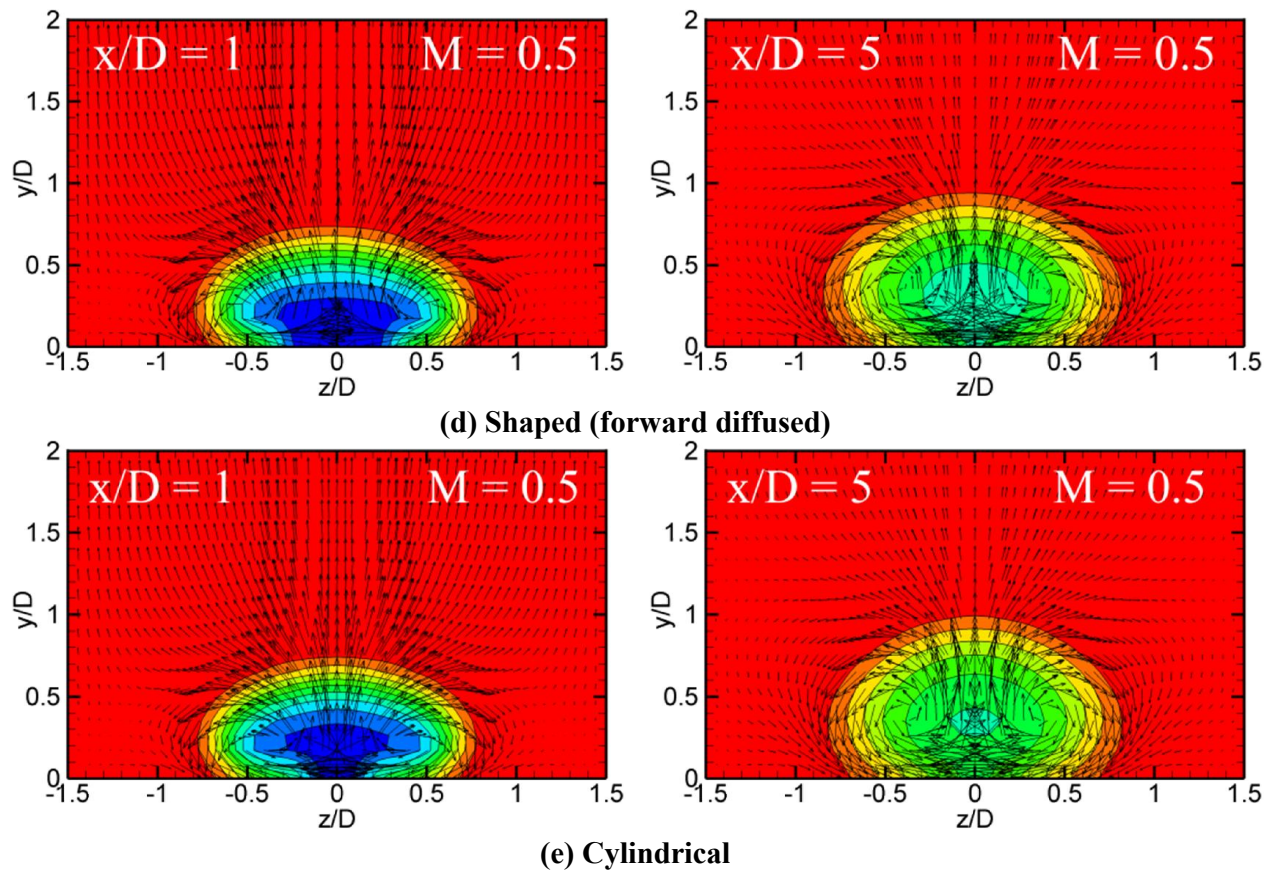


Figure 6.10 (cont.): Temperature contours and velocity vectors at $x/D = 1$ and 5 for $M = 0.5$

For the high blowing ratio of $M = 1.5$ at $x/D = 1$, the coolant core is almost detached from the plate's surface for the shaped, cylindrical and upstream SSSH holes, except for the downstream and up/downstream SSSH schemes where the cold flow is still attached to the wall, as illustrated in Figure 6.11. The footprint of counter rotating vortices (CRVP) is more easily recognized for the blowing ratio of 1.5 for the cylindrical and forward diffused shaped holes. A reason to have more attached and laterally well-spread coolant for the downstream and up/downstream SSSH schemes is because of the vortices generated from the downstream sister-shaped part of these holes which are countering the CRVP vortices. It is worth mentioning that the strength of the CRVP for the up/downstream SSSH is greater than that from the downstream SSSH. Consequently, the cooling jet is more lifted-off from the surface, particularly at $x/D = 5$, and undesirably expanded in the spanwise direction, where it provides less amount of coolant on the wall surface.

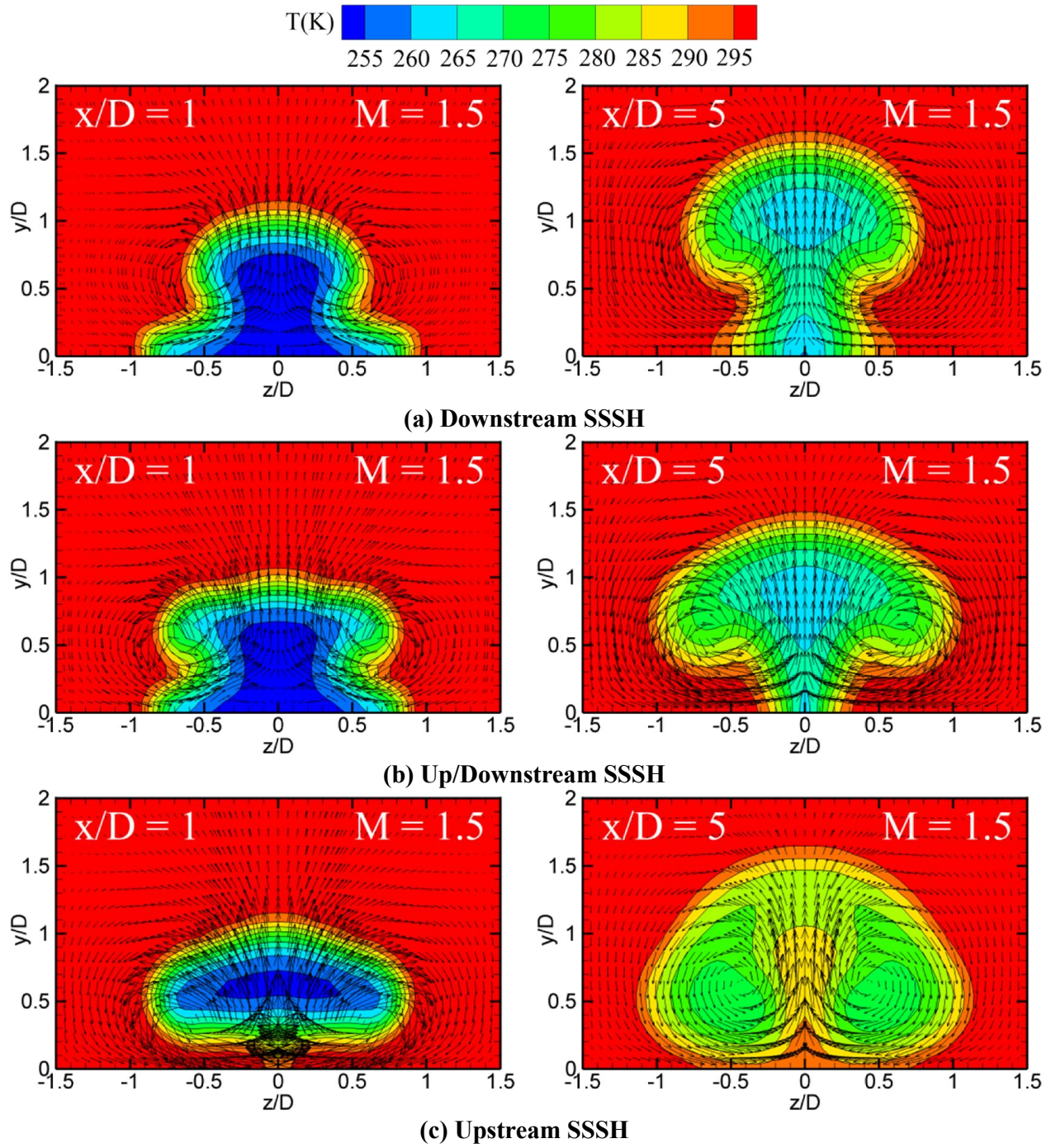


Figure 6.11: Temperature contours and velocity vectors at $x/D = 1$ and 5 for $M = 1.5$

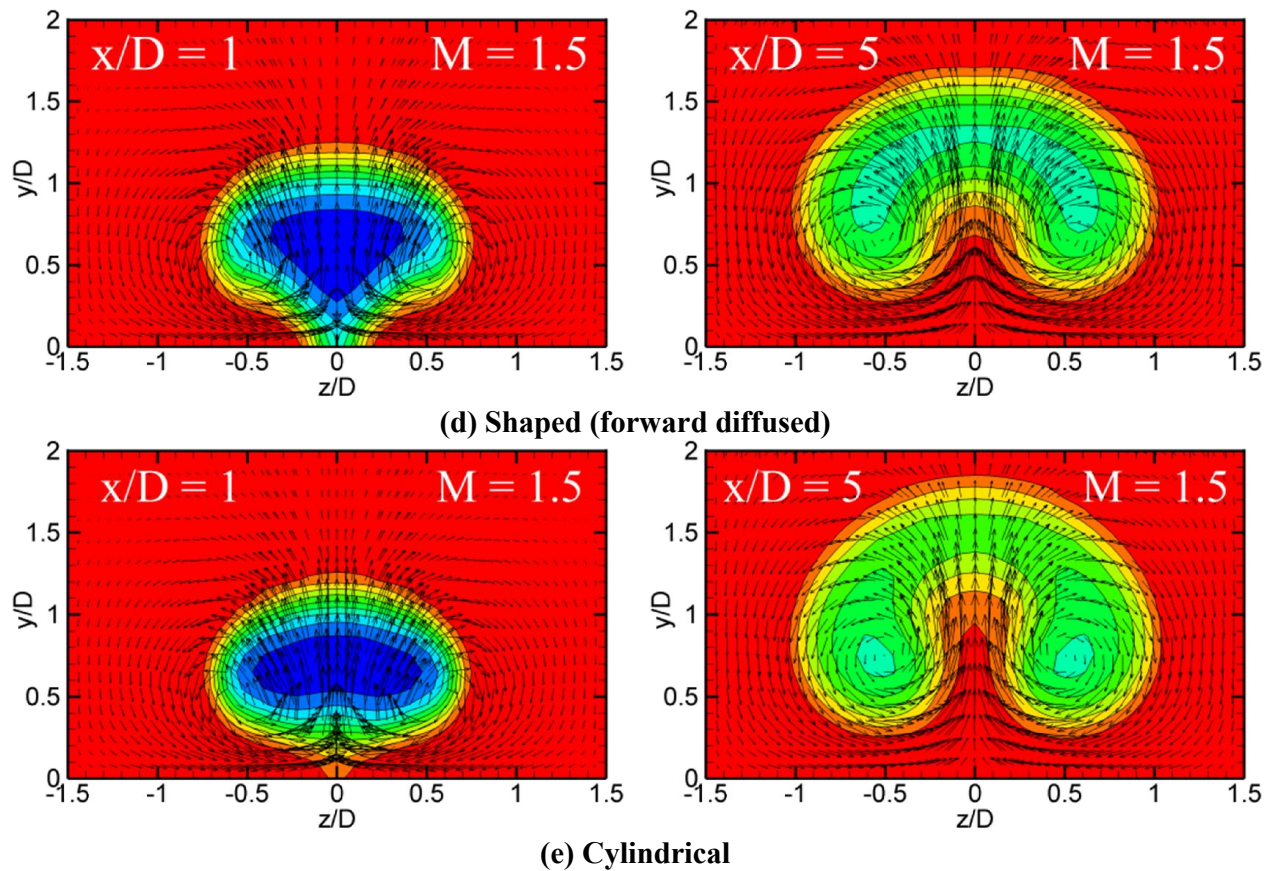


Figure 6.11 (cont.): Temperature contours and velocity vectors at $x/D = 1$ and 5 for $M = 1.5$

On the other hand, the upstream SSSH geometry cannot take advantage of this anti-vortex system as much as the downstream and up/downstream schemes; therefore, the CRVP vortices remain strong. A similar trend can be followed for the location of $x/D = 5$, where it is observed that the coolant core is still attached to the surface for the downstream and up/downstream SSSH configurations. Note that for the upstream SSSH, the coolant is reattached to the wall farther downstream of $x/D = 5$ which is caused by the freestream flow that pushes the coolant to the surface.

6.3.3. Effect of the Exit Hole Shape

The velocity magnitude contours in the jet exit plane for blowing ratios of 0.5 and 1.5 are shown in Figure 6.12.

Walters and Leylek [21] have pointed out that the distribution of the flow variables at the jet exit plane depends on different factors such as the blowing ratio, density ratio and geometry. In the present study, the blowing ratio and the hole geometry varies for different hole shapes.

As depicted in Figure 6.12(e), the high momentum region is placed more towards the downstream region of the hole (TE) for the cylindrical hole at the low blowing ratio of 0.5, while it moves to the upstream side of the hole (LE) by increasing the blowing ratio to 1.5. This is also true for the upstream SSSH scheme, as shown in Figure 6.12(c). However, for the downstream, up/downstream SSSH and the forward diffused shaped holes, the region with high velocity magnitude is located more towards the center and upstream side of the shaped holes for both blowing ratios.

It should be noticed here that for the up/downstream and upstream SSSH inside the sister-shaped hole parts in the upstream region (close to the LE), the velocity magnitude is comparatively less than in other regions of the holes. This shows that a small volume of coolant passes through this region; hence, it cannot participate efficiently in generating the anti-vortex structures to defeat the CRVP (as compared with the upstream discrete sister holes) and it could also have detrimental effects on the uniformity of the jet exit flow. Overall, the downstream sister-shaped parts have a dominant effect on the flow exiting from the hole and on countering the CRVP vortices in comparison with the upstream sister-shaped parts. Additionally, the wider area provided for the upstream and up/downstream SSSH schemes in the jet exit plane (downstream side of the hole) decreases the gradient of the flow variables. This can result in providing more uniform flow to exit from the hole.

The interaction of the jet with the mainstream flow has a direct effect on the distribution of the flow variables in the jet exit plane, which will be manifested for the high blowing ratio of 1.5 as compared to $M = 0.5$. As a result of the interaction between the coolant air jet and freestream flow, high and low pressure zones are formed in the upstream (LE) and downstream (TE) regions of the hole at the exit plane, respectively. Ergo, the coolant momentum increases downstream of the hole due to the pressure gradient. However, this argument is valid for the upstream SSSH and cylindrical hole for the low blowing ratio of 0.5. For other cases and/or the blowing ratio of 1.5, the high momentum zone stays mainly towards the upstream side of the hole which can be attributed to the strong effect of the blowing ratio and the film cooling hole geometry on the jet exit conditions.

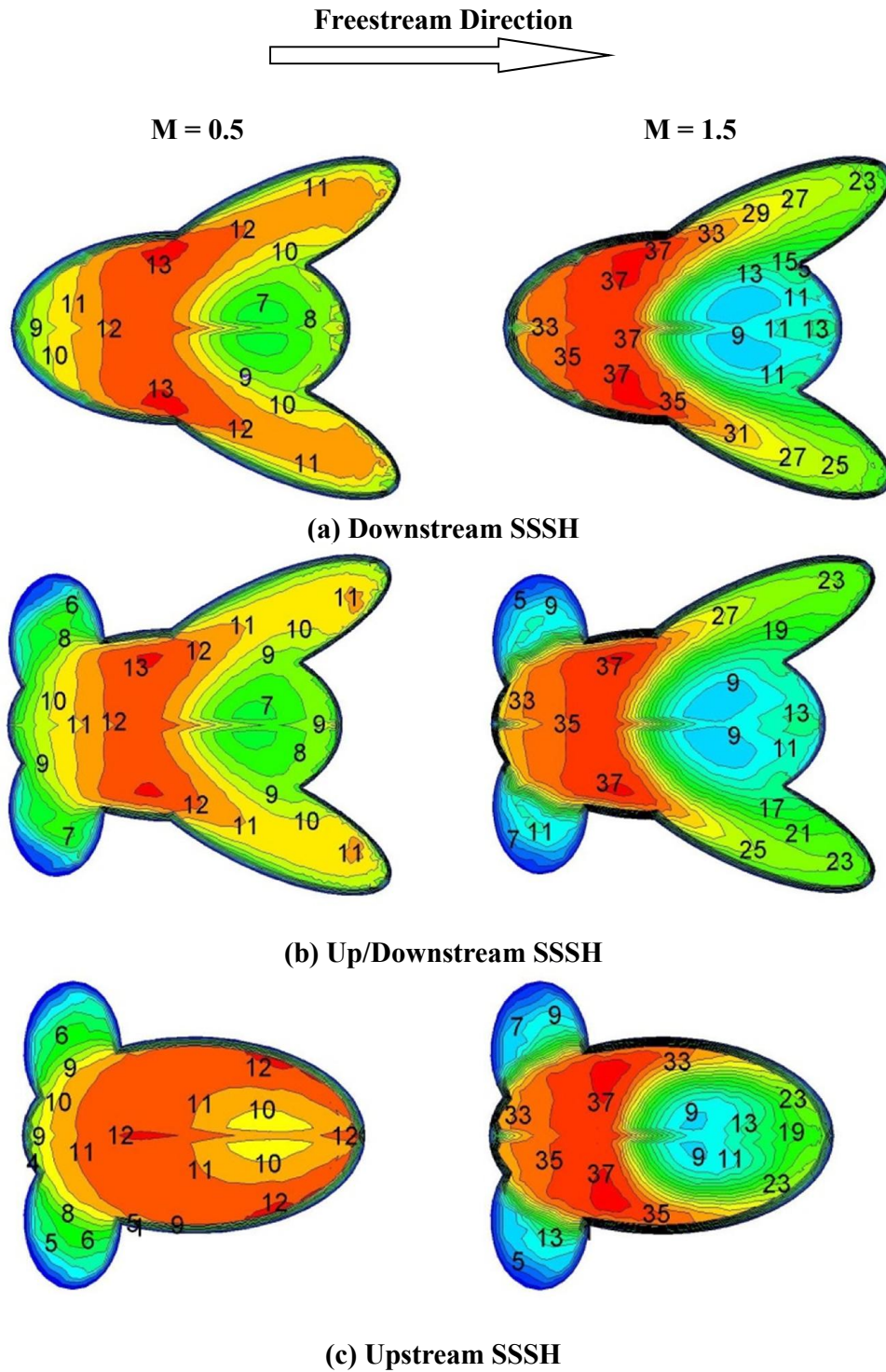


Figure 6.12: Velocity magnitude contours [m/s] in the jet exit plane for M = 0.5 and 1.5 (not drawn to scale)

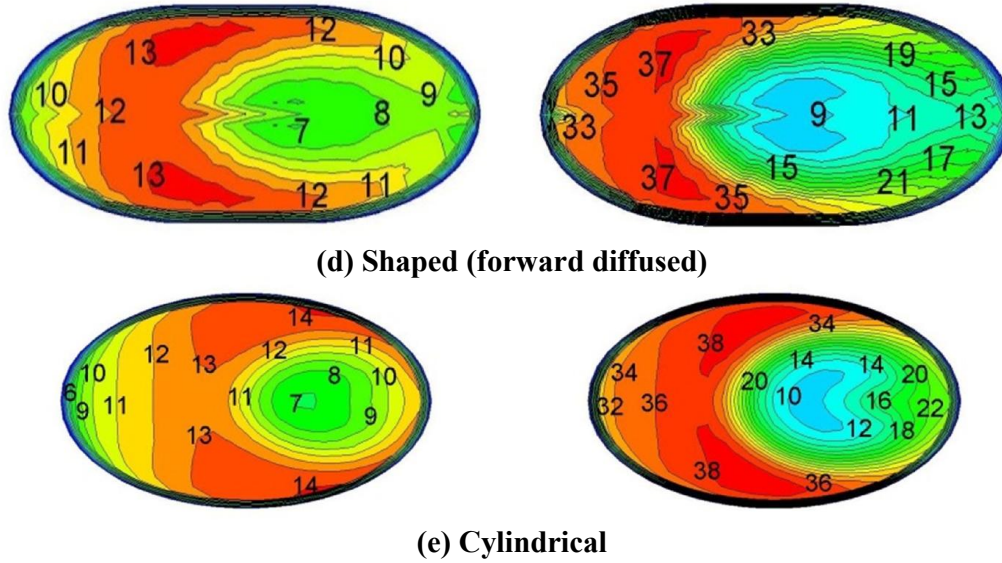


Figure 6.12 (cont.): Velocity magnitude contours [m/s] in the jet exit plane for $M = 0.5$ and 1.5 (not drawn to scale)

6.4. CONCLUSIONS

In the present chapter, three novel film cooling hole schemes, namely downstream, upstream and up/downstream sister shaped single-hole (SSSH) are suggested. Their film cooling performance has been compared with the cylindrical and the forward diffused shaped holes. Simulations are carried out at low blowing ratios of 0.25 and 0.5 and high blowing ratios of 1 and 1.5.

A notable improvement in film cooling performance has been observed for the downstream and up/downstream schemes compared with the cylindrical and forward diffused shaped holes. Wherein more lateral distribution of coolant is obtained and less penetration of coolant into the mainstream flow is observed.

The jet lift-off and the CRVP strength are significantly decreased for the downstream and up/downstream SSSH schemes compared to other cases; as a result, more attached coolant to the plate's surface is observed. In general, the downstream and up/downstream SSSH schemes performed equally in all blowing ratios, wherein the downstream SSSH has a less complex design process than the up/downstream scheme.

For the proposed SSSH geometries, the downstream sister-shaped parts have a dominant effect on the flow exiting from the hole and on countering the CRVP vortices in comparison with

the upstream sister-shaped parts. To clarify, the upstream SSSH provided similar film cooling performance as the forward diffused shaped hole in terms of film cooling effectiveness and downstream vortex structures for the low blowing ratios. However, the upstream SSSH outperforms other cases in the farther downstream region at the high blowing ratios of 1 and 1.5.

7. EVALUATION OF THE SISTER SHAPED SINGLE-HOLE SCHEMES AT THE LEADING EDGE

In this chapter, a numerical evaluation of the performance of the three proposed SSSH schemes (downstream, upstream and up/downstream) on the leading edge of an axial turbine blade cascade with two rows of cooling holes is presented; one row is positioned on the pressure side and the other on the suction side. Simulations are performed at three blowing ratios of 0.7, 1.1 and 1.5. The predicted pressure field is compared to the available experimental data. The obtained film cooling effectiveness results and the thermal field as well as the predicted flow field are compared with the conventional cylindrical hole and a forward diffused shaped hole.

7.1. PROBLEM STATEMENT

The investigated blade's configuration in this chapter corresponds to the AGTB-B1 high pressure turbine cascade. Note that for the AGTB-B1 blade the coolant air is injected in the streamwise direction. The radially inclined injection holes for the AGTB blade are called ABTB-B2. The leading edge film cooling for the AGTB-B1 blade includes two rows of injections holes, one on the pressure side and another row is located on the suction side of the blade.

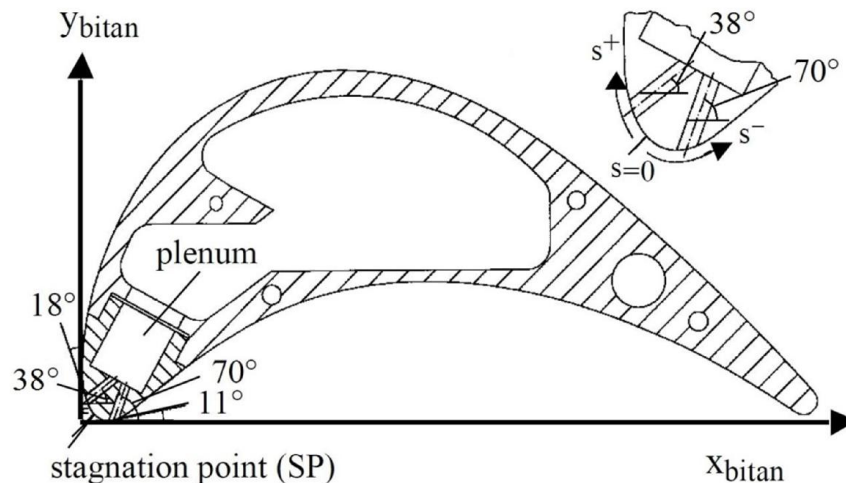


Figure 7.1: Geometry of AGTB-B1 blade [82]

The experimental study of the present cascade blade configuration for the cylindrical hole is carried out by Ardey and Fottner [83, 84] and Ardey [85] in a high speed cascade wind tunnel. The two-dimensional geometry of the investigated blade in a mid-section of the injection holes is depicted in Figure 7.1.

The profile coordinates of the AGTB-B1 blade in a bitangent-system can be found in Appendix B [85]. The geometric data of the cascade as well as the associated flow parameters are given in Table 7.1.

Table 7.1: Cascade geometry and parameters

Chord Length (L_{ch})	250 mm
Vane Height (H_v)	300 mm
Pitch Ratio of Cascade (t'/L_{ch})	0.714
Staggering Angle (β_s)	73.0°
<i>Cascade Aerodynamics</i>	
Inlet Mach Number (Ma_1)	0.37
Inlet Re Number (Re_1)	371,000
Inlet Flow Angle (β_1)	133.0°
Inlet Turbulent Intensity (Tu_1)	5%
Isentropic Exit Mach Number (Ma_{2is})	0.95
Isentropic Exit Re Number (Re_{2is})	695,000
Exit Flow Angle (β_2)	28.3°
<i>AGTB-B1 Cooling Configuration (Holes)</i>	
Position at SS (s/L_{ch}) _{SS}	0.02
Position at PS (s/L_{ch}) _{PS}	-0.03
Streamwise Ejection Angle at SS (γ) _{SS}	110°
Streamwise Ejection Angle at PS (γ) _{PS}	120°
Hole Diameter (D)	3 mm
Hole Length at SS (L_{SS})	12.5 mm (4.17D)
Hole Length at PS (L_{PS})	12.5 mm (4.17D)
Pitch-to-diameter Ratio of Holes (P/D)	5
Number of Holes/Row	20

The schematic of the cascade for the AGTB-B1 blade is illustrated in Figure 7.2.

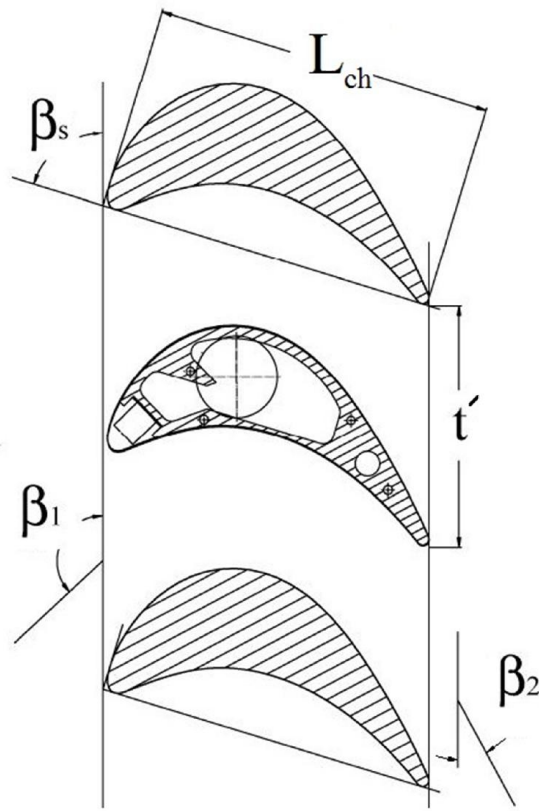


Figure 7.2: Schematic of AGTB-B1 cascade [86]

The close-up of the top and side views of the cylindrical hole and 15° forward diffused shaped hole are shown in Figure 7.3. A numerical evaluation on the performance of the 15° forward diffused shaped hole for the long-hole flat-plate film cooling application ($L/D = 4$) has been carried out in the work of Baheri et al. [87]. Note that the length of the entrance of the cooling pipe before the shaped part was $2.1D$ and the length of the shaped part of the hole was $1.9D$, where the injection angle was set to 35° . Later, Baheri et al. [17] provided a numerical assessment on the performance of the 15° forward diffused shaped hole on the AGTB-B1 blade (same as the present geometry), wherein the length-to-diameter ratio of the injection hole is $4.17D$. Accordingly, the length of the shaped hole in the present simulations is kept at $1.9D$ with the entrance length of $2.27D$ for the design of the 15° forward diffused shaped hole, as depicted in Figure 7.3.

The assumptions for the subsequent design procedures are based on the flat-plate film cooling. Once the design process is completed for the present long-hole film cooling (i.e., $L/D = 4.17$), each designed configuration will be applied on the AGTB-B1 blade. Similar to section 6.1 in the previous chapter, the original Cartesian coordinate system is placed at the trailing (downstream) edge of the jet exit hole (i.e., x, y, z), which is used to address all the simulation results. In order to ease the design process of the sister shaped single-hole, a secondary coordinate system (i.e., x', y', z') is placed after a length of $2.27D$ from the injection pipe entrance at the center of the primary cylindrical part.

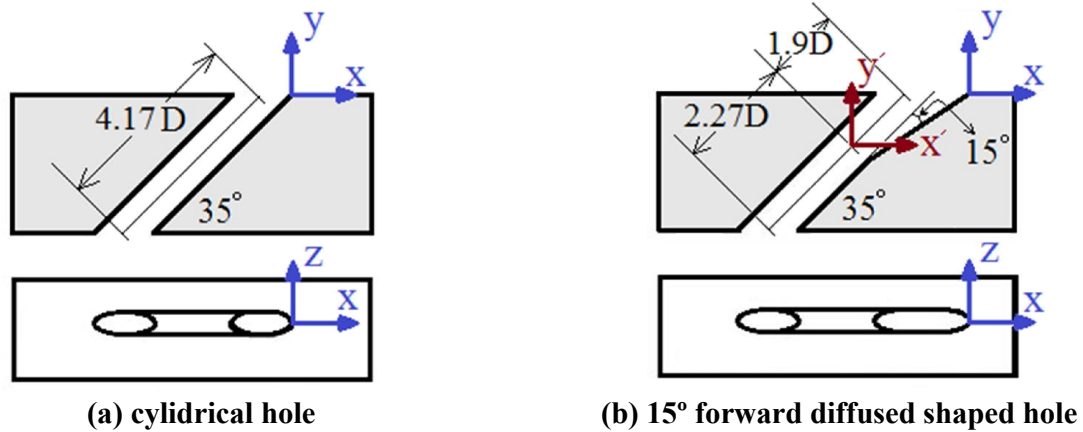


Figure 7.3: Close-up of the side and top view of (a) cylindrical hole and (b) 15° forward diffused shaped hole (not drawn to scale)

To make the sister shaped single-holes schemes applicable to the long-hole film cooling configuration herein ($L/D = 4.17$), similar procedures as in Section 6.1 have to be undertaken with slight modifications which will be explained as follows.

The discrete sister holes should be relocated at the origin of the secondary coordinate system with a specific inclination and rotation with respect to that coordinate system. Finally, the discrete sister holes will be merged to the main hole.

The formation of downstream SSSH scheme is similar to those steps that have already been taken for the short-hole design in Section 6.1 (Figure 6.3). However, small modifications due to the design limitation have to be applied here for the long-hole design, which can be explained in three steps as follows, Step 1: after placing the two downstream discrete sister holes at the origin of the secondary coordinate system position (aligned with the primary hole

inclination of 35°), they are rotated by 15° with respect to the negative direction of the z' axis. Step 2: the downstream sister holes are spread into the spanwise direction by 15° with respect to the y' axis. Note that the lateral spread angle of the sister holes has to be decreased from 25° to 15° in comparison to the design process for the short-hole film cooling ($L/D = 1.75$), as mentioned in Section 6.1. Otherwise, the sister holes will become branched-out from the primary injecting hole and a shaped single hole cannot be formed. Step 3: finally the downstream sister shaped single-hole configuration is formed by merging the primary hole to the rotated discrete sister holes and cutting them at the blade's surface plane, as shown in Figure 7.4.

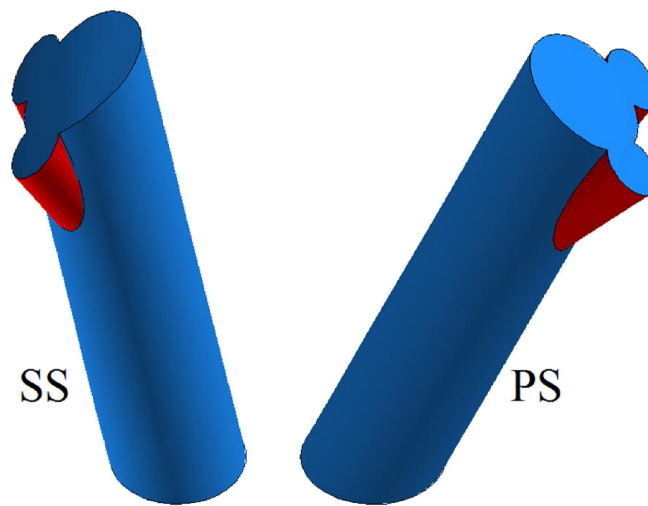


Figure 7.4: Downstream sister shaped single-hole scheme (Downstream SSSH)

Similarly, three steps have to be taken in order to make the upstream SSSH scheme. Note that again some modifications are needed to be applied to the design steps of the upstream SSSH for the shot-hole application which is mentioned in Section 6.1 (Figure 6.4).

Step 1: after placing the two downstream discrete sister holes at the origin of the secondary coordinate system (aligned with the primary hole inclination of 35°), they are rotated by 10° with respect to the positive direction of the z' axis. Step 2: the upstream sister holes are spread into the spanwise direction by 20° with respect to the x' axis. Step 3: the upstream SSSH is formed by merging all holes together and cutting them at the blade's surface plane as demonstrated in Figure 7.5. Once again, it is worth mentioning here that without the mentioned modifications in the rotation angle of the sister holes, it is impossible to produce a single shaped hole.

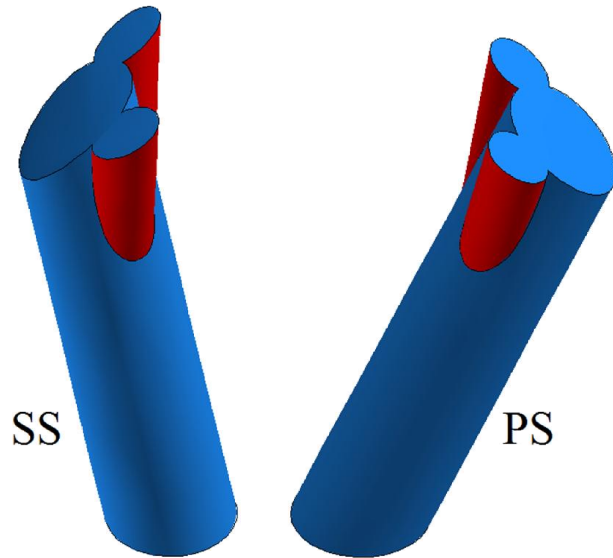


Figure 7.5: Upstream sister shaped single-hole scheme (upstream SSSH)

Finally, for the up/downstream sister shaped single-hole both steps 1 and 2 for the upstream and downstream SSSH have to be taken into consideration. The final up/downstream SSSH will be formed by merging the primary hole with the downstream and upstream sister holes together and cutting the resultant geometry with the blade's surface plane, as illustrated in Figure 7.6.

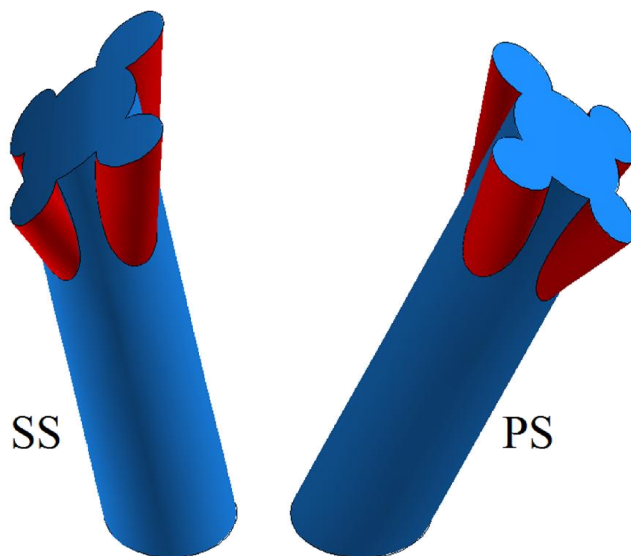


Figure 7.6: Up/downstream sister shaped single-hole scheme (Up/Downstream SSSH)

7.2. COMPUTATIONAL OVERVIEW AND DOMAIN

Simulations of the present cascade blade are carried out according to the experimental work of Ardey [85] for three blowing ratios of 0.7, 1.1 and 1.5, which are listed in Table 7.2. The aerodynamic condition for all blowing ratios is used for the validation of the predicted pressure distribution results over the blade against the available experimental data of Ardey [85]; the temperature ratio ($T_{t,c}/T_{t,1}$) of the coolant to the mainstream flow is kept at 1. The aerothermal analyses for the rest of the presented results are maintained by setting the temperature ratio to 0.5. Note that this temperature ratio represents the ratio of the air temperature at the final compressor stage to the turbine inlet temperature.

Table 7.2: Boundary conditions

<i>Flow Property</i>			
Blowing Ratio (M)	0.7	1.1	1.5
Total Pressure ($P_{t,1}$)	19,620 Pa	19,650 Pa	19,620 Pa
Total Temperature ($T_{t,1}$)	303.15 K	303.15 K	303.15 K
Inlet Flow Angle (β_1)	133.0°	133.0°	133.0°
Static Pressure (P_2)	14,710 Pa	14,640 Pa	14,560 Pa
<i>Cooling Flow Inlet Conditions</i>			
Total Pressure ($P_{t,c}$)	20,060 Pa	21,710 Pa	24,130 Pa
$(T_{t,c}/T_{t,1})_{\text{aerodynamic}}$	1	1	1
$(T_{t,c}/T_{t,1})_{\text{aerothermal}}$	0.5	0.5	0.5

The computational domain including the applied boundary conditions is shown in Figure 7.7. The no-slip condition is specified at adiabatic walls indicating that the velocity components of the flow at walls are zero. The pressure outlet is specified at the outlet boundary where the static pressure of P_2 is prescribed according to experimental values corresponding to its blowing ratio. The pressure inlet boundary allows us to specify the total inlet pressure and total inlet temperature for the freestream and plenum. In addition to the experimental value of the turbulent intensity ($Tu_1 = 5\%$), a turbulent viscosity ratio of $\mu_t/\mu = 100$ is set at the freestream inlet. Lower values for the turbulent intensity ($Tu_c = 1\%$) and turbulent viscosity ratio ($\mu_t/\mu = 10$) are considered at the plenum inlet boundary [88].

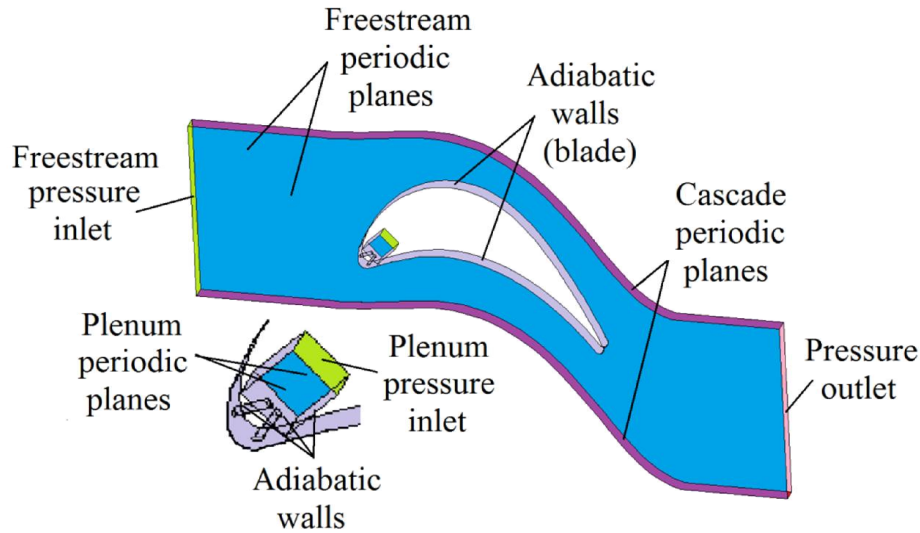


Figure 7.7: Computational domain and boundary conditions

The simulations were performed using ANSYS FLUENT 14.0.0. The solution of compressible Reynolds-Averaged Navier-Stokes equations is obtained by using the finite volume for discretization of the continuity, momentum and energy equations. The realizable $k-\epsilon$ turbulence model combined with the standard wall function is used to model the flow field. The second order upwind solution scheme is used to solve the momentum, energy and turbulence model equations. The SIMPLEC algorithm is employed to solve the pressure-velocity coupling. The simulations are terminated when the normalized residuals reach 10^{-5} for all variables and 10^{-7} is considered for the energy equation.

7.2.1. Computational Grid

The ANSYS GAMBIT 2.4.6 is used to generate a structured multiblock computational grid for the solver. As the standard wall function is employed, the density of the grids in the near-wall region have been carefully set to achieve y^+ values which fall in the range of 30 to 60 [72]. Three different numbers of structured hexahedral cells have been implemented ranging from 284,800 to 868,006 cells. The pressure ratio ($P/P_{t,1}$) distribution over the blade on both the suction side and pressure side is chosen as the monitored parameter. Figure 7.8 shows the predicted pressure distribution over the suction side and pressure side of the blade for the applied grids at blowing ratio of 1.1.

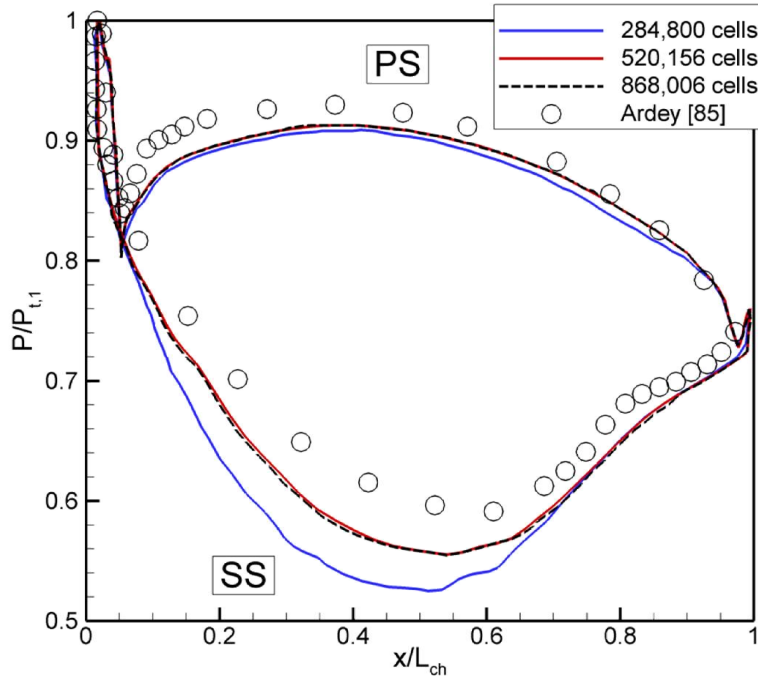
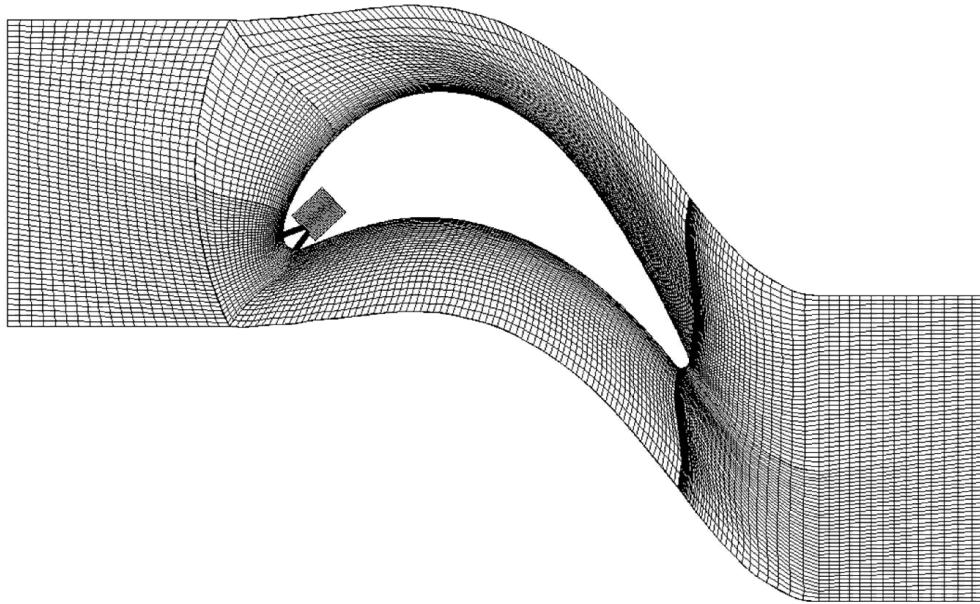


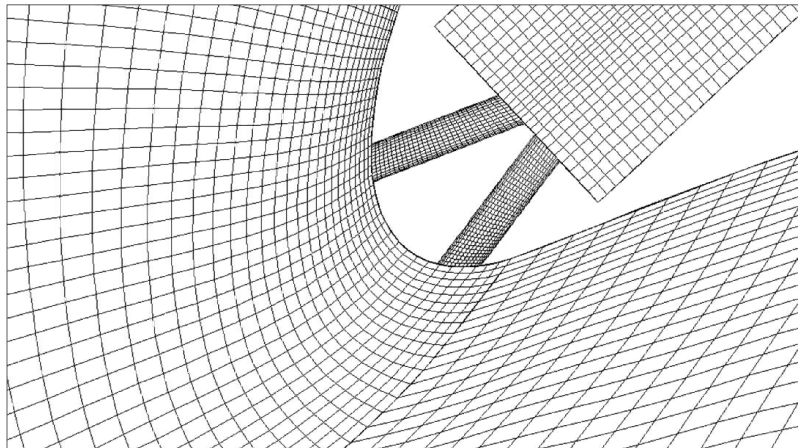
Figure 7.8: The grid sensitivity test ($M = 1.1$)

It can be seen that the coarse mesh including 284,800 cells significantly underpredicts the pressure on the suction side and this number of cells does not provide sufficient accuracy of the simulations. Increasing the number of cells to 520,156 provided better pressure distribution results on the blade compared to the coarse mesh. However, further increase in the number of cells to 868,006 does not result in any significant change in the pressure distribution results as the monitored parameter. Hence, the grid number with 520,156 cells is chosen as the grid independent solution for subsequent simulations.

The computational grid for the medium grid size (520,156 cells) is shown in Figure 7.9.



(a) Side view of the whole domain



(b) Close-up of the leading edge region

Figure 7.9: Computational grid

7.3. RESULTS

The following sub-sections provide the results for three blowing ratios of $M = 0.7$, 1.1 and 1.5 at the leading edge of the blade. First, the predicted pressure distributions on the blade will be validated against the experimental data and numerical results available in the literature. The second section presents a detailed discussion on the results of the centerline and laterally averaged film cooling effectiveness. Next, more investigation in the thermal field is carried out

through the temperature contours. Finally, the velocity plot distributions are analysed at the mid-span plane.

7.3.1. Validation

The predicted static pressure distributions on the blade's surface at mid-span (a plane across the center of the injection holes along the blade) under the aerodynamic condition for the cylindrical hole are presented in Figure 7.10. The obtained results are compared with the available experimental data of Ardey [85] for three blowing ratios of $M = 0.7$, 1.1 and 1.5 . Furthermore, a comparison of the present predicted results against the numerical simulation of Baheri et al. [17] is shown at the blowing ratio of $M = 1.1$.

In general, the comparisons of the predicted pressure distributions are satisfactory on both the suction side and the pressure side. Nevertheless, an underprediction of the predicted results can be observed in the front part of the turbine blade for all blowing ratios.

Moreover, the advantage of the present applied realizable $k-\epsilon$ model combined with the standard wall function can be seen when compared to that of Baheri et al. [17] where the standard $k-\epsilon$ model with standard wall function has been implemented, as shown in Figure 7.10(a). In comparison, the under prediction of the pressure distribution on the suction side with the realizable $k-\epsilon$ model is significantly decreased than the one using the standard $k-\epsilon$ model.

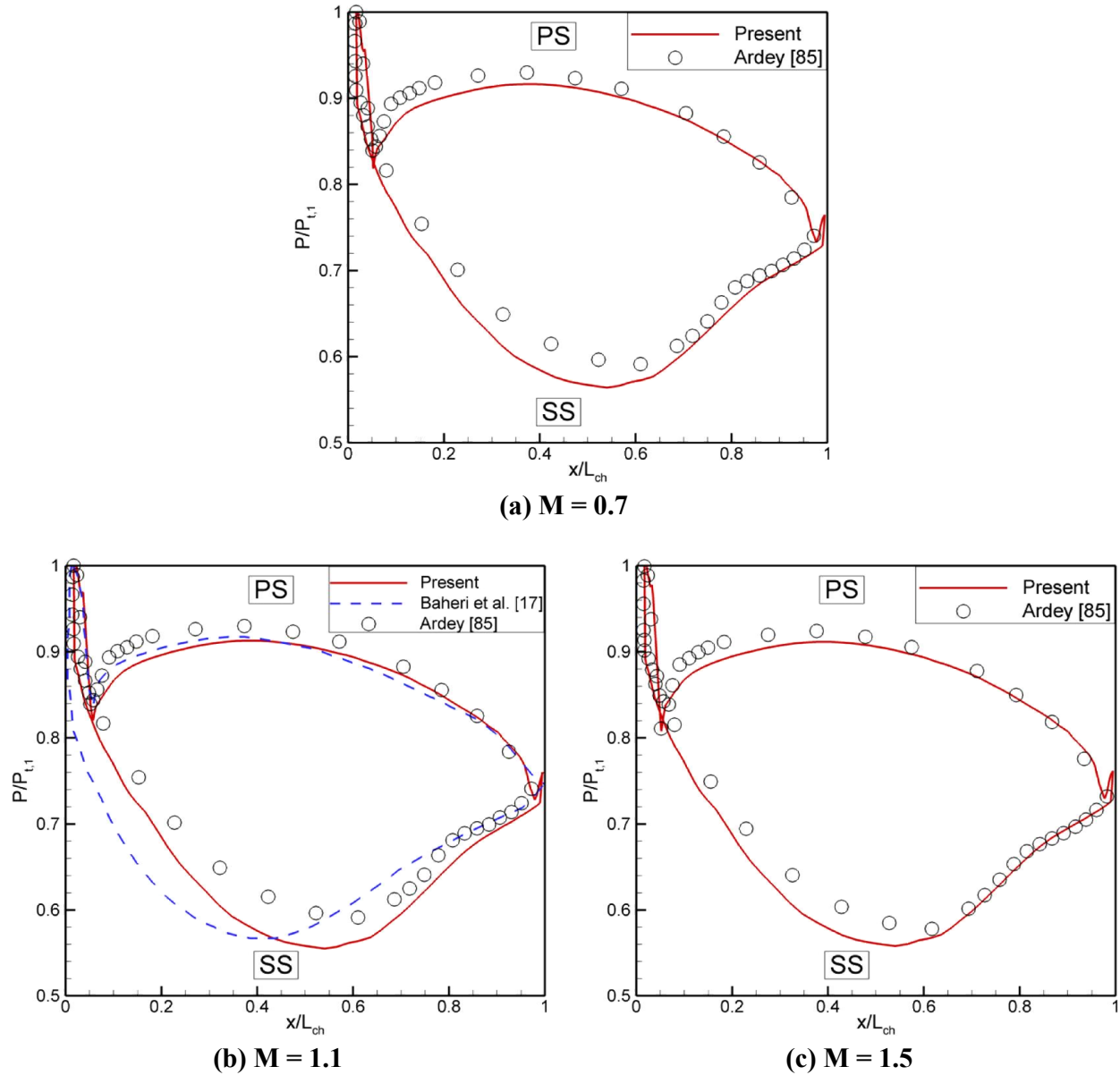


Figure 7.10: Static pressure distribution on blade's surface at mid-span plane

7.3.2. Film Cooling Effectiveness

The predicted centerline and laterally averaged film cooling effectiveness for the sister shaped single-holes (SSSH) including downstream, upstream and up/downstream SSSH are compared to the cylindrical and 15° forward diffused shaped holes (shaped hole), as shown in Figure 7.11 and Figure 7.12, respectively. Results are presented for three different blowing ratios of $M = 0.7, 1.1, 1.5$ at the leading edge of the blade for both the pressure side and the suction side.

The difference between the predicted centerline film cooling effectiveness for all configurations is not considerable on the pressure side at the blowing ratio of 0.7, as shown in Figure 7.11(a). On the other hand, the difference between the resultant centerline film cooling effectiveness values for various configurations increases on the suction side. This may be a result of the lower pressure on the suction side which allows for the exiting of higher volume of coolant from the holes on the suction side as compared to the pressure side. Moreover, the momentum of the exiting jet at the blowing ratio of 0.7 does not seem to be sufficiently high enough to defeat the mainstream flow on the pressure side, which will be discussed in Section 7.3.4. It can be seen that the downstream SSSH provides the highest centerline film cooling effectiveness values compared to other hole geometries on the suction side. It also shows an increase of about 28% on average in comparison to the cylindrical hole. In general, the predicted centerline film cooling effectiveness with the up/downstream SSSH is almost disappointing for $M = 0.7$ at the leading edge compared to other SSSH schemes.

The general trend of the centerline film cooling effectiveness results for the higher blowing ratios of 1.1 and 1.5 is similar, as depicted in Figure 7.11(b and c). The centerline film cooling effectiveness is slightly increased on the pressure side for the upstream and up/downstream SSSH compared to the cylindrical and forward diffused shaped holes. On the suction side, these two schemes (upstream and up/downstream SSSH) notably outperform other configurations. For example, the centerline film cooling effectiveness obtained from the upstream SSSH is escalated by approximately a factor of 2 and 6 in comparison with that from the cylindrical hole at $M = 1.1$ and 1.5, respectively. Conversely, the downstream SSSH provides poor centerline film cooling effectiveness values in the downstream region at the high blowing ratios compared to the upstream and up/downstream SSSH. The forward diffused shaped hole does not demonstrate a significant improvement in centerline film cooling effectiveness compared to the cylindrical hole at high blowing ratios.

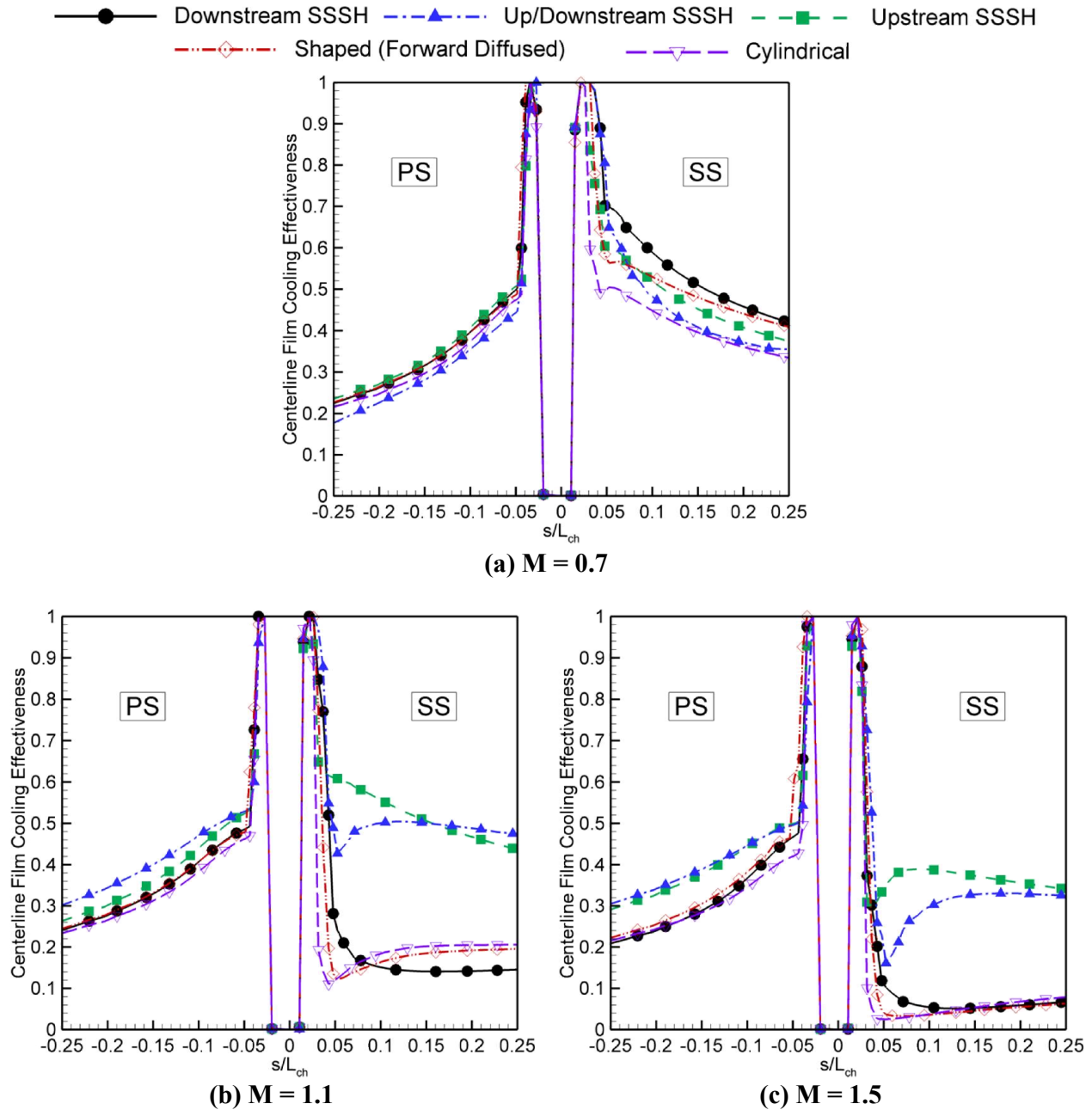


Figure 7.11: Centerline film cooling effectiveness

It should also be noticed that a sudden lowering in film cooling effectiveness after the injection hole, which represents the jet lift-off effect, is significantly diminished for the upstream and up/downstream SSSH schemes at $M = 1.1$ and 1.5 on the suction side of the blade. The cooling jet from the upstream SSSH is fully attached to the blade's surface at the blowing ratio of 1.1.

The predicted laterally averaged film cooling effectiveness results for various mentioned film hole configurations can be found in Figure 7.12. The downstream SSSH scheme performs similar to the forward diffused shaped hole with a slight improvement compared to the cylindrical hole at the leading edge for $M = 0.7$, as shown in Figure 7.12(a).

The upstream SSSH outperforms other cases on the pressure side and demonstrates better spanwise coverage of the coolant over the blade at the lowest blowing ratio. While on the suction side, all of the shaped holes except the up/downstream perform similarly. It seems that the cooling flow from the up/downstream SSSH is more concentrated towards the centerline region. In this regard, it provides even lower lateral film cooling effectiveness than the cylindrical hole; while it stands at higher centerline film cooling effectiveness values.

The up/downstream SSSH at the higher blowing ratio of 1.1 provides the highest laterally averaged film cooling effectiveness and consequently the widest lateral cooling coverage among other cases downstream of the pressure side of the blade. However, the upstream SSSH scheme outperforms it on the suction side in the downstream region closer to the injection hole, as illustrated in Figure 7.12(b). The predicted laterally averaged film cooling effectiveness results with the downstream SSSH are again disappointing on the suction side as is also the case for the centerline film cooling effectiveness. It is also observed that the film cooling effectiveness provided with this configuration does not provide any noticeable privilege to the forward diffused shaped hole for the range of blowing ratios that are used herein. Note that the lateral spread of the coolant from the cylindrical hole on the suction side stands at the value of about 0.12 based on the laterally averaged film cooling effectiveness results compared to the approximated averaged value of 0.7 for the forward diffused and downstream SSSH configurations.

In general, the laterally averaged film cooling effectiveness results for various hole shapes at the higher blowing ratio of $M = 1.5$ can be divided into two groups; wherein the first group includes the upstream and up/downstream SSSH schemes and the second group contains the cylindrical, downstream SSSH and forward diffused shaped holes. The predicted lateral coverage of the coolant at the leading edge of the blade, based on the laterally averaged film cooling effectiveness results, is significantly improved for the first group of hole schemes compared to the second group on both of the pressure and suction sides, as depicted in Figure 7.12(c). For instance, an approximate increase of 34% (on average) in laterally averaged

film cooling effectiveness can be observed for the upstream SSSH on the pressure side in comparison to that from the forward diffused shaped hole; this percentage of increase in the film cooling effectiveness value will be dramatically elevated on the suction side by a factor of 7 when considering the upstream SSSH over the forward diffused shaped hole.

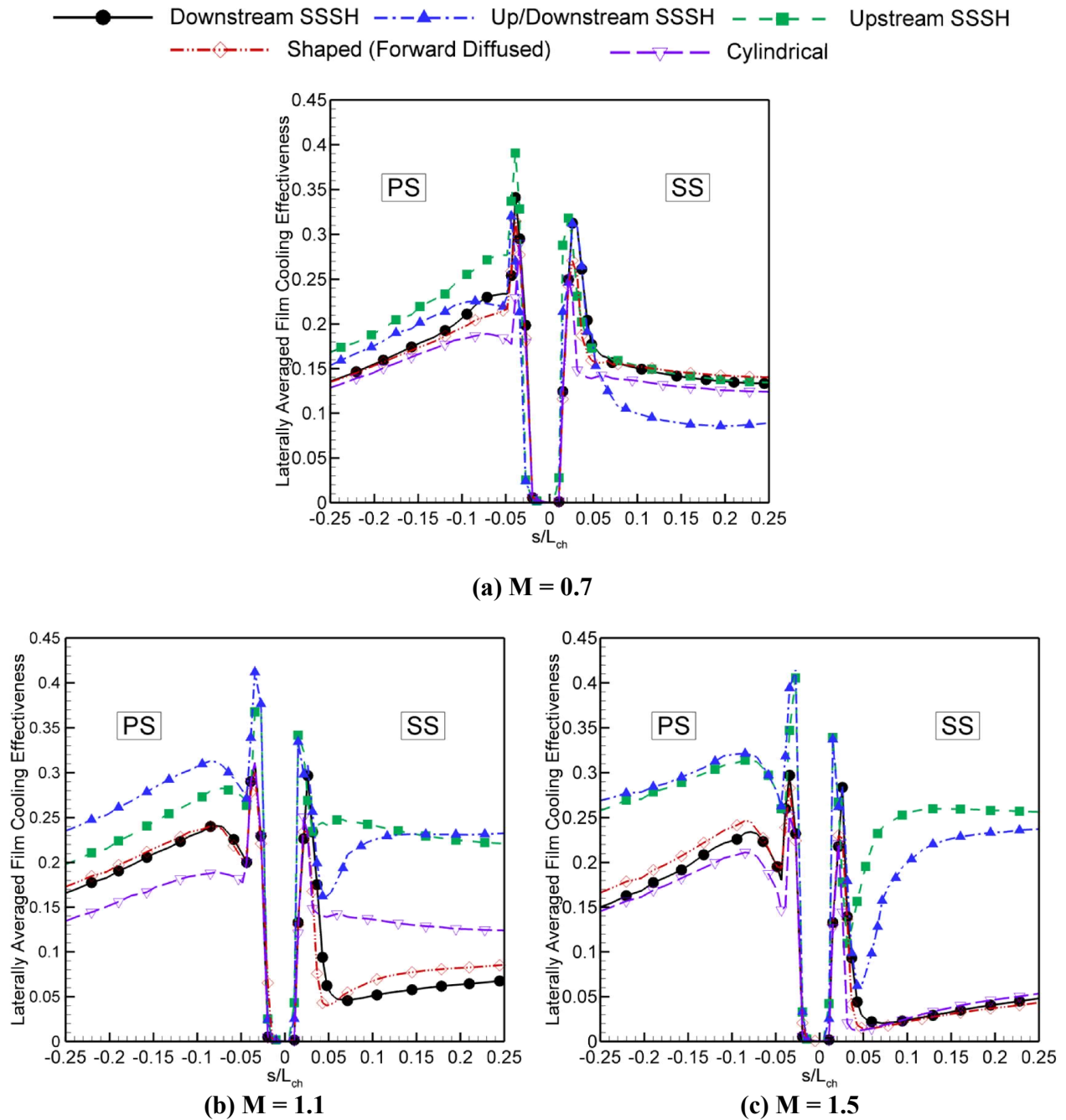


Figure 7.12: Laterally averaged film cooling effectiveness

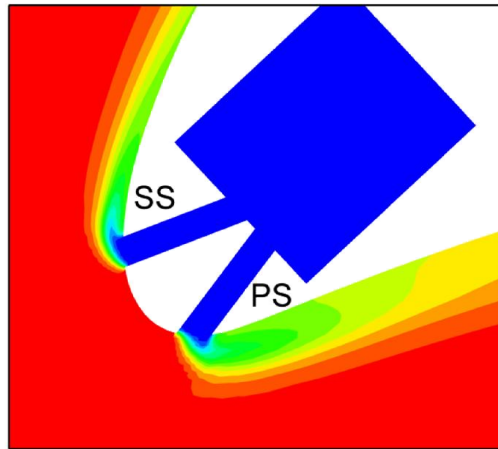
7.3.3. Temperature Contours

The temperature contours provide better insight of the behaviour of the cooling jets exiting from the holes and the mixing rate with the hot mainstream flow at the leading edge. Accordingly, the temperature contours at the mid-span plane for the shaped holes and cylindrical hole at three blowing ratios of 0.7, 1.1 and 1.5 are shown in Figure 7.13, Figure 7.14 and Figure 7.15, respectively.

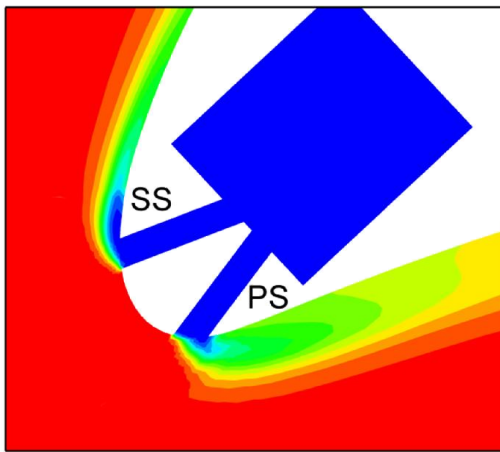
Due to the lower momentum of the cooling jets compared with the higher blowing ratio cases, less mixing of the coolant and hot mainstream is expected. For the low blowing ratio of $M = 0.7$ the coolant is attached to the blade surface on both suction and pressure sides for all hole geometries, as illustrated in Figure 7.13.

It should be mentioned here that the up/downstream SSSH scheme provides wider area at the blade's surface; hence, the momentum of the exiting jet will become lower than in other cases. Accordingly, due to the high value of the pressure on the pressure side the hot mainstream flow can penetrate inside the coolant air injection hole, as depicted in Figure 7.13(d). This phenomenon can also be seen in smaller scale for the forward diffused shaped hole. This has to be taken into consideration regarding the performance of the shaped holes on the pressure side; wherein, the momentum of the exiting jet might not be sufficient to defeat the mainstream flow and as a result the hot flow could penetrate into the film cooling pipe.

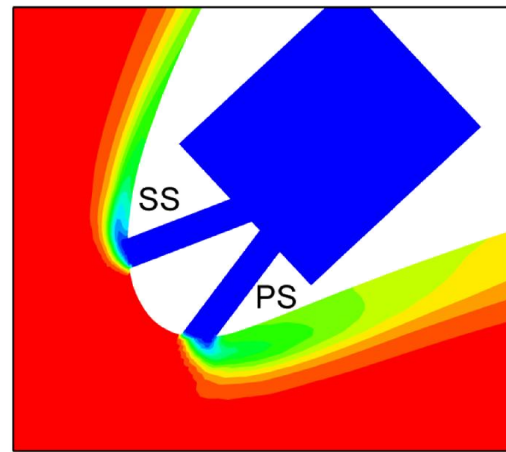
At the high blowing ratio of 1.1, the cooling flow is detached from the blade surface and hot mainstream flow is penetrated underneath the jet on the suction side for the cylindrical, downstream SSSH and forward diffused shaped holes, as shown in Figure 7.15(a, b and e), respectively. This jet lift-off can also be verified from the centerline film cooling effectiveness results in Figure 7.11. It should be mentioned here that the performance of these shaped holes also depends on the inlet flow angle. This has been reported in the numerical study of Benabed et al. [89] for the same cylindrical hole and cascade blade geometry used in the present chapter. They concluded that variations of the inlet flow angle can strongly affect film cooling performance, especially at lower blowing ratios. The stagnation moves from the suction side to the pressure side by altering the inlet flow angle from near horizontal to almost vertical.



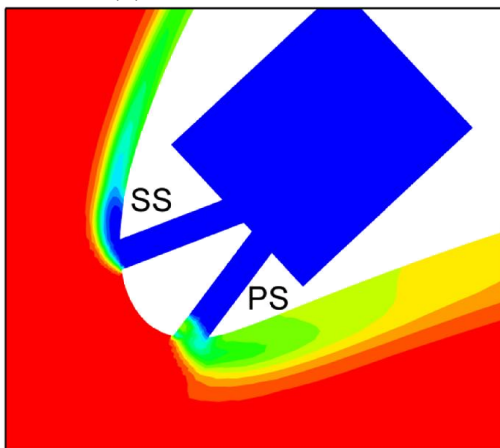
(a) Cylindrical



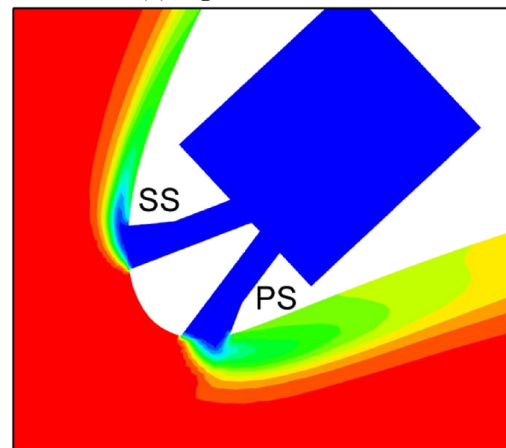
(b) Downstream SSSH



(c) Upstream SSSH

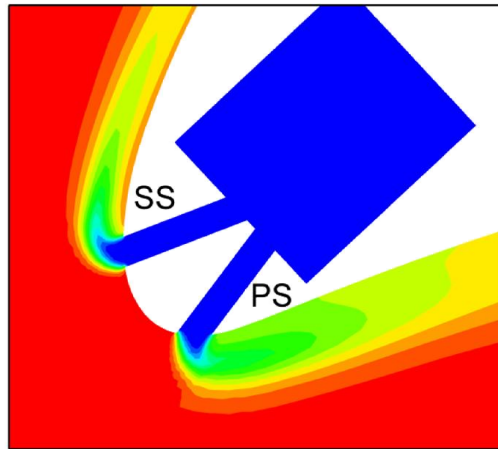


(d) Up/Downstream SSSH

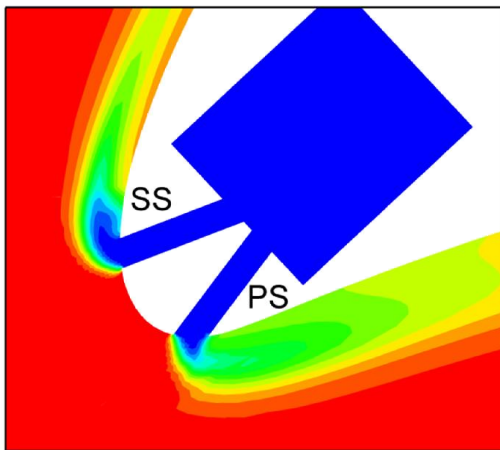


(e) Shaped (Forward Diffused)

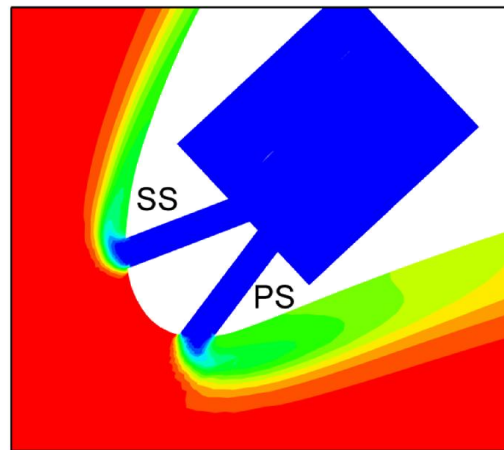
Figure 7.13: Temperature contours on mid-span plane for $M = 0.7$



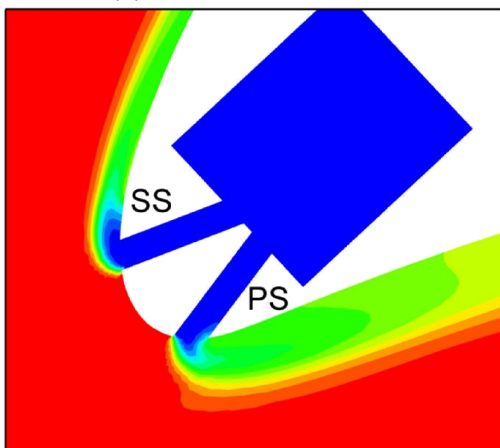
(a) Cylindrical



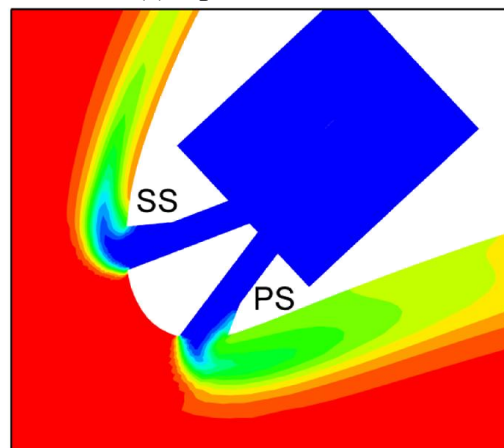
(b) Downstream SSSH



(c) Upstream SSSH

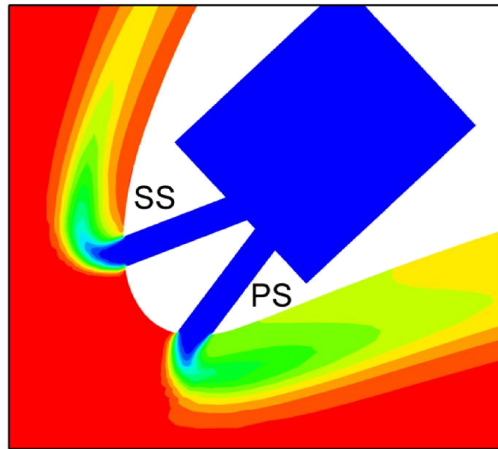


(d) Up/Downstream SSSH

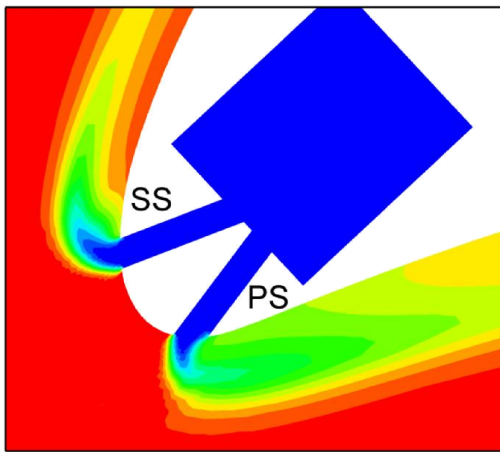


(e) Shaped (Forward Diffused)

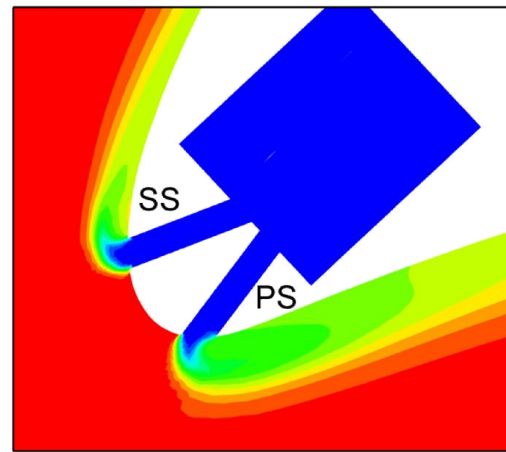
Figure 7.14: Temperature contours on mid-span plane for $M = 1.1$



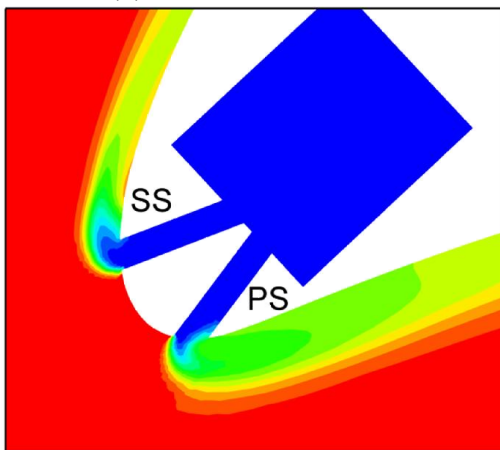
(a) Cylindrical



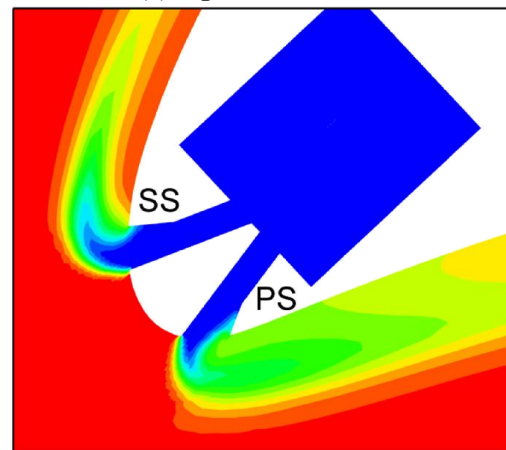
(b) Downstream SSSH



(c) Upstream SSSH



(d) Up/Downstream SSSH



(e) Shaped (Forward Diffused)

Figure 7.15: Temperature contours on mid-span plane for $M = 1.5$

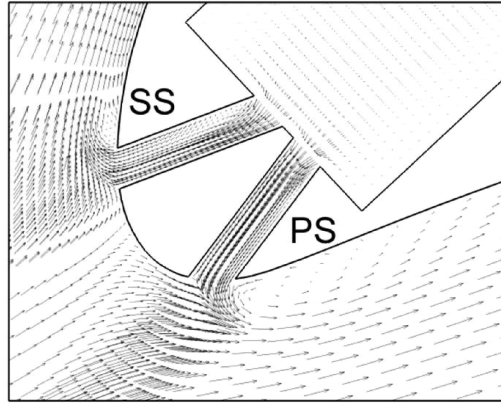
On the other hand, the cooling flow is adhered more to pressure side of the blade for the upstream and up/downstream SSSH configurations compared with other hole schemes. Similar trend of results for the temperature contours can be observed for the higher blowing ratio of $M = 1.5$ where the jet lift-off effect will become magnified, as shown in Figure 7.15. It should be noticed that the hot flow is entered into the downstream part of the injection hole (i.e., trailing edge of the hole) for the shaped holes on the pressure side. Better judgment on this can be made by observing the flow field behaviour which will be discussed in the following subsection. Note that the lowest amount of mixing between the coolant air and hot mainstream gas at the mid-span plane can be observed for the upstream and up/downstream SSSH schemes among other configurations at the blade's leading edge.

7.3.4. Velocity Plot Distributions

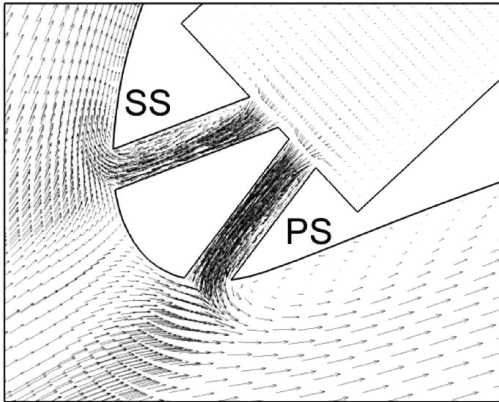
The flow field is visualised by the aid of the velocity vectors. The velocity plot distributions at the mid-span plane for the shaped holes and cylindrical hole at three blowing ratios of 0.7, 1.1 and 1.5 are shown in Figure 7.16, Figure 7.17 and Figure 7.18, respectively.

In Figure 7.16, the recirculation zone close to the trailing edge (TE) after the injection hole on the suction side can be recognized for the cylindrical and upstream SSSH holes, which considerably diminishes for the forward diffused shaped hole. However, it is almost vanished for the downstream SSSH schemes. As a result, higher values of the film cooling effectiveness are predicted for them in section 7.3.2 at the low blowing ratio of 0.7. On the pressure side all of the hole configurations perform almost equally in terms of the velocity distribution.

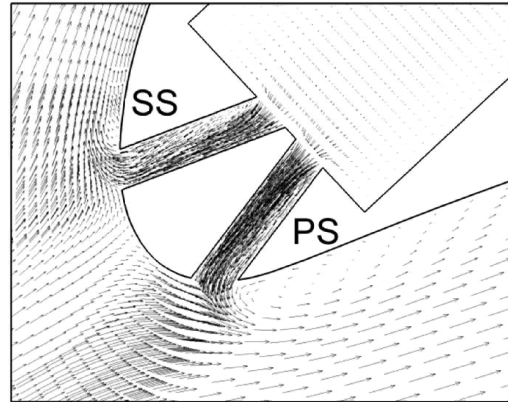
At the higher blowing ratio of $M = 1.1$, the coolant air flow is jetting-off and penetrates more into the mainstream flow when compared to the lowest blowing ratio, as shown in Figure 7.17. Once again, on the suction side, the recirculation zone of the flow has notably shrunk for the upstream and up/downstream SSSH in comparison with other cases. This also remains valid at the highest blowing ratio of $M = 1.5$ (see Figure 7.18). However, on the pressure side the flow plot distributions do not provide a notable difference for the different cases.



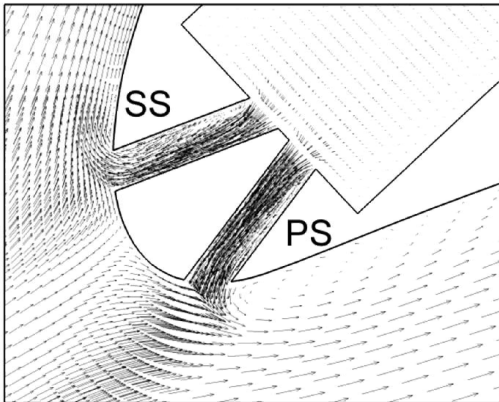
(a) Cylindrical



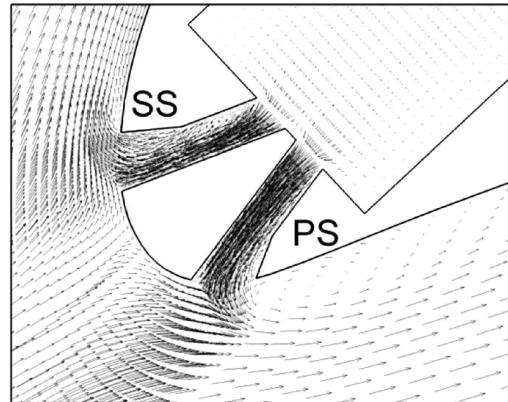
(b) Downstream SSSH



(c) Upstream SSSH

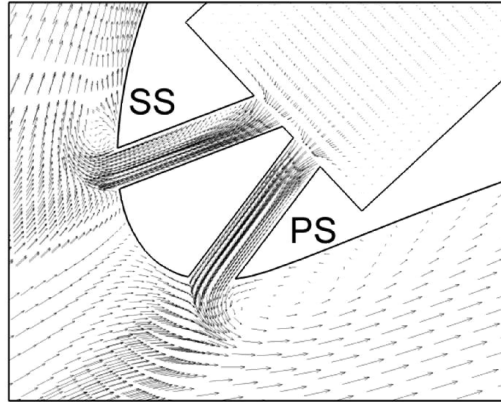


(d) Up/Downstream SSSH

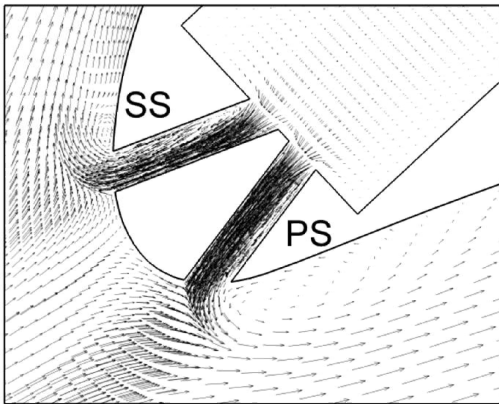


(e) Shaped (Forward Diffused)

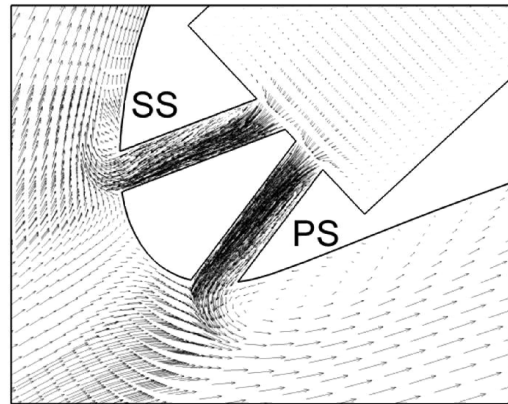
Figure 7.16: Velocity plot distributions on mid-span plane for $M = 0.7$



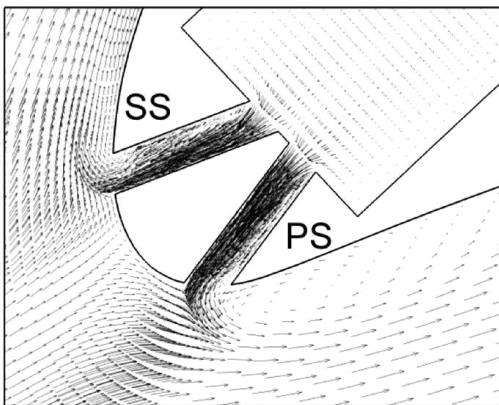
(a) Cylindrical



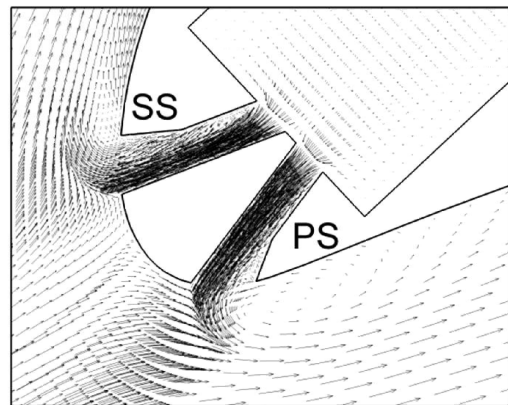
(b) Downstream SSSH



(c) Upstream SSSH



(d) Up/Downstream SSSH



(e) Shaped (Forward Diffused)

Figure 7.17: Velocity plot distributions on mid-span plane for $M = 1.1$

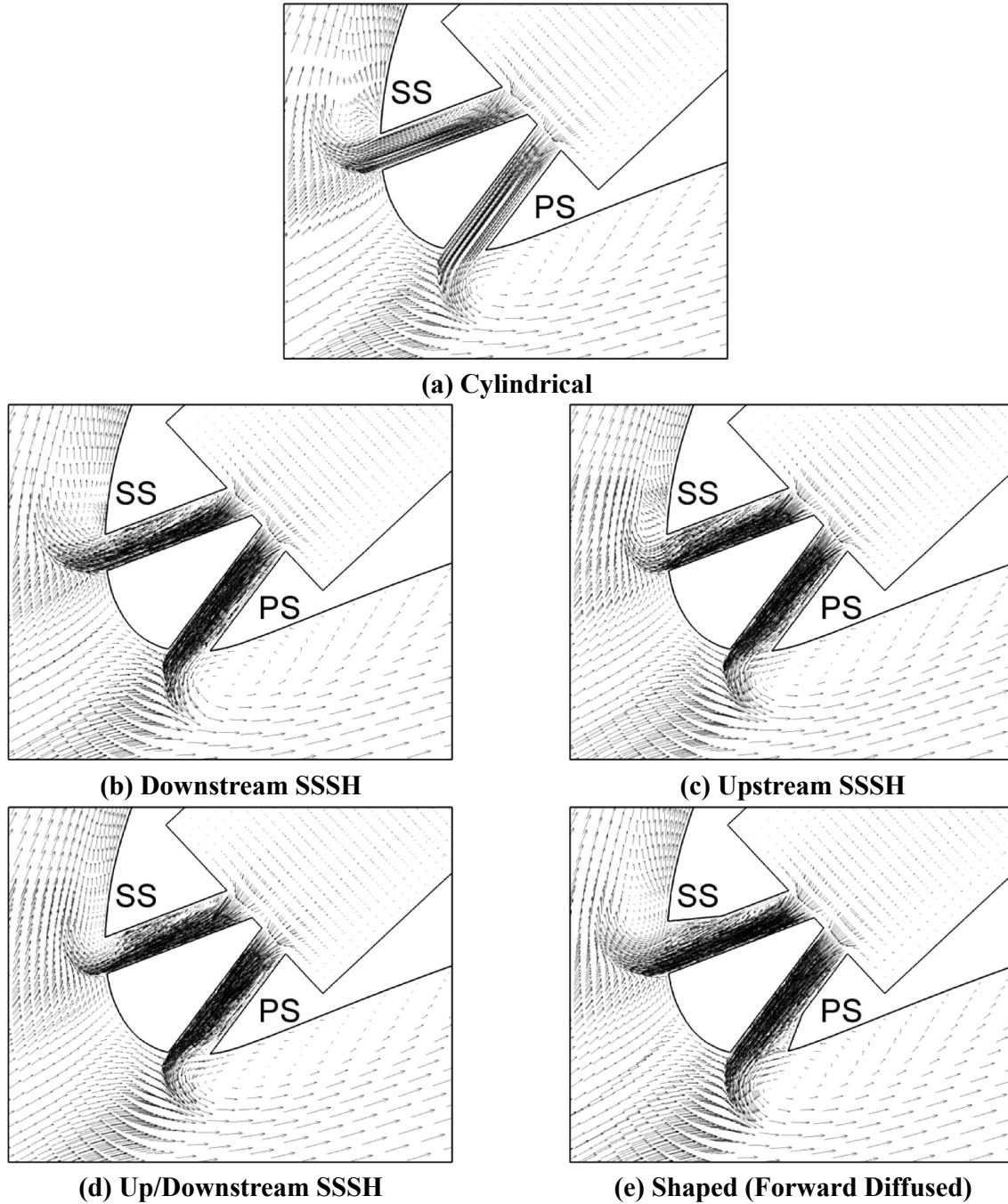


Figure 7.18: Velocity plot distributions on mid-span plane for $M = 1.5$

The high velocity zone for the flow inside of the injecting pipes on both the suction and pressure sides is more concentrated towards the side of the pipe which is closer to the stagnation point for all cases. Therefore, the high velocity zone at the exit plane of the jet shifts toward the leading edge (i.e., upstream) side of the hole at the high blowing ratios. This has also been

verified in the previous chapter (in Section 6.3.3). Therefore, the possibility for the hot flow to enter the exit part of the hole due to the low momentum zone which is formed at the TE side of the injection hole is increased, as seen in temperature contours' section (Section 7.3.3) for the forward diffused and up/downstream SSSH cases. It is worth mentioning here that at the high blowing ratio values ($M = 1.1$ and 1.5) the upstream and up/downstream SSSH schemes provide the minimum jet lift-off on both the suction side and pressure side of the blade. This leads to obtaining the highest values for the film cooling effectiveness through these two schemes as compared to other evaluated film cooling hole configurations.

7.4. CONCLUSIONS

In this chapter, the performance of the three proposed film cooling hole schemes, namely downstream, upstream and up/downstream sister shaped single-hole (SSSH) is numerically investigated on the leading edge of a turbine blade. The obtained results for both suction and pressure sides have been compared with the cylindrical and forward diffused shaped holes. Simulations are carried out at blowing ratio of 0.7 , 1.1 and 1.5 .

At the high blowing ratios of 1.1 and 1.5 , a noticeable improvement in film cooling performance including the film cooling effectiveness and the lateral spread of the cooling jet has been observed for the upstream and up/downstream SSSH schemes at the leading edge of the blade, in particular on the suction side. However, the general performance of the up/downstream SSSH scheme at the low blowing ratio of $M = 0.7$ was not satisfying.

The downstream SSSH configuration provided almost similar film cooling effectiveness values to that of the forward diffused shaped hole for low and high blowing ratios on both the pressure and suction side of the blade. Note that the obtained film cooling effectiveness for the downstream SSSH scheme at blowing ratios of $M = 1.1$ and 1.5 was disappointing in comparison with other SSSH schemes where much higher film cooling effectiveness values were obtained.

The mixing of the coolant with the high mainstream flow at the leading edge of the blade is considerably decreased for the upstream and up/downstream SSSH schemes and more adhered coolant to the blade's surface is observed than with other configurations. Moreover, the jet lift-off is notably diminished for the upstream and up/downstream SSSH compared to other hole geometries.

8. CONCLUSIONS & RECOMMENDATIONS FOR FUTURE WORK

In this chapter, the conclusions obtained through intensive numerical analyses regarding the performance of novel and existing film cooling schemes have been presented. The chapter begins with concluding remarks entailing the findings of this research study followed by a summary of the contributions. The final section of this chapter suggests potential future work following the present study.

8.1. CONCLUSIONS

The conclusions presented in this chapter have been produced while considering low blowing ratios of 0.25 and 0.5, and high blowing ratios of 1 and 1.5 for the flat plate film cooling. Moreover, blowing ratios of 0.7, 1.1, and 1.5 have been considered for the analysis on the leading edge of the AGTB-B1 blade.

To evaluate the performance of the CESH configuration, the results obtained have been compared with the EESH geometry as well as with the influence of sister holes and it has been determined that higher film cooling effectiveness is achieved at blowing ratios of 1 and 1.5, results of which are even greater when considering the influence of discrete sister holes where adiabatic film cooling effectiveness results reach a plateau. The proposed novel geometry did not have ample effect on the results at the lower blowing ratios. Analysis of the flow structure validated that the CRVP are responsible for the jet lift-off effect and inherently decrease the performance in film cooling while increasing the aerodynamic losses. The analysis illustrated a decrease in the strength of the vortex pairs for the CESH scheme and thereby provides more attached coolant to the plate's surface. Furthermore, the repositioning of the sister holes for the CESH scheme shifted the vortices away from the centerline plane to assist the coolant air flow to spread in the spanwise direction. To this end, examination of the jet exit condition confirmed that the hole geometry, blowing ratio and the exit shape hole have significant effects on the flow variables on the jet exit plane.

To further investigate the performance of the sister holes, numerical simulations using modified locations of the discrete sister holes in the streamwise and spanwise directions have been investigated. Analysis results for the centerline and laterally averaged film cooling effectiveness show that insignificant effects are produced with variations in the streamwise direction and similar results are obtained to that of the base case. Hence, the base case with sister holes' location of $x/D = \pm 0.75$ is considered the better candidate among all other cases for the streamwise variations. On the other hand, spanwise variation of the sister holes' location had a significant effect on the film cooling effectiveness results. The obtained laterally averaged effectiveness for a considered case (3z) demonstrates an increase of approximately 78% and 49% as compared to the base case for $M = 1$ and 1.5, respectively. The lateral spreading of the coolant from the sister holes in the far downstream region of the injection hole is directly dependent on the spanwise location of the sister holes. Wherein placing the sister holes in the farther locations from the centerline increases the lateral spread of the coolant over the plate's surface. This has also been verified through the flow structure analysis.

To elaborate on the conclusions made from the present study, three novel film cooling hole schemes, namely downstream, upstream and up/downstream sister shaped single-hole (SSSH) have been proposed where the upstream and latter SSSH schemes have shown notable improvements in film cooling performance, wherein more lateral distribution of coolant is obtained and less penetration of coolant into the mainstream flow is observed, when compared with the cylindrical and forward diffused shaped holes. The jet lift-off and the CRVP strength are significantly decreased for the downstream and up/downstream SSSH schemes. As a result, more coolant is attached to the plate's surface. In general, the downstream and up/downstream SSSH schemes performed equally well for all blowing ratios, while, the downstream SSSH has a less complex design process than the up/downstream scheme. In comparison with the upstream sister-shaped parts, the constituent downstream sister-shaped components prove to have a dominating effect on countering the CRVP vortices and the flow existing from the primary hole. The upstream SSSH provided a similar film cooling performance as the forward diffused shaped hole in terms of film cooling effectiveness and downstream vortex structures for the low blowing ratios. However, the upstream SSSH outperforms other cases in the farther downstream region at the high blowing ratios of 1 and 1.5.

The SSSH configurations have been applied to the leading edge of the AGTB-B1 blade where a noticeable improvement in film cooling performance including the effectiveness and the lateral spread of the cooling jet has been observed for the upstream and up/downstream SSSH schemes, particularly on the suction side, at blowing ratios of 1.1 and 1.5. However, low performance of the up/downstream SSSH scheme was observed at the lower blowing ratio of $M = 0.7$. The downstream SSSH configuration provided almost similar film cooling effectiveness values to that of the forward diffused shaped hole for low and high blowing ratios on both the pressure and suction side of the blade. The obtained centerline and laterally averaged film cooling effectiveness results for the downstream SSSH at blowing ratios of $M = 1.1$ and 1.5 were disappointing in comparison with other SSSH schemes where much higher film cooling effectiveness values were obtained. The mixing of the coolant with the high mainstream flow at the leading edge of the blade is considerably decreased for the upstream and up/downstream SSSH schemes and more adhered coolant to the blade's surface is observed than with other configurations. Moreover, the jet lift-off is notably diminished for the upstream and up/downstream SSSH compared to other hole geometries.

8.2. RECOMMENDATIONS FOR FUTURE WORK

To expand on the work of this research and to put the suggested film cooling schemes into practice, this section provides recommendations for future work.

Due to the state of modern computational technology, the results obtained herein are limited, however accurate, to the accuracy of the Reynolds-Averaged Navier-Stokes (RANS) models used to devise the preliminary assessment for the present research. By using more advanced flow field modeling techniques such as large eddy simulation (LES) or direct numerical simulation (DNS) the accuracy of the results can be further tuned to more accurately reflect the complex nature of film cooling flow. Moreover, the thermal field modeling can be further improved by implementing advanced models for the turbulent heat flux vector.

From the analysis carried out in this research, it is evident that the careful design of film hole geometries, with meticulous consideration to tolerances and precise hole angles and configurations, plays a vital role in the optimization of the film cooling effectiveness and overall performance. To this end, the author recommends further design considerations to be made such as alterations in the discrete sister holes' diameter and/or their injection angle to find an optimal

configuration for maximizing the performance of film cooling turbine blades. To expand on this notion, the proposed SSSH schemes can also be optimized where modifications can be made to the diameters of the merged sister holes as well as their angles with respect the main injection hole.

With modern-day technologies rapidly advancing toward micro-levels it would be of major interest to assess the performance of the proposed film cooling schemes on the micro-scale level. However, this notion raises further implications, namely deposition – from volcanic ash or sand that could clog the film holes and be detrimental to the performance of the blades.

To add to the practicality of the current research, it is highly recommend that experimental evaluation of the proposed film cooling geometries is conducted to simulate the theoretical aspects of this research in the laboratory environment under various flow conditions.

The manufacturing of advanced film cooling holes requires highly precise machinery and skilled labour. To fully exploit the benefits of the work presented herein it is of great importance to ensure the manufacturing of the stated schemes is cost effective. As such, researching into methods of optimizing the manufacturability of the presented work can lead to the application of the proposed hole schemes for today's aircraft and terrestrial turbines.

It is also recommended to investigate the effects of conjugate heat transfer on film cooling prediction by considering the conduction heat transfer within the solid body of the turbine blade rather than assuming adiabatic wall boundaries.

APPENDIX A: PEER REVIEWED PUBLICATIONS

Journals

- (1) Khajehhasani, S., and Jubran, B. A., 2013, “A Numerical Evaluation of the Performance of Film Cooling from a Circular Exit Shaped Hole with Sister Holes Influence”, *Heat Transfer Engineering*, (submitted).
- (2) Khajehhasani, S., and Jubran, B. A., 2014, “A Numerical Investigation of Film Cooling Performance through Variations in the Location of Discrete Sister Holes”, *International Journal of Heat and Fluid Flow*, (submitted).
- (3) Khajehhasani, S., and Jubran, B. A., 2014, “Numerical Assessment of the Film Cooling through Novel Sister Shaped Single-Hole Schemes using CFD”, *Numerical Heat Transfer: Part A*, (accepted).

Conferences

- (4) Khajehhasani, S., and Jubran, B. A., 2013, “Film Cooling from Circular and Elliptical Exit Shaped Holes with Sister Hole Influence”, *Proceedings of ASME Turbo Expo 2013*, No. GT2013-95138.
- (5) Khajehhasani, S., and Jubran, B. A., 2013, “Comparison of Various Turbulence Models to Predict Film Cooling Effectiveness from Different Exit Shaped Holes with Sister Holes Influence”, *Proceedings of the 21st Annual Conference of the CFD Society of Canada*, Sherbrooke, Quebec, Canada.
- (6) Khajehhasani, S., and Jubran, B. A., 2013, “Numerical Simulation of Film Cooling from a Circular Exit Shaped Hole with Sister Holes Influence”, *Proceedings of Canadian Aeronautics and Space Institute (CASI) 60th Aeronautics Conference and AGM*, Toronto, Ontario, Canada.

- (7) Khajehhasani, S., and Jubran, B. A., 2014, "A CFD-Based Parametric Study on Modification of Discrete Sister Holes Location for the Film Cooling Flow", *Proceedings of ASME Turbo Expo 2014*, No. GT2014-25970.
- (8) Khajehhasani, S., and Jubran, B. A., 2014, "Predictions of the Effects of Discrete Sister Holes' Location on Film Cooling Performance", *Proceedings of the 22nd Annual Conference of the CFD Society of Canada*, Toronto, Ontario, Canada.
- (9) Khajehhasani, S., and Jubran, B. A., 2014, "Film Cooling from Novel Sister Shaped Single-Holes", *Proceedings of ASME Turbo Expo 2014*, No. GT2014-25971.
- (10) Khajehhasani, S., and Jubran, B. A., 2014, "A Numerical Investigation on the Performance of Novel Sister Shaped Single-Hole Configurations for Film Cooling Flow", *Proceedings of ASME 2014 International Mechanical Engineering Congress & Exposition*, No. IMECE2014-36263, (submitted).

APPENDIX B: PROFILE COORDINATES FOR AGTB BLADE

The Profile coordinates in bitangent-system for AGTB blade (cord length of 250mm) are presented in Table B.1 [85].

Table B.1: Profile coordinates in bitangent-system for AGTB blade

x (mm)	y (mm)						
144.2116	100.8619	245.2333	0	100.0766	45.1569	4.005584	2.220171
151.5596	96.42524	243.9998	0.283368	94.77442	44.41012	3.17464	3.201671
158.5297	91.82312	242.8723	0.838406	89.62704	43.47302	2.490543	4.324383
165.2226	87.03907	241.8483	1.521105	84.63445	42.34561	1.83917	5.648169
171.6681	82.13021	240.2566	2.647088	79.7966	41.02788	1.334613	7.113171
177.8961	77.15351	238.0808	4.11583	75.02658	39.49272	0.87636	8.735757
183.9067	72.10903	235.3645	5.940874	70.26731	37.77005	0.521439	10.486
189.8304	67.03741	232.1347	8.035261	65.50243	35.75932	0.212816	12.39382
195.523	61.94146	228.4621	10.32557	60.67488	33.4905	0	19.96199
201.1015	56.90541	224.3332	12.8553	55.78469	30.96354	0.646211	27.9889
206.479	51.90207	219.832	15.50753	50.81547	28.07794	2.031697	36.24632
211.6418	46.97494	214.9722	18.23879	45.72653	24.96414	4.083042	44.66368
216.5765	42.16751	209.7537	21.04907	40.54505	21.53517	6.811013	53.05345
221.2694	37.52328	204.2472	23.86496	35.37429	17.9187	10.0987	61.33147
225.6906	32.9852	198.4798	26.59949	30.25779	14.12829	14.07377	69.39438
229.8294	28.74077	192.4949	29.26621	25.28529	10.33506	18.74978	77.1987
233.6123	24.71939	186.3496	31.8352	20.6607	6.650317	24.17023	84.75803
237.0557	21.02159	180.0575	34.26298	16.49016	3.345744	30.50624	91.98251
240.1162	17.63381	173.6322	36.50605	15.40813	2.531171	37.97244	98.79601
242.7666	14.64302	167.1741	38.54805	14.38594	1.830693	46.54971	104.9539
244.9933	12.09271	160.6833	40.38899	13.33663	1.217197	56.30298	110.0948
246.7829	10.02638	154.1868	41.94187	12.33362	0.761277	66.93861	113.9362
248.1217	8.487496	147.7582	43.27733	11.34698	0.405895	77.96188	116.2285
248.9526	7.506001	141.3675	44.3383	10.37671	0.151047	88.98424	116.9935
249.6503	6.3398	135.0445	45.18183	9.409228	0.040223	99.66342	116.4109
250	5.065111	128.9034	45.74807	8.51517	0	109.7576	114.6439
249.9448	3.711862	122.8438	46.05341	7.667407	0.117366	119.2888	112.081
249.4876	2.424077	116.9389	46.16839	6.792514	0.321705	128.1429	108.7821
247.6793	0.571888	111.1588	46.03606	5.792779	0.773412	136.4396	104.9753
246.4888	0.105217	105.5335	45.71336	4.882806	1.396255	144.2116	100.8619

REFERENCES

- ¹ Lakshminarayana, B., 1996, “*Fluid Dynamics and Heat Transfer of Turbomachinery*”: John Wiley & Sons, New York, USA.
- ² Dixon, S. L., 2005, “*Fluid Mechanics, Thermodynamics of Turbomachinery*”: Fifth Edition, Elsevier Butterworth-Heinemann, USA.
- ³ Ely, M. J., and Jubran, B. A., 2008, “A Numerical Study on Increasing Film Cooling Effectiveness Through the Use of Sister Holes”, *Proceedings of ASME Turbo Expo 2008*, No. GT2008-50366, pp. 341-350.
- ⁴ Johnson, P. L., Shyam, V., and Hah, C., 2011, “Reynolds-Averaged Navier-Stokes Solutions to Flat Plate Film Cooling Scenarios”, *National Aeronautics and Space Administration, Glenn Research Center*, No. NASA/TM-2011-217025, pp. 1-21.
- ⁵ Lutum, E., and Johnson, B. V., 1999, “Influence of the Hole Length-to-Diameter Ratio on Film Cooling With Cylindrical Holes”, *Journal of Turbomachinery*, Vol. 121, No. 2, pp. 209-216.
- ⁶ Kohli, A., and Bogard, D. G., 1997, “Adiabatic Effectiveness, Thermal Fields, and Velocity Fields for Film Cooling With Large Angle Injection”, *Journal of Turbomachinery*, Vol. 119, No. 2, pp. 352-358.
- ⁷ Baldauf, S., Schulz, A., Wittig, S., and Scheurlen, M., 2002, “Correlation of Film-Cooling Effectiveness From Thermographic Measurements at Enginelike Conditions”, *Journal of Turbomachinery*, Vol. 124, No. 4, pp. 686-698.
- ⁸ Sinha, A. K., Bogard, D. G., and Crawford, M. E., 1991, “Film-Cooling Effectiveness Downstream of a Single Row of Holes With Variable Density Ratio”, *Journal of Turbomachinery*, Vol. 113, No. 3, pp. 442-449.
- ⁹ Bunker, R. S., 2005, “A Review of Shaped Hole Turbine Film-Cooling Technology”, *Journal of Heat Transfer*, Vol. 127, No. 4, pp. 441-453.

- 10 Sargison, J. E., Guo, S. M., Oldfield, M. L. G., Lock, G. D., and Rawlinson, A. J., 2002, “A Converging Slot-Hole Film-Cooling Geometry–Part 1: Low-Speed Flat-Plate Heat Transfer and Loss”, *Journal of Turbomachinery*, Vol. 124, No. 3, pp. 453-460.
- 11 Sargison, J. E., Guo, S. M., Oldfield, M. L. G., Lock, G. D., and Rawlinson, A. J., 2002, “A Converging Slot-Hole Film-Cooling Geometry–Part 2: Transonic Nozzle Guide Vane Heat Transfer and Loss”, *Journal of Turbomachinery*, Vol. 124, No. 3, pp. 461-471.
- 12 Sargison, J. E., Oldfield, M. L. G., Guo, S. M., Lock, G. D., and Rawlinson, A. J., 2005, “Flow Visualisation of the External Flow from a Converging Slot-Hole FilmCooling Geometry”, *Experiments in Fluids*, Vol. 38, No. 3, pp. 304-318.
- 13 Liu, C. L., Zhu, H. R., Bai, J. T., and Xu, D. C., 2010, “Film Cooling Performance of Converging Slot-Hole Rows on A Gas Turbine Blade”, *International Journal of Heat and Mass Transfer*, Vol. 53, No. 23–24, pp. 5232-5241.
- 14 Azzi, A., and Jubran, B., 2007, “Numerical Modelling of Film Cooling From Converging Slot-Hole”, *Heat and Mass Transfer*, Vol. 43, No. 4, pp. 381-388.
- 15 Bruce-Black, J. E., Davidson, F. T., Bogard, D. G., and Johns, D. R., 2011, “Practical Slot Configurations for Turbine Film Cooling Applications”, *Journal of Turbomachinery*, Vol. 133, No. 031020, pp. 1-8.
- 16 Liu, C.-l., Zhu, H.-r., Bai, J.-t., and Xu, D.-c., 2011, “Experimental and Numerical Investigation on the Film Cooling of Waist-Shaped Slot Holes Comparing With Converging Slot Holes”, *Journal of Turbomachinery*, Vol. 134, No. 1, pp. 011021-1-11.
- 17 Baheri Islami, S., Alavi Tabrizi, S. P., Jubran, B. A., and Esmaeilzadeh, E., 2010, “Influence of Trenched Shaped Holes on Turbine Blade Leading Edge Film Cooling”, *Heat Transfer Engineering*, Vol. 31, No. 10, pp. 889-906.
- 18 Waye, S. K., and Bogard, D. G., 2006, “High-Resolution Film Cooling Effectiveness Measurements of Axial Holes Embedded in a Transverse Trench With Various Trench Configurations”, *Journal of Turbomachinery*, Vol. 129, No. 2, pp. 294-302.

- ¹⁹ Lu, Y., Bunker, R. S., Dhungel, A., and Ekkad, S. V., 2009, "Effect of Trench Width and Depth on Film Cooling From Cylindrical Holes Embedded in Trenches", *Journal of Turbomachinery*, Vol. 131, No. 1, pp. 011003-1-13.
- ²⁰ Abdala, A. M., Zheng, Q., Elwekeel, F. M., and Dong, P., 2013, "Computational Film Cooling Effectiveness of Dual Trench Configuration on Flat Plate at Moderate Blowing Ratios", *Journal of Marine Science and Application*, Vol. 12, No. 2, pp. 208-218.
- ²¹ Walters, D. K., and Lylek, J. H., 2000, "A Detailed Analysis of Film-Cooling Physics: Part I-Streamwise Injection With Cylindrical Holes", *Journal of Turbomachinery*, Vol. 122, No. 1, pp. 102-112.
- ²² Zhang, X. Z., and Hassan, I., 2006, "Film Cooling Effectiveness for an Advanced-Louver Cooling Scheme for Gas Turbines", *Journal of Thermophysics and Heat Transfer*, Vol. 20, No. 4, pp. 754-763.
- ²³ Fric, T., and Roshko, A., 1994, "Vortical Structure in the Wake of a Transverse Jet", *Journal of Fluid Mechanics*, Vol. 279, No. 1, pp. 1-47.
- ²⁴ Haven, B. A., and Kurosaka, M., 1997, "Kidney and Anti-Kidney Vortices in Crossflow Jets", *Journal of Fluid Mechanics*, Vol. 352, pp. 27-64.
- ²⁵ New, T. H., Lim, T. T., and Luo, S. C., 2003, "Elliptic Jets in Cross-Flow", *Journal of Fluid Mechanics*, Vol. 494, pp. 119-140.
- ²⁶ Ghorab, M. G., 2013, "Cooling Performance and Flow-Field Analysis of a Hybrid Scheme with Different Outlet Configurations", *Applied Thermal Engineering*, Vol. 61, No. 2, pp. 799-816.
- ²⁷ Takahashi, H., Nuntadusit, C., Kimoto, H., Ishida, H., Ukai, T., and Takeishi, K., 2001, "Characteristics of Various Film Cooling Jets Injected in a Conduit", *Annals of the New York Academy of Sciences*, Vol. 934, No. 1, pp. 345-352.

- 28 Aga, V., Rose, M., and Abhari, R. S., 2008, “Experimental Flow Structure Investigation of Compound Angled Film Cooling”, *Journal of Turbomachinery*, Vol. 130, No. 3, pp. 031005-1-8.
- 29 McGovern, K., and Leylek, J., 2000, “A Detailed Analysis of Film-Cooling Physics: Part I-Compound-Angle Injection with Cylindrical Holes”, *Journal of turbomachinery*, Vol. 122, No. 1, pp. 113-121.
- 30 Gräf, L., and Kleiser, L., 2012, “Flow-Field Analysis of Anti-Kidney Vortex Film Cooling”, *Journal of Thermal Science*, Vol. 21, No. 1, pp. 66-76.
- 31 Rigby, D. L., and Heidmann, J. D., 2008, “Improved Film Cooling Effectiveness by Placing a Vortex Generator Downstream of Each Hole”, *Proceedings of ASME Turbo Expo 2008*, No. GT2008-51361, pp. 1161-1174.
- 32 An, B., Liu, J., Zhang, C., and Zhou, S., 2013, “Film Cooling of Cylindrical Hole With a Downstream Short Crescent-Shaped Block”, *Journal of Heat Transfer*, Vol. 135, No. 3, pp. 031702-1-9.
- 33 Cain, D., and Duffy, J., 1971, “An Experimental Investigation of Turbulent Flow in Elliptical Ducts”, *International Journal of Mechanical Sciences*, Vol. 13, No. 5, pp. 451-459.
- 34 Velusamy, K., Garg, V. K., and Vaidyanathan, G., 1995, “Fully Developed Flow and Heat Transfer in Semi-Elliptical Ducts”, *International Journal of Heat and Fluid Flow*, Vol. 16, No. 2, pp. 145-152.
- 35 Voronova, T. V., and Nikitin, N. V., 2006, “Direct Numerical Simulation of the Turbulent Flow in An Elliptical Pipe”, *Computational Mathematics and Mathematical Physics*, Vol. 46, No. 8, pp. 1378-1386.
- 36 Goldstein, R. J., Eckert, E. R. G., and Burggraf, F., 1974, “Effects of Hole Geometry and Density on Three-Dimensional Film Cooling”, *International Journal of Heat and Mass Transfer*, Vol. 17, No. 5, pp. 595-607.

- 37 Saumweber, C., and Schulz, A., 2008, "Comparison the Cooling Performance of Cylindrical and Fan-Shaped Cooling Holes With Special Emphasis on the Effect of Internal Coolant Cross-Flow", *Proceedings of ASME Turbo Expo 2008*, No. GT2008-51036, pp. 893-903.
- 38 Saumweber, C., and Schulz, A., 2008, "Free-Stream Effects on The Cooling Performance of Cylindrical and Fan-Shaped Cooling Holes", *Journal of Turbomachinery*, Vol. 134, No. 6, pp. 061007-1-12.
- 39 Saumweber, C., and Schulz, A., 2008, "Effect of Geometry Variations on the Cooling Performance of Fan-Shaped Cooling Holes", *Journal of Turbomachinery*, Vol. 134, No. 6, pp. 061008-1-16.
- 40 Lee, K.-D., and Kim, K.-Y., 2010, "Shape Optimization of a Fan-Shaped Hole to Enhance Film-Cooling Effectiveness", *International Journal of Heat and Mass Transfer*, Vol. 53, No. 15–16, pp. 2996-3005.
- 41 Montomoli, F., D'Ammaro, A., and Uchida, S., 2013, "Numerical and Experimental Investigation of a New Film Cooling Geometry with High P/D Ratio", *International Journal of Heat and Mass Transfer*, Vol. 66, pp. 366-375.
- 42 Gritsch, M., Colban, W., Schar, H., and Dobbeling, K., 2005, "Effect of Hole Geometry on the Thermal Performance of Fan-Shaped Film Cooling Holes", *Journal of Turbomachinery*, Vol. 127, No. 4, pp. 718-725.
- 43 Lee, K.-D., and Kim, K.-Y., 2012, "Performance Evaluation of a Novel Film-Cooling Hole", *Journal of Heat Transfer*, Vol. 134, No. 10, pp. 101702-1-7.
- 44 Takeishi, K., Komiyama, M., Oda, Y., Egawa, Y., and Kitamura, T., 2011, "Aerothermal Investigations on Mixing Flow Field of Film Cooling With Swirling Coolant Flow", *Proceedings of ASME Turbo Expo 2011*, No. GT2011-46838.
- 45 Liu, J. S., Malak, M. F., Tapia, L. A., Crites, D. C., Ramachandran, D., Srinivasan, B., Muthiah, G., and Venkataramanan, J., 2010, "Enhanced Film Cooling Effectiveness with

- New Shaped Holes”, *Proceedings of ASME Turbo Expo 2010*, No. GT2010-22774, pp. 1517-1527.
- ⁴⁶ Kim, S. M., Lee, K. D., and Kim, K. Y., 2012, “A Comparative Analysis of Various Shaped Film-Cooling Holes”, *Heat and Mass Transfer*, Vol. 48, No. 11, pp. 1929-1939.
- ⁴⁷ Yusop, N. M., Ali, A. H., and Abdullah, M. Z., 2013, “Computational Study of a New Scheme for a Film-Cooling Hole on Convex Surface of Turbine Blades”, *International Communications in Heat and Mass Transfer*, Vol. 43, pp. 90-99.
- ⁴⁸ Kusterer, K., Elyas, A., Bohn, D., Sugimoto, T., Tanaka, R., and Kazari, M., 2011, “The NEKOMIMI Cooling Technology: Cooling Holes With Ears for High-Efficient Film Cooling”, *Proceedings of ASME Turbo Expo 2011*, No. GT2011-45524, pp. 303-313.
- ⁴⁹ Kusterer, K., Tekin, N., Reiners, F., Bohn, D., Sugimoto, T., Tanaka, R., and Kazari, M., 2013, “Highest-Efficient Film Cooling by Improved NEKOMIMI Film Cooling Holes: Part 1: Ambient Air Flow Conditions”, *Proceedings of ASME Turbo Expo 2013*, No. GT2013-95027.
- ⁵⁰ Kusterer, K., Tekin, N., Kasiri, A., Bohn, D., Sugimoto, T., Tanaka, R., and Kazari, M., 2013, “Highest-Efficient Film Cooling by Improved NEKOMIMI Film Cooling Holes: Part 2: Hot Gas Flow Conditions”, *Proceedings of ASME Turbo Expo 2013*, No. GT2013-95042.
- ⁵¹ Han, C., Ren, J., and Jiang, H.-d., 2012, “Multi-Parameter Influence on Combined-Hole Film Cooling System”, *International Journal of Heat and Mass Transfer*, Vol. 55, No. 15–16, pp. 4232-4240.
- ⁵² Javadi, A., Javadi, K., Taeibi-Rahni, M., and Darbandi, M., 2003, “A New Approach to Improve Film Cooling Effectiveness using Combined Jets”, *Proceedings of the International Gas Turbine Congress 2003 Tokyo*, No. IGTC2003Tokyo TS -071, pp. 1-9.
- ⁵³ Javadi, K., Taeibi-Rahni, M., and Darbandi, M., 2007, “Jet-into-Crossflow Boundary-Layer Control: Innovation in Gas Turbine Blade Cooling”, *AIAA Journal*, Vol. 45, No. 12, pp. 2910-2925.

- 54 Kusterer, K., Bohn, D., Sugimoto, T., and Tanaka, R., 2007, “Double-Jet Ejection of Cooling Air for Improved Film Cooling”, *Journal of Turbomachinery*, Vol. 129, No. 4, pp. 809-815.
- 55 Heidmann, J. D., and Ekkad, S., 2008, “A Novel Antivortex Turbine Film-Cooling Hole Concept”, *Journal of Turbomachinery*, Vol. 130, No. 3, pp. 031020-1-9.
- 56 Dhungel, A., Lu, Y., Phillips, W., Ekkad, S. V., and Heidmann, J., 2009, “Film Cooling From a Row of Holes Supplemented With Antivortex Holes”, *Journal of Turbomachinery*, Vol. 131, No. 2, pp. 021007-1-10.
- 57 Soe, M. K. K., Ding Shui, T., and Wu, H., 2011, “Analysis of Film Cooling Effectiveness on Antivortex Hole”, *Consumer Electronics, Communications and Networks (CECNet), 2011 International Conference on*.
- 58 Yao, Y., Zhang, J., and Yang, Y., 2013, “Numerical Study on Film Cooling Mechanism and Characteristics of Cylindrical Holes with Branched Jet Injections”, *Propulsion and Power Research*, Vol. 2, No. 1, pp. 30-37.
- 59 Ely, M., and Jubran, B. A., 2009, “A Numerical Evaluation on the Effect Of Sister Holes on Film Cooling Effectiveness and the Surrounding Flow Field”, *Heat and Mass Transfer*, Vol. 45, No. 11, pp. 1435-1446.
- 60 Ely, M. J., and Jubran, B. A., 2009, “A Numerical Study on Improving Large Angle Film Cooling Performance through the Use of Sister Holes”, *Numerical Heat Transfer, Part A: Applications*, Vol. 55, No. 7, pp. 634-653.
- 61 Ely, M. J., and Jubran, B. A., 2010, “A Parametric Study on the Effect of Sister Hole Location on Active Film Cooling Flow Control”, *Proceedings of ASME Turbo Expo 2010*, No. GT2010-22060, pp. 1301-1311.
- 62 Ely, M. J., and Jubran, B. A., 2012, “Film Cooling from Short Holes with Sister Holes Influence”, *Proceedings of ASME Turbo Expo 2012*, No. GT2012-68081, pp. 1185-1196.

- 63 Hassan, J. S., and Yavuzkurt, S., 2006, "Comparison of Four Different Two-Equation Models of Turbulence in Predicting Film Cooling Performance", *Proceedings of ASME Turbo Expo 2006*, No. GT2006-90860, pp. 701-710.
- 64 Tao, Z., Zhao, Z., Ding, S., Xu, G., and Wu, H., 2009, "Suitability of Three Different Two-Equation Turbulence Models in Predicting Film Cooling Performance over a Rotating Blade", *International Journal of Heat and Mass Transfer*, Vol. 52, No. 5-6, pp. 1268-1275.
- 65 Harrison, K. L., and Bogard, D. G., 2008, "Comparison of RANS Turbulence Models for Prediction of Film Cooling Performance".
- 66 Na, S., Zhu, B., Bryden, M., and Shih, T., 2006, "CFD Analysis of Film Cooling", *44th AIAA Aerospace Sciences Meeting and Exhibit*, No. AIAA 2006-0022, pp. 1-10.
- 67 Acharya, S., Tayagi, M., Hoda, A., and Muldoon, F., 1999, "From RANS To DNS: Application To Film Cooling", *Proceedings of the 26th National Conference on Fluid Mechanics and Fluid Power*.
- 68 Tyagi, M., and Acharya, S., 2003, "Large Eddy Simulation of Film Cooling Flow From an Inclined Cylindrical Jet", *Journal of Turbomachinery*, Vol. 125, No. 4, pp. 734-742.
- 69 Konopka, M., Jessen, W., Meinke, M., and Schröder, W., 2013, "Large-Eddy Simulation of Film Cooling in an Adverse Pressure Gradient Flow", *Journal of Turbomachinery*, Vol. 135, No. 3, pp. 031031-1-13.
- 70 Johnson, P. L., and Shyam, V., 2012, "Large Eddy Simulation of a Film Cooling Flow Injected from an Inclined Discrete Cylindrical Hole into a Crossflow with Zero-Pressure Gradient Turbulent Boundary Layer", *National Aeronautics and Space Administration, Glenn Research Center*, No. NASA/TM-2012-217695, pp. 1-23.
- 71 Martini, P., Schulz, A., Bauer, H. J., and Whitney, C., 2006, "Detached eddy simulation of film cooling performance on the trailing edge cutback of gas turbine airfoils", *Journal of turbomachinery*, Vol. 128, No. 2, pp. 292-299.

- 72 ANSYS Inc., 2011, “ANSYS FLUENT User's Guid”, *ANSYS FLUENT 14.0.0*,
Cononsburg, PA, USA.
- 73 Zhang, X., 2008, “Numerical Study of Louver Cooling Scheme on Gas Turbine Airfoils”,
PhD thesis, *Concordia University*.
- 74 Hinze, J. O., 1975, “*Turbulence*”: McGraw-Hill, New York, USA.
- 75 Launder, B. E., and Spalding, D. B., 1972, “*Lectures in Mathematical Models of
Turbulence*”: Academic Press.
- 76 Yakhot, V., and Orszag, S., 1986, “Renormalization Group Analysis of Turbulence. I.
Basic Theory”, *Journal of Scientific Computing*, Vol. 1, No. 1, pp. 3-51.
- 77 Shih, T. H., Liou, W. W., Shabbir, A., Yang, Z., and Zhu, J., 1995, “A new $k-\epsilon$ Eddy
Viscosity Model for High Reynolds Number Turbulent Flows”, *Computers & Fluids*, Vol.
24, No. 3, pp. 227-238.
- 78 Daly, B. J., and Harlow, F. H., 2003, “Transport Equations in Turbulence”, *Physics of
Fluids (1958-1988)*, Vol. 13, No. 11, pp. 2634-2649.
- 79 Lien, F.-S., and Leschziner, M., 1994, “Assessment of Turbulence-Transport Models
Including Non-Linear Rng Eddy-Viscosity Formulation and Second-Moment Closure for
Flow Over a Backward-Facing Step”, *Computers & Fluids*, Vol. 23, No. 8, pp. 983-1004.
- 80 Azzi, A., and Lakehal, D., 2002, “Perspectives in Modeling Film Cooling of Turbine
Blades by Transcending Conventional Two-Equation Turbulence Models”, *Journal of
Turbomachinery*, Vol. 124, No. 3, pp. 472-484.
- 81 Sargison, J. E., 2001, “Development of a Novel Film Cooling Hole Geometry”, PhD
thesis, *University of Oxford*, Department of Engineering Science.
- 82 Bohn, D. E., and Kusterer, K. A., 2000, “Aerothermal Investigations of Mixing Flow
Phenomena in Case of Radially Inclined Ejection Holes at The Leading Edge”, *Journal of
turbomachinery*, Vol. 122, No. 2, pp. 334-339.

- 83 Ardey, S., and Fottner, L., 1997, "Flow Field Measurements on a Large Scale Turbine Cascade with Leading Edge Film Cooling by Two Rows Of Holes", *Proceedings of ASME, the International Gas Turbine & Aeroengine Congress & Exhibition*, No. 97-GT-524, pp. 1-9.
- 84 Ardey, S., and Fottner, L., 1998, "Systematic Experimental Study on the Aerodynamics of Leading Edge Film Cooling on a Large Scale High Pressure Turbine Cascade", *Proceedings of ASME, the International Gas Turbine & Aeroengine Congress & Exhibition*, No. 98-GT-434, pp. 1-12.
- 85 Ardey, S., 1998, "3D-Messung des Strömungsfeldes um die filmgekühlte Vorderkante einer Referenzschaufel", PhD thesis, *University of the Armed Forces*, Munich, Germany (in German).
- 86 Wolff, S. J., 2003, "Aerodynamische Effekte bei Vorderkanten-Filmkühlblasung an hochbelasteten Turbinengittern unter dem Einfluss periodisch instationärer Zuströmung", *University of the Armed Forces*, Munich, Germany (in German).
- 87 Baheri Islami, S., Alavi Tabrizi, S. P., and Jubran, B. A., 2008, "Film Cooling Effectiveness from Trenched Shaped and Compound Holes", *Heat and Mass Transfer*, Vol. 44, No. 8, pp. 989-998.
- 88 Theodoridis, G., and Rodi, W., 1999, "Calculation of the Flow around a High-Pressure Turbine Blade with Cooling-Jet Injection from Slots at the Leading Edge", *Flow, Turbulence and Combustion*, Vol. 62, No. 2, pp. 89-110.
- 89 Benabed, M., Azzi, A., and Jubran, B. A., 2010, "Numerical Investigation of the Influence of Incidence Angle on Asymmetrical Turbine Blade Model Showerhead Film Cooling Effectiveness", *Heat and Mass Transfer*, Vol. 46, No. 8-9, pp. 811-819.